THE UNIVERSITY *of* LIVERPOOL

Detection of Power Disturbances for Power Quality Monitoring Using Mathematical Morphology

Thesis submitted in accordance with the
requirements of the University of Liverpool
for the degree of Doctor of Philosophy

in

Electrical Engineering and Electronics

by

I Gusti Ngurah Agung Dwijaya Saputra,

April 2017

Detection of Power Disturbances for Power Quality Monitoring Using Mathematical Morphology

by

I Gusti Ngurah Agung Dwijaya Saputra

Acknowledgements

I would like to thank my supervisors Professor Q.H. Wu and Professor J.S. Smith for their invaluable support and guidance for this research project. Thanks are also offered to my colleagues in Power System Group for their assistance provided during my study.

I would also like to thank the Directorate of High Education, Republic of Indonesia for funding this research project. I am grateful to the Department of Electrical and Engineering and Electronics, The University of Liverpool, for providing the facilities for my research work. Finally, I am greatly indebted to my parents, my wife, my son and my daughter for their encouragement, understanding, support and love, given during my PhD study.

Abstract

Detection of Power Disturbances for Power Quality Monitoring Using Mathematical Morphology

by:

I Gusti Ngurah Agung Dwijaya Saputra

In power quality monitoring, determining the type of power quality disturbance occurring in the power system is important. Some disturbances such as, voltage dip, momentary interruption, voltage swell, or oscillatory transients in power systems may result in the mal-function or failure in the operation of some devices. Knowing the location where the disturbances occur in the system can yield an effective and efficient result when an appropriate method is applied in the attempt to solve the power quality issues. Some traditional strategies such as, wavelet or Fast Fourier transforms have been applied to detect and locate power quality disturbances, suffer from the complexity of the algoritm and the calculation load. In this thesis, mathematical morphology has been investigated for this purpose due to the merits of robustness and the simple calculations needed.

In this thesis, some novel strategies using mathematical morphology are presented to find the time location of the disturbances, that is defined as the start and end points when the disturbance occur in the time domain. The first method was using morphology gradient, top-hat transform, and Skeletonization to identify the time location of the disturbances and noise in the system, and then plotting the results in

3D for pattern recognition. This Skeletonization is also combined with Morphology Edge Detection to find the accurate time location of disturbances in the system for both noise free signals and signals with noise. The overall result shows the reduction of the error was significant compared to the result of morphology edge detection strategy.

Another novel strategy is presented by converting a signal to an image then applying image processing techniques, which are then evaluated using a control chart to find the time location of any disturbances. This conversion strategy is also applied for detecting the times of power quality disturbances uses short data samples of the signal (4 samples), so that it can be implemented as a real time detection strategy. The results show an accurate strategy in detecting disturbances.

Half Multi-resolution Morphology Gradients (HMMG) based on multi-resolution morphology gradients (MMG) is also presented as a novel strategy and it operates in level 1 only, reducing the processing and increase the speed of detection of disturbance. The results show accurate detection when disturbances occur in the system.

Other applications of MM are also presented such as a new alternative method in estimating the frequency in a signal based on top-hat and bottom-hat transforms with the results showing the ability of this method to handle low frequencies when the signal is a noise free signal. Neural networks are also implemented with MM for the identification and classification of disturbances.

All the novel strategies using Skeletonization, signal/image conversion and HMMG for disturbances detection were then evaluated using a real dataset and an experimental dataset. Overall results show that this three methods can detect disturbances accurately.

Declaration

The author hereby declares that this thesis is a record of work carried out in the Department of Electrical Engineering and Electronics at the University of Liverpool during the period from May 2013 to April 2017. The thesis is original in content except where otherwise indicated.

Contents

List of Figures

List of Tables

Nomenclature

Abbreviation

COF	close-open filter
FFT	Fast Fourier Transform
HMMG	Half Multi-resolution Morphological Gradient
MM	Mathematical Morphology
MEX	Matlab Executable
MSE	Mean Square Error
MMG	Multi-resolution Morphological Gradient
OCF	open-close filter
PDF	Probability Density Function
PNN	Probabilistic Neural Networks
PQ	Power Quality
SNR	Signal to Noise Ratio
SE	Structuring element

Greek

$\hat{A}$	The reflection of A by the origin coordinate

A^c	The complement of A
β_1	internal boundary
β_2	external boundary
C_t	Center of the length of column of the new matrix
$\mathfrak{D}_g$	the definition domains of signal and structuring element
δ_{nB}	dilated image
ε_{nB}	eroded image
ψ	morphological filter
ρ	morphological gradient
(S_{f})	Morphological Skeletonization
σ	Smoothing parameter
τ_s	Soft Threshold
$\oplus$	Dilation
$\ominus$	Erosion
$\bullet$	Opening operation
$\circ$	Closing operation

Roman

a	Level of MMG to be processed
B_{Hat}	bottom-hat Transform
E_m	Cross entropy error
$f(x)$	function of signal
f_{ed}	Morphological edge detection

f_{grad}	morphological gradient
f_{HAT}	top-hat transform of morphology gradient signal
f_{loc}	Time Location of disturbances
g	structuring element
g^{+}	SE used for extracting the ascending edges
g^{-}	SE used for extracting the descending edges
z_j	Hidden layer
y_k	Actual network value
t_k	Target value
l_g	Primary length of g at level 1
N	Number of sampling cycles over an integral multiple of the period of the input signal
T_b	The black top-hat transform
T_w	The white top-hat transform
$U(f)$	Umbra
$V(n)$	Instantaneous value of voltage in the n-th sample interval
W_{jk}	Weighting function
y_{1k}	Value of the vector after the rounding process

Chapter 1

Introduction

1.1 Background

Nowadays, an importance issue in power systems is the quality of the electrical power. This is because the effect of power quality (PQ) is not only on the system itself but there is also on the economic impact if disturbances occurs in the power system. Some examples of disturbances are voltage sag, momentary interruption, voltage swell, or oscillatory transients. The faults in the utility system such as, single line-to-ground faults are the most common cause of voltage sags in an industrial plant [1]. The faults also can produce a momentary interruption. A swell may exist because of the switching off a large load or the energizing a large capacitor bank to the system.

PQ disturbances in power systems may result in the mal-function or failure in operation of some devices connected to the network. Sensitive equipment like computer may crash data. Relays contactor may shut down due to sensitivity from sag. Some components on a power supply equipment may fail because of the effect of swell.

Knowing the time location when the disturbances occur in the system can yield

an effective and efficient result when an appropriate method is applied in the attempt to solve the power quality issues.

Some electrical devices are operated based on the precise time location of the disturbances in the system so the improvement of power quality and protection of electrical apparatus or electrical equipment are needed. These devices operation are based on microprocessor relays. They need accurate data of the time location of disturbances. As a real time detector, the 50-fault detector will compute the data every one-quarter cycle [2]. So, the more accurate the data the better information for protection will be produced.

Accurate data are also needed for power quality data monitoring. Digital Fault and Power Quality Recorder with the disturbance recorder is one of the devices that has a high sampling rate and excellent frequency response for enabling precise analysis of network disturbances [3–5]. The Power Quality Monitoring System [6] for the recording of voltage and current r.m.s. values, frequency, real and reactive power, power factor, current and voltage harmonics, voltage sags and swells, voltage flicker, etc. is a reliable tool to monitor and archive power quality related events. The Power and Frequency Recording System [7] is important equipment in power plants to understand stability problems and analyze related topics like the response of the generator excitation control systems. With an event recorder, various digital signals like the status of a breaker, isolator, and trip contacts of protection relays, etc. can be observed and recorded for further analysis.

Some strategies have been applied to detect and locate Power Quality (PQ) disturbances, such as orthogonal wavelet packet transform [8], embedding strategy [9], Time-Time (TT)-transform [10], or pattern recognition classifier based on neural network and genetic algorithm [11]. Another method in locating power disturbances is by using Mathematical Morphology (MM).

Mathematical Morphology is firstly used in image processing, then followed by

applying it in signal processing. Morphology filtering is one example of MM application in signal processing that it was implemented as a pre-processor for fingerprint processing, and as an efficient technique for electro cardiogram (ECG) wave filtering and analysis of ECG classification [12].

MM has been utilized in the disturbance detection of the time location of the power quality events in electrical power systems using Morphology Edge Detection [13], in the detection of high impedance fault in power distribution systems [14].

In disturbances detection, extracting the features of the signal is a main key in using MM. This can be done using Morphological Gradient Wavelet (MGW) method [15] by separating geometric characteristics of the normal signal and embedded the disturbances to the phase space through the Gustafson-Kessel (GK) clustering algorithm [16].

MM has also been combined with complex wavelets [17] by using de-noised wavelets and a generalized morphology filter for filtering signals, and by subsequently applying the complex wavelet of the Daubechies real wavelet in order to locate the start and end time of the disturbance. The Hilbert-Huang transform (HHT) has been combined with MM to suppress noise effectively. The morphology gradient for mutational components of the signal waveform [18], and MM based and radial coordinate visualization have been developed to detect and locate disturbances [19]. The MM filter Dierion has been used to reduce the noise in transient signals and it improved the performance of the accurate fault location [20].

Another method that based on MM is multi resolution morphology gradient (MMG) [21]. This method can be used to identify the features of electromagnetic transient signal. In application, the MMG is applied to detect fault location in the transmission line by extracting and recognizing transient features of voltage and current of the fault signal. MMG was also combined with closing operator to extract envelope signal for classification of different types of power disturbances [22].

1.2 Motivations

As mention before that producing the faster algorithm in detecting power quality disturbances is essential both for the system itself and the economic advantages. Some strategies that have been developed use complicated method making the strategy need more time to process the calculations. So, the simple methods and the faster calculations process are needed for detecting and classifying the power quality disturbances in the power system.

1.3 Aims and Objectives

The aim of this research is to develop a novel approach for recognizing and classifying power disturbances using Mathematical Morphology (MM) techniques and evaluating their performance such as, the accuracy and processing time of the method against other methods.

Objectives of this research are:

- To detect PQ disturbances using new strategies based on MM and combine them with existing methods.
- To classify PQ disturbances using a combination of MM and Neural Networks

1.4 Contributions

In this thesis, strategies are developed to detect and classify disturbances in power systems. MM was implemented to find the time location of the disturbances. Signals with disturbances were filtered using a morphology gradient. The top-hat transform was applied to the filtered signal using a flat structuring element. The simulation results show that the location of disturbances can be detected accurately.

Skeletonization was used to identify the time location of the noise in the system. By plotting the results in 3D, it is easier to identify the location of disturbances with or without noise with different colors and shapes for pattern recognition.

A new combination of skeletonization and Morphology Edge Detection is proposed to find the accurate time location of disturbances. This proposed strategy is implemented using MATLAB for voltage sag, swell, and interruption, both with noise-free signals and with signals that contained noise. Firstly, signals with disturbances were filtered using a morphology gradient then Morphology edge detection was applied by using the top-hat transform using a flat structuring element. After that, a soft threshold was applied to eliminate the background noise. After this step, the results still had errors, so skeletonization [23] was introduced to the system to find the accurate time location of disturbances both in noise-free signals and in signals with noise. This strategy can detect the disturbances more accurately compared to the previous strategy.

Another strategy applied was converting a signal to an image matrix. This allow an image processing strategy to be applied to the image. In this case, a structuring element for image processing was chosen for this strategy. A control chart was used to post process the image to identify the start and the end of disturbances as violation points. This vector to matrix conversion is also then applied on a small window size. Comparing the mean value of each row of the new matrix to the mean value of the normal signal, and then choosing the higher value will locate any disturbances in the signal.

This thesis also presents a new method for the detection and classification of power disturbances in power distribution systems using half the process of Multi-resolution morphology gradients (MMG). It is called Half Multi-resolution Morphology Gradients (HMMG). The results can be found in level 1 thus the processing time is reduced or the speed of detection is increased. The location of the distur-

bances can be detected as the difference between the input signal and the ascending and descending edges of the waveform.

1.5 Publications

- **IGNA Dwijaya Saputra**, Q.H. Wu, and W.H. Tang, "Location Time of Power Quality Disturbances Using Morphology Gradient and Skeletonization of Mathematical Morphology in 3D", The 4th International Seminar APTECS (Applied Technology, Science & Arts), At ITS, 2013, 10 December 2013, Surabaya, Indonesia.

- **IGNA Dwijaya Saputra**, J.S. Smith, and Q.H. Wu, "Combination of Skeletonization and Morphology Edge Detection for Detecting Time Location of Power Disturbances", The 5th IEEE PES Innovative Smart Grid Technologies (ISGT) European 2014, 13 October 2014, Istanbul, Turkey.

- **IGNA Dwijaya Saputra**, J.S. Smith, and Q.H. Wu, "Detection of Power Disturbances using Mathematical Morphology on Small Data Windows", 39th International Conference on Telecommunications and Signal Processing (TSP), 27-29 June 2016, Vienna, Austria.

- **IGNA Dwijaya Saputra**, J.S. Smith, L. Jiang, and Q.H. Wu, "Detection and Classification of Power Disturbances Using Half Multi-resolution Morphology Gradient", IEEE PES Innovative Smart Grid Technologies (ISGT) European 2016, 9-12 October 2016, Ljubljana, Slovenia.

1.6 Organization of the Thesis

This thesis is structured as follows:

Chapter 2 introduces the theoretical background of MM. The basic operators of MM such as dilation, erosion, opening, and closing are discussed at the start of this chapter. After that, a brief explanation of the implementation of MM in image and signal processing is presented.

Chapter 3 introduces an implementation of MM to find the time location of disturbances. Firstly, the proposed strategy for using morphology gradient in filtering input signals is introduced. This is then followed by the initial location of disturbances detection using the top-hat transform with a flat structuring element. A brief description of Skeletonization is presented to identify the time location of the noise in the system, and the 3D plotting used to identify the location of disturbances with or without noise with different colors and shape as a pattern recognition.

This chapter also presents an application of the combination of skeletonization and morphology edge detection for detecting the time location of power system disturbances. A brief description of morphological filter, morphology gradient, top-hat transform, and Skeletonization are outlined at the beginning of this chapter. After that the simulation strategy and results both in noise-free and signals with noise are presented.

Chapter 4 introduces a new strategy to find the time location of disturbances using the idea of transferring a signal to an image then processing it by using the methods used in image processing. Boundary extraction is presented in converting the signal to a matrix in this method. The last part of this chapter presents the image result evaluation using a control chart to find the time location of disturbances as violation points in control chart.

This chapter also presents an advanced method of disturbance detection using a vector to matrix conversion with a MM in a small window size.

Chapter 5 starts with the theory of Multi-resolution Morphology Gradient and then Half Multi-resolution Morphology Gradient. These two strategies were then

compared in terms of disturbances detection in power system, followed by the classification of disturbances for transient, notching, flicker, sag, swell, and interruption.

Chapter 6 introduces an alternative in estimating the frequency of the signal. This strategy based on the top-hat and bottom-hat transforms. The simulation results is presented in different conditions of the signal like using the variety of SNR and frequency.

Chapter 7 is focused on Probabilistic Neural Network (PNN) to classify some PQ disturbances in the system. A HMMG is used for detecting the disturbances then followed by a PNN for classification of the disturbances.

Chapter 8 presents the evaluation of 3 methods that have been developed (Skeletonization, Signal to Image convertion, and HMMG) for detecting sag, swell and interruption using real data. Datasets were acquired from the laboratory and also from the IEEE Dataport.

Chapter 9 presents conclusions of all methods that have been developed. It is also added some recommendations for future work in order to improve this performance.

Chapter 2

Basic Principle of Mathematical Morphology

2.1 Introduction

Mathematical Morphology (MM) is a powerful tool in image processing to analyze the geometrical shapes of images. Introduced for the first time in 1964 by French researchers Matheron and Serra [23], MM became a popular method in digital image analysis after its foundation had been laid down in 1975 [24]. This is because of the ability to simplifying image data and in preserving the essential shape information of the image [25].

The basic ideas of MM stem from the general mathematical operations such as, translation, reflection, complement, and difference. There are two basic operators in MM, dilation and erosion. By using combinations of these operators, all other operations can be made [26].

In image processing, MM is used to detect the object boundaries of an image by using the basic operations of MM, $dilation$ and $erosion$. Another application of MM is under the concept of using the combination of $dilation$ and $erosion$,

which are the $opening$ and $closing$ operations. Using this combination, the filter for smoothing gray-scale images can be developed. The operation of noise reduction is removing thin features from the image. By using a morphological image cleaning (MIC) algorithm this limitation can be eliminated [27]. Another strategy in removing noise from images uses two stages, which are detecting the noisy pixels in the image, and then replacing the noisy pixels using the median value of the neighborhood noise free pixels [28], and by using the Block Smart Erase (BSE) algorithm [29].

Another application of MM is in image segmentation [30]. It has been implemented in medical areas such as medical image segmentation [31, 32] and the analysis of $High - Resolution\ Computed\ Tomography$ (HRCT) images of the lung [33]. It is an important step in assisting in diagnosis for medical treatments.

The scope of MM applications became broader when artificial intelligence such as the fuzzy mathematical morphology (FMM) filter was used especially in image denoising [34,35]. Due to some of the drawbacks of this fuzzy morphology strategy, an adaptive fuzzy morphology filter [36], and then a dynamic fuzzy mathematical morphology (DFMM) using an adaptive structuring element (ASE) were developed to eliminate the need of deciding the shape and value of the structuring element before image processing and the large changes of the image by the selection of the structuring element [37]. The structuring element will be presented later on this chapter.

MM has also been applied in signal processing applications such as in removing noise in vibration signals [38], detecting fault location accurately [39], and detecting power fault signals [40].

In this chapter, some application of MM in image and signal processing will be presented. One of the applications of MM is the boundary detection of object in an image. By applying a combination of dilation and erosion, the object boundary can

be determined, not only the internal boundary and the external boundary, but also the morphological gradient (a combination of the internal and external boundary). In signal processing, MM can also be used for signal filtering.

2.2 Principle of MM

Mathematical Morphology (MM) is a powerful image-processing tool to analyze shapes in images [23, 41]. It has the ability to analyse binary images and change them into greyscale images. One of the standard methods in MM, which uses operations on sets of point, can be defined as follow:

2.2.1 Translation

If A is a set of pixels in a binary image, and w =*(x,y)* is a particular coordinate point, then A "translated" in direction *(x,y)* is defined as A_w. That is:

$$A_w = \{c|c = a + w, \forall a \in A\}. \tag{2.2.1}$$

Figure 2.1 shows an example of the translation operation using matrix coordinates with w =(2,2), which has shifted A in the x and y directions.

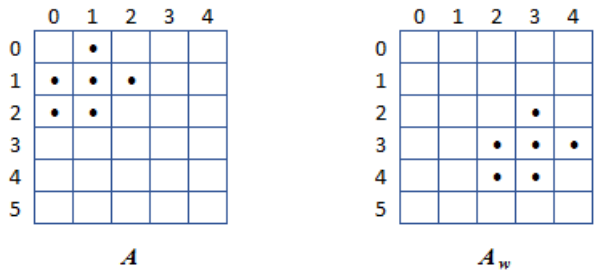

Figure 2.1: Translation operation example

2.2.2 Reflection

The reflection of A by the origin coordinate is denoted as $\hat{A}$:

$$\hat{A} = \{x | x = -a, \forall a \in A\}. \tag{2.2.2}$$

An example of the *Reflection* operation can be seen in Figure 2.2.

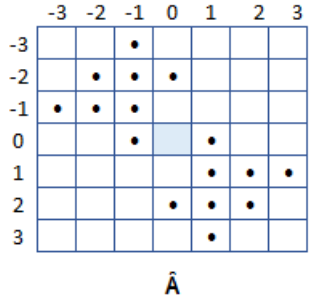

Figure 2.2: Reflection operation example

2.2.3 Complement

The complement of A, denoted by A^c, is defined as

$$A^c = \{x | x \notin A\}. \tag{2.2.3}$$

For example, Figure 2.3 shows the *complement* operation.

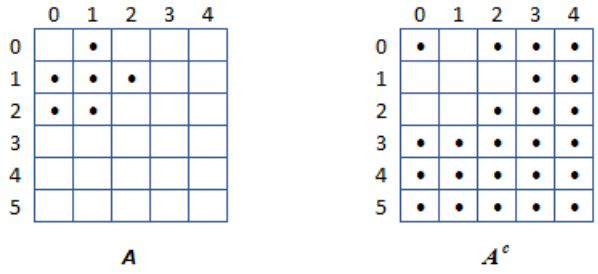

Figure 2.3: Complement operation example

2.2.4 Difference

The difference of two sets A and B, denoted by $A - B$, is defined as

$$A - B = \{x | x \in A, x \notin B\} = A \bigcap B^c. \tag{2.2.4}$$

The Example of this operation can be seen in Figure 2.4.

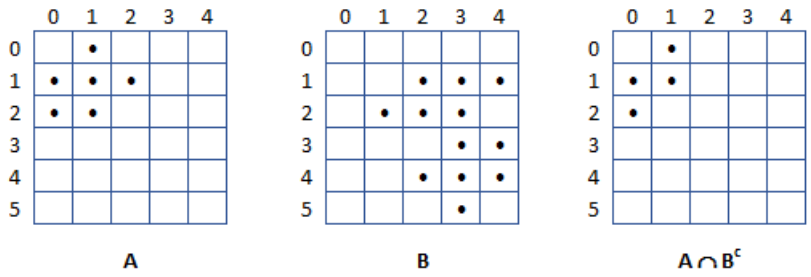

Figure 2.4: Difference operation example

2.3 Basic Operation of Mathematical Morphology

The basic operations of MM are ***dilation*** and ***erosion*** and combinations of these two operations.

2.3.1 Binary Dilation and Erosion

The dilation of sets of pixels A and B is defined as [42]:

$$A \oplus B = \bigcup_{b \in \hat{B}} (A)_b = \bigcup_{b \in B} (A)_{-b} = \{x | x = a + b, a \in A \wedge b \in B\}. \tag{2.3.1}$$

where: *a=(x,y)*, *b=(u,v)* and $\hat{B}$ = reflected structuring element.

Dilation is also known as *Minkowski addition* [43]. The effect of dilation is increasing the size of an object. An example of this effect in an image is given in Figure 2.5.

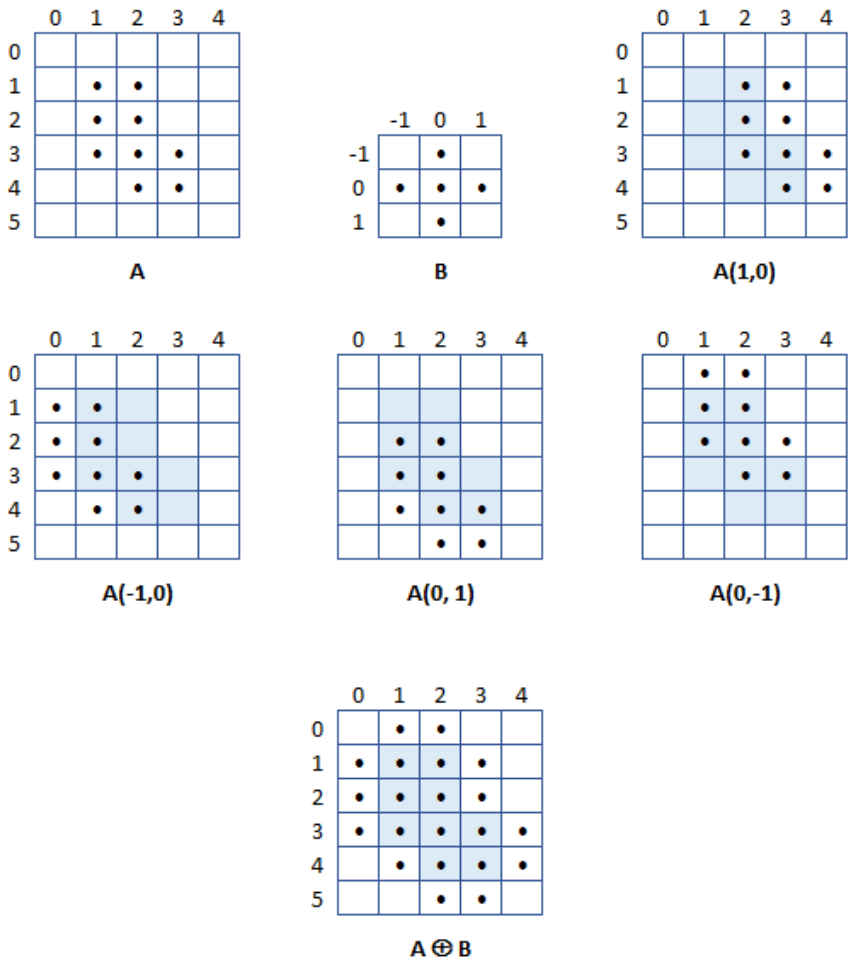

Figure 2.5: Dilation

In dilation, A is the processing image and B is a small set of pixels that is referred to as *a structuring element* or *a kernel*. There is a communicative operation in *dilation*:

$$A \oplus B = B \oplus A. \tag{2.3.2}$$

The *erosion* of A by B is related to *Minkowski substraction*. Then the *erosion* is defined as:

$$A \ominus B = \bigcap_{b \in \hat{B}} (A)_b = \bigcap_{b \in B} (A)_{-b} = \{x | x + b \in A, \forall b \in B\}. \tag{2.3.3}$$

Different from the dilation procedure, the effect of erosion is a shrinking of the image pixels, this can be seen in Figure 2.6.

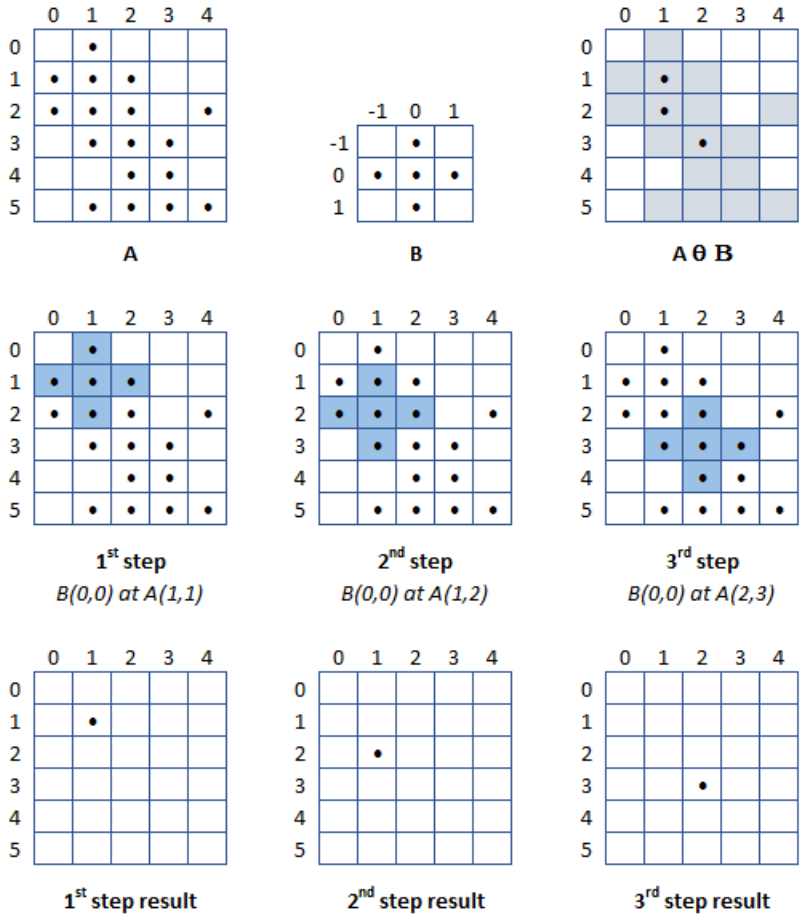

Figure 2.6: Erosion

2.3.2 Relation Between Dilation and Erosion

It is clearly seen that dilation is the inverse of erosion, or in other words, the complement of erosion is equal to the dilation of the complement [43]. So that, in mathematical form:

$$\overline{A \ominus B} = \overline{A} \oplus \hat{B}. \tag{2.3.4}$$

If erosion and dilation are interchanged, the relationship between them will have the same result, then it can be written as:

$$\overline{A \oplus B} = \overline{A} \ominus \hat{B}. \tag{2.3.5}$$

2.3.3 Opening and Closing

Opening and Closing are a combination of erosion and dilation. The Opening operation can be defined as:

$$A \circ B = (A \ominus B) \oplus B. \tag{2.3.6}$$

and the Closing operation as:

$$A \bullet B = (A \oplus B) \ominus B. \tag{2.3.7}$$

Opening is used to eliminate small holes, and to fill gaps in the contour while closing tends to smooth the sections of the contours.

2.4 Structuring Element

The structuring elements (SE) are the foundation of all MM transformations, and are used as probes for feature extraction. The lengths of the SE can vary and also they can be linear, sinusoidal, square, circular, or an other geometrical shapes

[44]. For each particular application, the frequency of interest is a primary key in the selection of the structuring element. The choice is influenced by other factors such as the type of signal, frequency spectrum, and the sampling rate. The optimal choice would be such that it captures the feature of interest whilst suppressing other features.

There are many types of structuring element in image processing. Some of them can be seen in Figure 2.7.

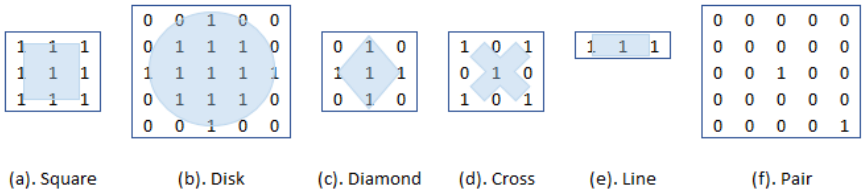

Figure 2.7: Various shapes of SEs in image processing

The SE is the key component to be defined after selecting the morphological operator. Generally, only when the scale and shape of the signal are matched to those of the SE, the signal can be preserved. Therefore, the shape, length (domain) and height (amplitude) of SE should be selected according to the signal to be analyzed. The shapes of the SE can vary from regular to irregular curves, such as flat, triangle, semicircular, and so on.

Some types of structuring elements for signal processing can be seen in Figure 2.8. When defining a SE in signal processing, a principle shall be followed, which is that the SE should approach the morphological features of the signal as far as possible. The triangular, circular and flat SE are good candidates to extract the morphological features of the vibration signal that have been presented in [45].

Figure 2.8: Various shapes of SEs: a) flat SE, b) triangular SE, c) semicircular SE

An example of triangular shape of SE is used in multiscale morphology for extracting features of the signal [45]. Not only the shape, but also the scale of the SE, including both the length and height scales are important for the morphology analysis of 1-D signals and can be seen in Figure 2.9.

Figure 2.9: SEs of multiscale morphology

Another type of SE is introduced in Generalized Morphological Open-closing and Close-opening Wavelet (GMOCW) strategy by using the SE Unit (SEU) [46]. The shapes of SEU in this GMOCW are the two types that can be seen in Figure 2.10.

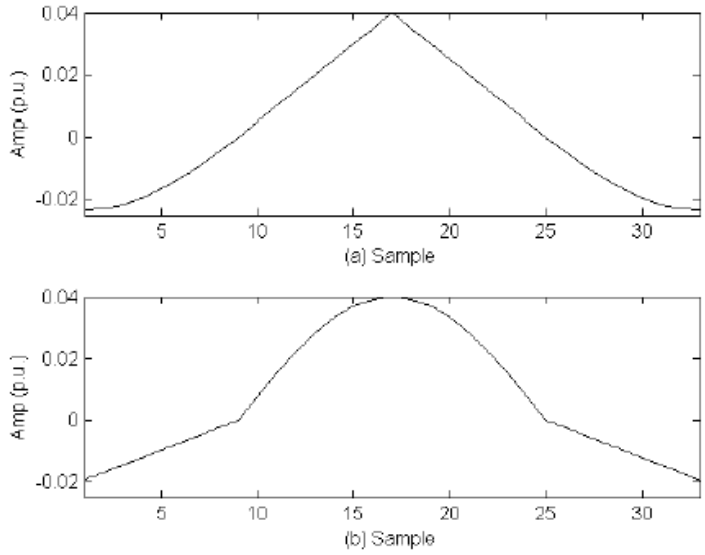

Figure 2.10: The shapes of the SEUs used in GMOCW

There are limited rules or guidelines for choosing the optimum SE for various application and operators, so some researchers conducted experiments to determine the optimum SE [45,47–50]. In morphological filtering, the results of the operations depend on not only on the form of the morphological transformation but also the size and shape of the structuring element. Commonly, only when the signal is suited for the size and shape of the SE, it can be well preserved. If the SE width is longer and its shape is more complex, the filter results will be better and the amount of operation will be larger. In [51], horizontal linear structure elements were chosen to filter impulses and random white noise in the signal. The length of the linear SE is chosen to be bigger than the width of the biggest impulse.

2.5 Application of Mathematical Morphology in Image Processing

Basic MM has been applied in image processing. When the dilation operation is used in an image, on increase in the object pixels will occur. Figure 2.11 shows that the effect of this process makes the text in that image become blurred. On the other hand, there is an inversion effect in an image if the erosion process has been applied. The object would be shrunk or became thinner as shown in Figure 2.12.

Figure 2.11: Effect of dilation on an image

Figure 2.12: Effect of erosion on an image

2.5.1 Boundary Detection

There are some applications in image processing using MM. One of them is boundary detection. The detection of the boundary of an image A can be defined by the following methods, where B is a small structuring element that is placed about the origin symmetrically.

- Internal boundary

$$A - (A \ominus B) \tag{2.5.1}$$

- External Boundary

$$(A \oplus B) - A \tag{2.5.2}$$

- Morphological gradient

$$(A \oplus B) - (A \ominus B) \tag{2.5.3}$$

Figure 2.13 shows the boundary detection for each definition. An example application in detecting the boundaries in an image (coins and key) will be described as follows.

The original RGB image (Figure 2.14) is converted into a greyscale image (Figure 2.15), then processed by applying a threshold to obtain a binary image showing only the objects and isolating the background [52]. The boundaries of the coins and keys in the image are detected as internal boundaries (Figure 2.16b), external boundaries (Figure 2.17a), and the morphological gradient (both of internal and external boundaries in Figure 2.17b by using Matlab software. The internal boundaries show the outer edge of an image component for both the coins and keys while external boundaries show the outside pixels of the object.

2.5.2 Noise Removal

One example of an MM implementation is on removing noise from signals. The basic idea of noise removal in signal processing is based on the same idea in removing noise from images. Some images may have noise because of some reasons such as, the noise that is produced by sensor and circuitry of a scanner or digital camera or the problem in data transmission. In order to remove this noise, applying an opening and closing operation of MM in the images will fix this issue.

An example of noise removal in an image can be seen in Figure 2.18. When a binary image has impulse noise, it means that some of the black pixels are white while some of the white pixels are black. This noise can be removed by using the following steps.

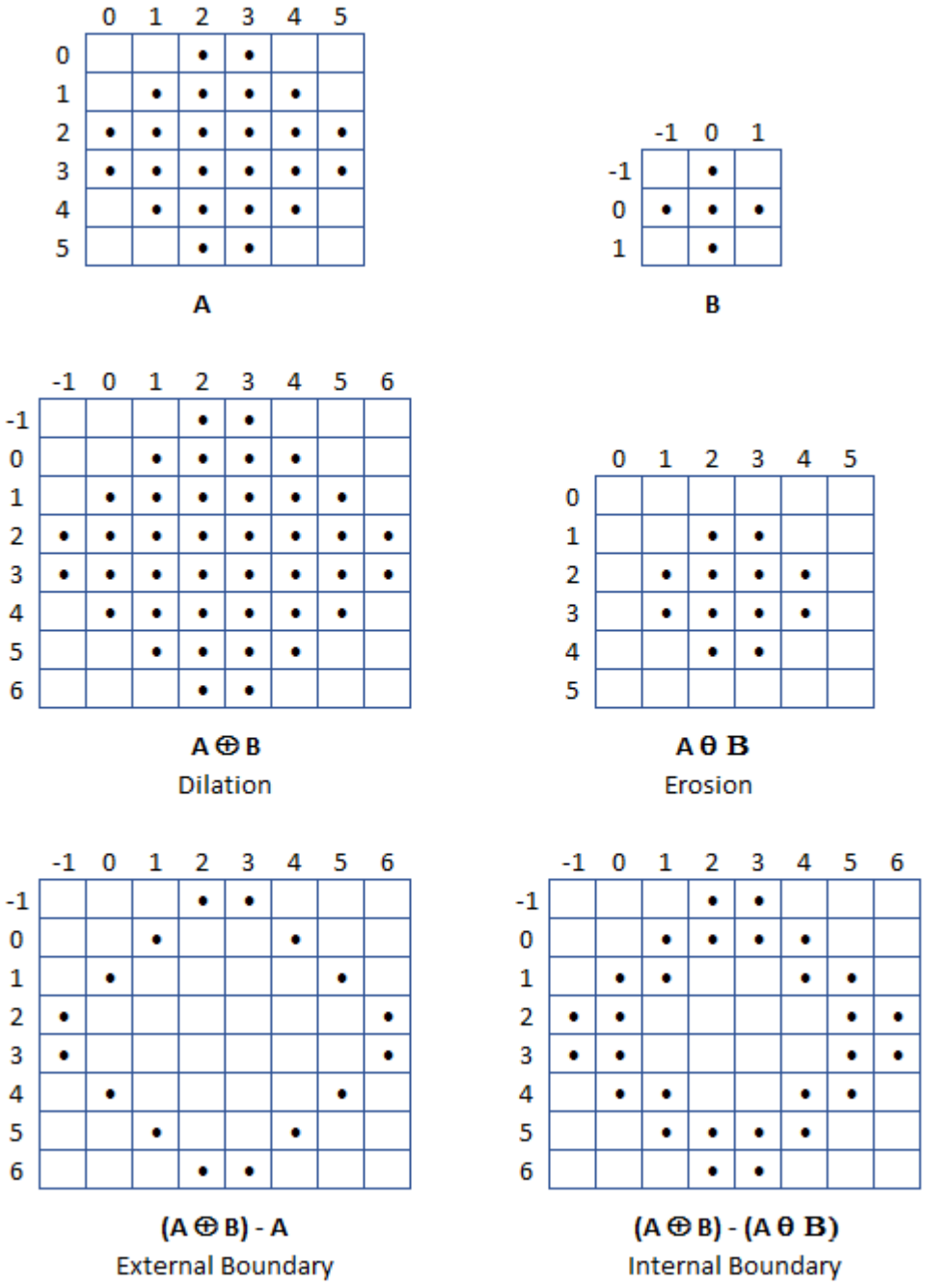

Figure 2.13: Boundary detection

Figure 2.14: Original image of coins and key

Figure 2.15: Greyscale image of coins and key

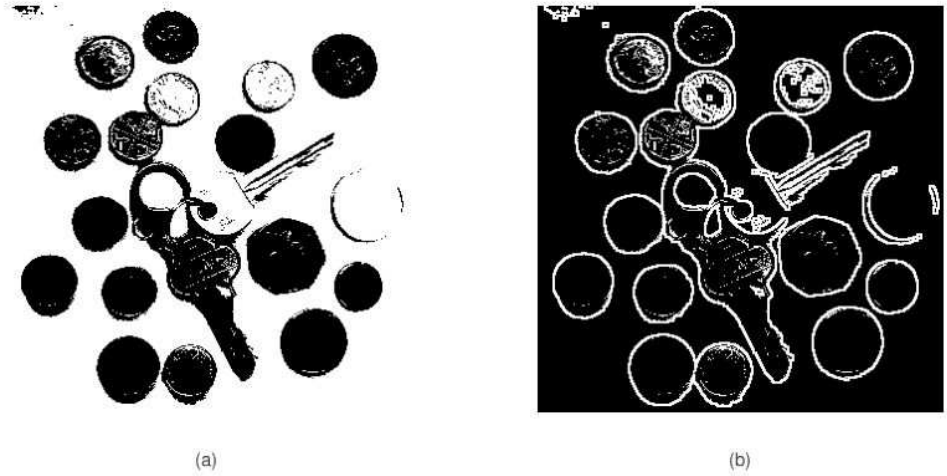

Figure 2.16: (a) Thresholding image; (b) Internal boundary

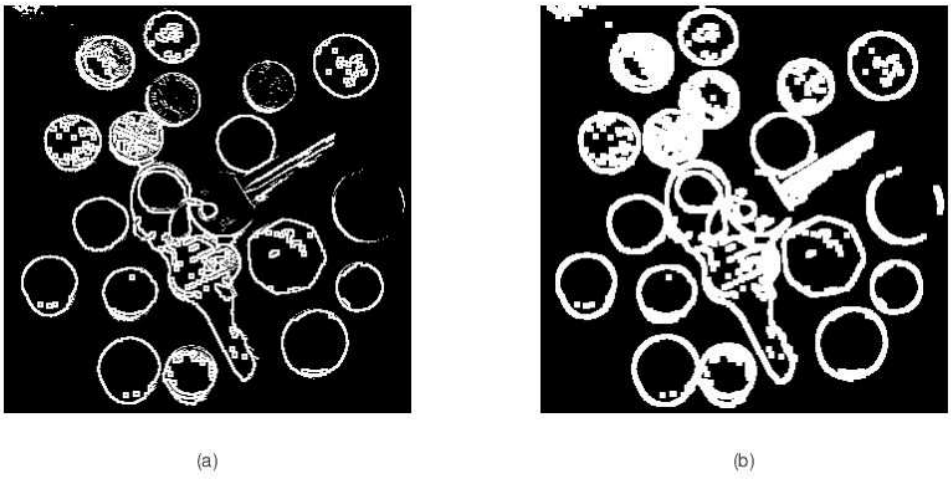

Figure 2.17: (a) External boundary; (b) Morphology gradient

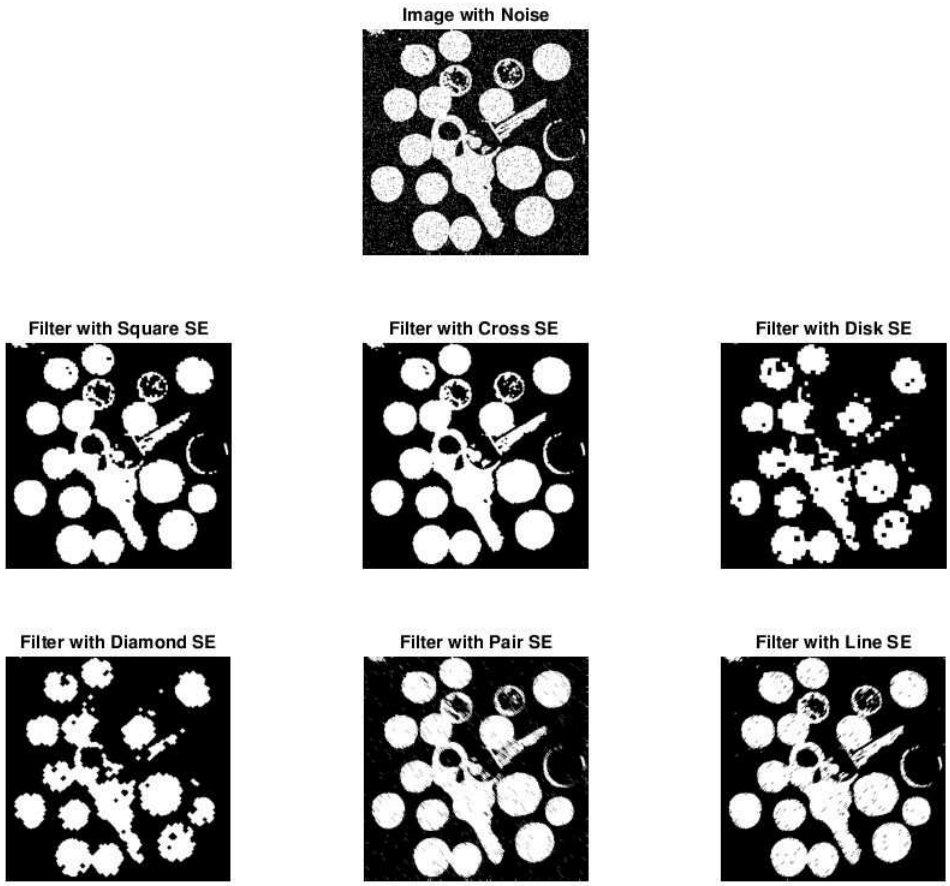

Figure 2.18: Noise removal in image using different structuring element

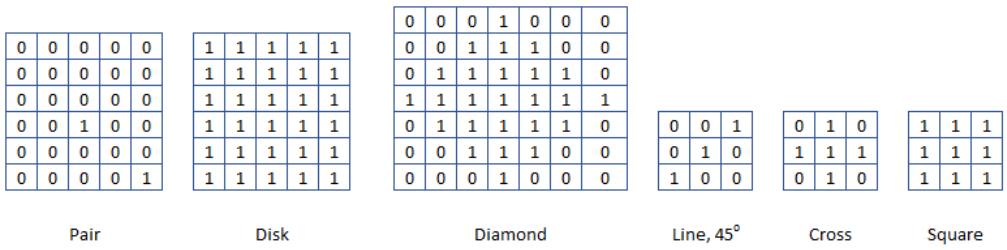

Figure 2.19: Different type of structuring element for noise removal

Firstly, by using the erosion operation $A \ominus B$ in this corrupted image A will remove the single black pixels, but will enlarge the holes. After that the dilation

operation will be applied to the image twice. In these operations, the holes were returned to their original size in the first dilation, and then the holes were removed in the second dilation. Consequently, the objects in the image were enlarged. The mathematical operation for this step is as follows:

$$((A \ominus B) \oplus B) \oplus B = (A \circ B) \oplus B \tag{2.5.4}$$

The last step is using the erosion operation in order to reduce the incorrect size of the object in the image, and the results using different structuring element such as *square, cross, disk, diamond, pair, and line* (Figure 2.19) can be seen in Figure 2.18.

$$(((A \ominus B) \oplus B) \oplus B) \ominus B = ((A \circ B) \oplus B) \ominus B \tag{2.5.5}$$

In this equation, it is clearly seen that the inner two operations are an $opening$, and the outer two are a $closing$. So, the method in removing of the noise is using an opening followed by a closing operation, which is called $morphology\ filtering$ and can be written as follows:

$$\text{Morphology Filtering} = (A \circ B) \bullet B) \tag{2.5.6}$$

2.6 Mathematical Morphology in Signal Processing

As mention before MM can be applied not only in image processing but also in signal processing. Since most of the signals are not binary, a grey-scale should be used by extending the morphology operators. In this grey-scale, the process of MM uses algebraic addition and subtraction for dilation and erosion; while in the binary case, it uses the union and intersection operations.

2.6.1 Functions and Umbra

Morphological operators need to be extended to functions, where the functions are represented by their umbra [53], which is defined as:

$$U(f) = \{(x, y)|y \leq f(x)\} \tag{2.6.1}$$

In this case a D-dimensional function $f(x)$ is represented by a $(D+1)$-dimensional set. So, it can be clearly seen that the umbra is the set of points below the surface represented by $f(x)$. By using the umbra, binary morphological operators can be applied to the signal.

In general, the umbra set extends to $y = -\infty$, and the function f can be reconstructed from its umbra since:

$$f(x) = max\{a|(x, a) \in U(f)\}, \forall x. \tag{2.6.2}$$

An example of the umbra of a sinusoidal function as a shaded region can be seen in Figure 2.20. It shows that $f \leq g \Leftrightarrow U(f) \subseteq U(g)$.

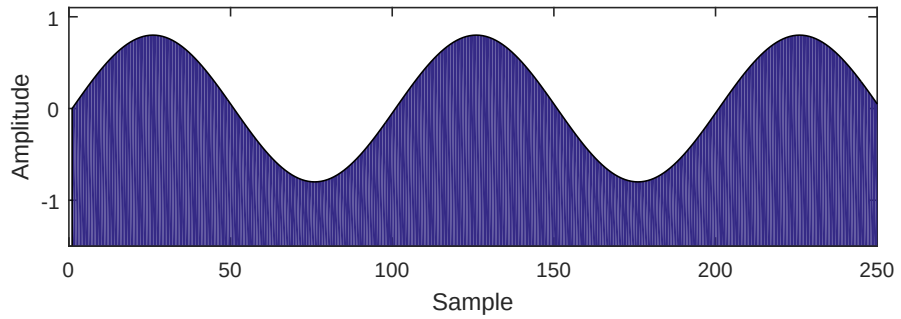

Figure 2.20: Umbra $U(f)$ of a sinusoidal function f

Some definitions for grey-scale operations based on sets are defined as follows [54]:

1. Grey-scale union:

The union of two functions f and g, denoted by $f \vee g$, is defined as:

$$(f \vee g)(x) = f(x) \vee g(x) \tag{2.6.3}$$

There is a one-to-one correspondence between the union of functions and the set union:

$$U(f \vee g) = U(f) \cup U(g) \tag{2.6.4}$$

2. Grey-scale intersection:

The intersection of two functions f and g, denoted by $f \wedge g$, is defined as:

$$(f \wedge g)(x) = f(x) \wedge g(x) \tag{2.6.5}$$

A similar one-to-one correspondence exists for the function and the set intersection:

$$U(f \wedge g) = U(f) \cap U(g) \tag{2.6.6}$$

3. Grey-scale transpose:

The transpose $\breve{f}$ of a function f is defined as:

$$\breve{f}(x) = f(-x) \tag{2.6.7}$$

4. Grey-scale complement:

The complement f^c of a function f is defined as:

$$f^c c(x) = -f(x) \tag{2.6.8}$$

Figure 2.21 shows the grey-scale operations in the graph as a solid line. In these figures, it can be noticed that $f \vee f^c = |f|$ and $f \wedge f^c = -|f|$, whereas for sets, we have $A \cup A^c = I$ and $A \cap A^c = \emptyset$.

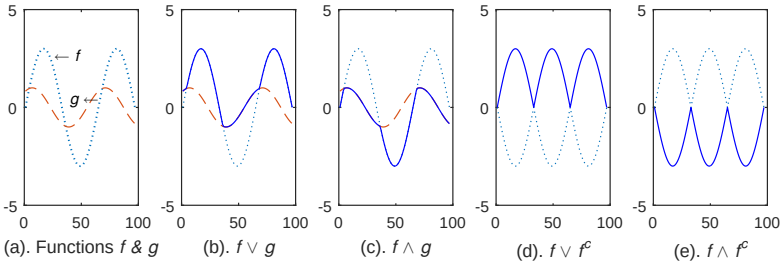

Figure 2.21: Grey-scale operations with 2 functions; f (dotted line) and g (dashed line)

2.6.2 Grey-Scale Dilation and Erosion

By denoting f as a signal and g as a structuring element (SE) where g should be shorter than f, the dilation and erosion can be defined as follows:

$$f \oplus g(x) = \max_s \{f(x+s) + g(s) | (x+s) \in \mathfrak{D}_f, s \in \mathfrak{D}_g\} \tag{2.6.9}$$

$$f \ominus g(x) = \min_s \{f(x+s) - g(s) | (x+s) \in \mathfrak{D}_f, s \in \mathfrak{D}_g\} \tag{2.6.10}$$

where $\mathfrak{D}_f$, $\mathfrak{D}_g$ are the definition domains of f and g, respectively.

An example of dilation and erosion is explained as follows:

For the structuring element g which has a length of five samples with its origin in the middle, $\mathfrak{D}_g$ will have values $\mathfrak{D}_g$ = {-2,-1,0,1,2}. The calculation of the dilation and erosion of f by g will be:

$$f \oplus g(x) = \max_s \ \{f(x-2) + g(-2), f(x-1) + g(-1), f(x) + g(0), \\ f(x+1) + g(1), f(x+2) + g(2)\}$$

and

$$f \ominus g(x) = \min_s \ \{f(x-2) - g(-2), f(x-1) - g(-1), f(x) - g(0), \\ f(x+1) - g(1), f(x+2) - g(2)\}$$

The structuring element g, is used to indicate which samples are involved in the process of the current sample. A flat SE must be used for binary signals. By using a flat SE, $g(s) \equiv 0, s \in \mathfrak{D}g$, so equations 2.6.9 and 2.6.10 will become:

$$f \oplus g(x) = \max_s \{f(x+s) | (x+s) \in \mathfrak{D}_f, s \in \mathfrak{D}_g\} \tag{2.6.11}$$

$$f \ominus g(x) = \min_s \{f(x+s) | (x+s) \in \mathfrak{D}_f, s \in \mathfrak{D}_g\} \tag{2.6.12}$$

For signal f = [0 0 0 0 0 0 1 2 3 4 5 6 6 5 5 5 5 4 4 4 3 3 3 5 5 5 2 1 0 0 0 0 0], with g = 5, the effect of dilation and erosion can be seen in Figure 2.22 and also Figure 2.23 with a different plot style.

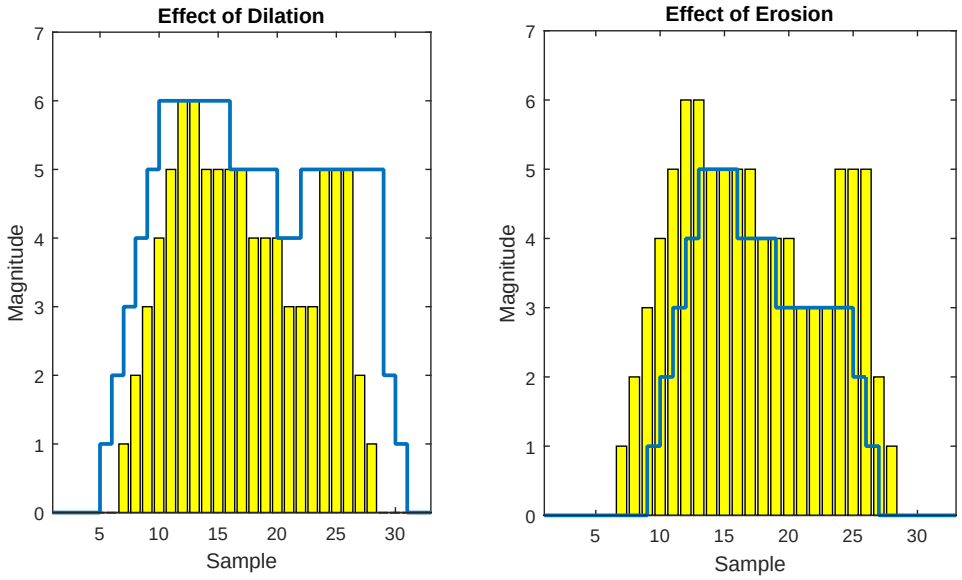

Figure 2.22: Effect of dilation and erosion in signal

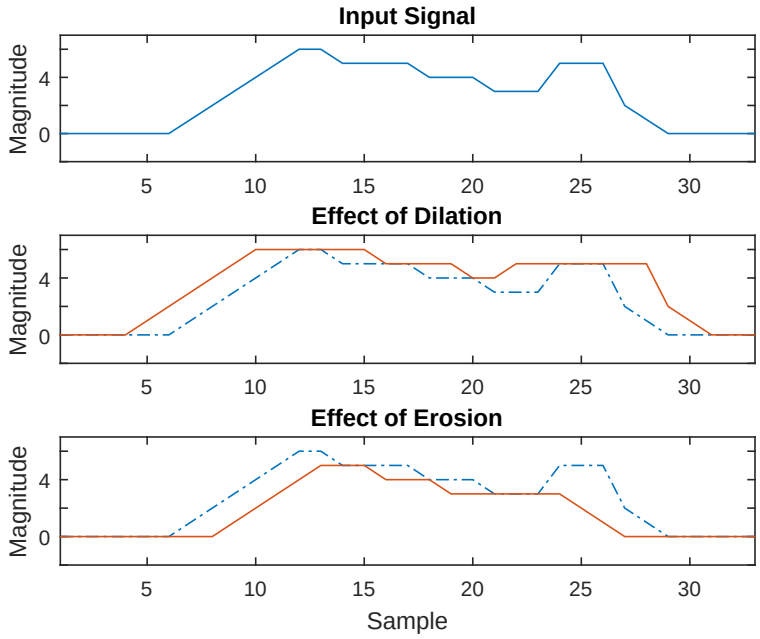

Figure 2.23: A signal that is processed by dilation and erosion

For a sinusoidal signal $f = 100\ sin(\omega t)$ the results of dilation and erosion are shown in Figure 2.24

The effect of dilation in signal processing is an expanding of the signal while that of erosion is shrinking. This means that a sample of the signal within a window when the SE contains its origin can be denoted as follows;

$$f \ominus g(x) \leq f \leq f \oplus g(x) \tag{2.6.13}$$

2.6.3 Morphological Filters of Opening and Closing

Morphological filters are non-linear signal transforms that locally modify the geometrical features of signals or image objects. A condition of the properties of the morphological filter for a transform ψ are idempotence and increasing, and it can be denoted as:

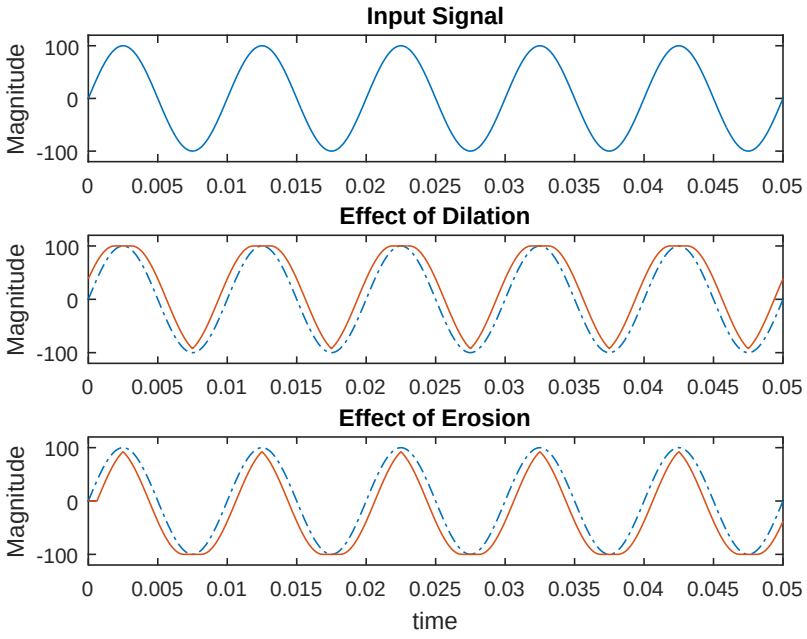

Figure 2.24: Effect of dilation and erosion in sinusoidal signal

ψ is a morphological filter $\Leftrightarrow$ ψ is increasing and idempotent.

Idempotence means applying a morphological filter twice to a signal is equivalent to applying it only once, and it can be denoted as:

ψ is idempotent $\Leftrightarrow$ $\psi\psi = \psi$

The opening and closing operators in signal processing are the same as in image processing. The opening operation is denoted as follows:

$$f \circ g = (f \ominus g) \oplus g. \tag{2.6.14}$$

and the closing operation:

$$f \bullet g = (f \oplus g) \ominus g. \tag{2.6.15}$$

The effects of opening and closing on the previous signal and a sinusoidal signal

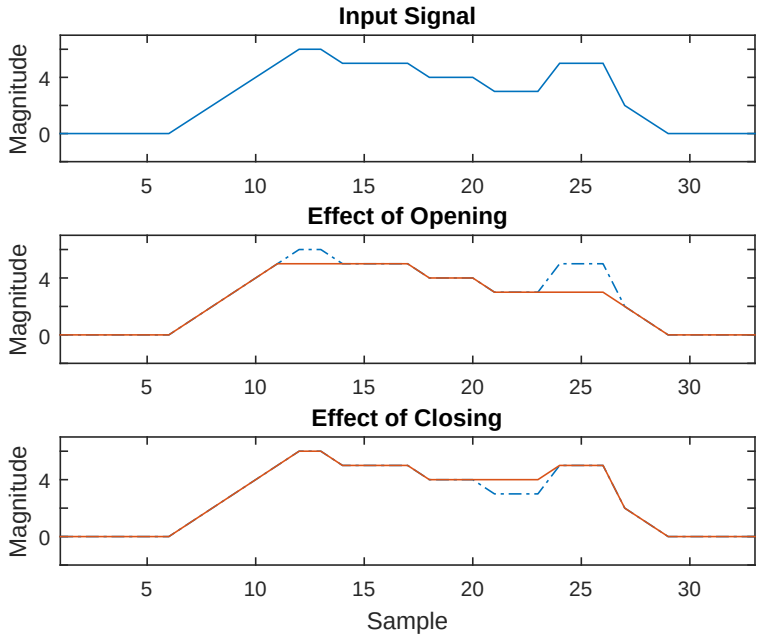

Figure 2.25: Effect of opening and closing on a signal

with $g = 5$ can be seen in Figures 2.25 and 2.26 respectively.

2.7 Summary

This chapter presents the basic operations of MM using methods such as, *translation, reflection, complement* and *difference*. There are two basic operators in MM; dilation and erosion. The effect of dilation is that the object becomes thicker whereas erosion shrinks the object in an image. These basic operators of MM can be applied in the boundary detection of an image by using the internal and external boundary and morphological gradient methods. MM can also be implemented in signal processing using Grey-scale dilation and erosion. Filtering a signal can be done by combining the dilation and erosion operators to become opening and closing.

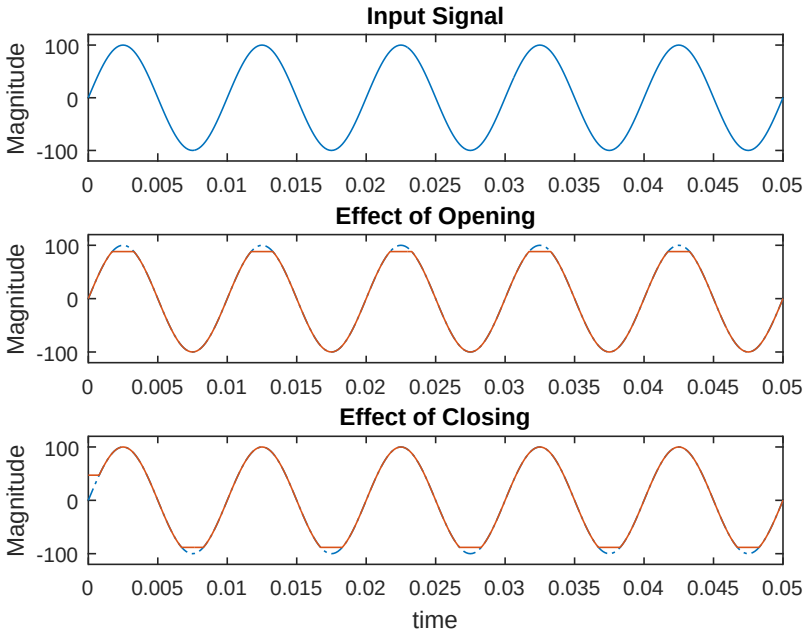

Figure 2.26: Effect of opening and closing for a sinusoidal signal

Chapter 3

Time Location of Power Quality Disturbances Using Morphology Gradient and Skeletonization

3.1 Introduction

In power quality monitoring, determining the type of power quality disturbance occurring in the system is important, as disturbances are not always obvious. Many types of power quality monitors are available in the market and they have the ability to measure and record all energy data such as voltage, current, average power factor, instantaneous power factor, active power, reactive power, frequency and all the disturbances.

Some disturbances such as, voltage dip, momentary interruption, voltage swell, or oscillatory transients in power systems may result in the malfunction or failure in the operation of some connected devices. Knowing the location where the disturbances occur in the system can yield an effective and efficient result when an appropriate method is applied in the attempt to solve the power quality issues. Some

electrical devices are operated based on the precise time location of the disturbances in the system. Therefore, power quality should be improved and electrical apparatus or electrical equipment should be protected.

In order to detect and analyse power quality disturbances, conventional strategies based on Fourier transforms have been applied. These strategies use fixed window lengths and thus cannot detect transients.

To detect transients, strategies based on the wavelet transform [55–59] were developed. Unfortunately, this method has a problem in real time implementation due to the complexity of the calculations required.

In this chapter, MM is implemented to find the time location of disturbances. Signals with disturbances were filtered using the morphology gradient. The top-hat transform is applied on the filtered signal using a flat structuring element. The simulation results show that the location of disturbances can be detected accurately. Skeletonization is used to identify the time location of the noise in the system. Plotting the results in 3D makes it easier to identify the location of disturbances with or without noise with different colors and shapes for pattern recognition.

3.2 Definitions in Power Quality

There are some definitions in power quality, such as:

- **Power quality** is a set of electrical characteristics that allows a piece of equipment to function in its intended manner without significant loss of performance or life expectancy. It describes its impact on system operation. The electrical boundaries are the nominal operating levels of voltage, current, and frequency.

- **Sag** is an rms reduction in the ac voltage, at the power frequency, for durations

from a half cycle to a minute (IEEE-1100,2.2.67) [60].

- **Swell** is an increase in rms voltage or current at the power frequency for durations from (a half cycle) to 1 minute (IEEE 1100,2.2.78) [60].

- **Transient** is a sub cycle disturbance in the ac waveform that is evidenced by a sharp, brief discontinuity of the waveform. It may be of either polarity and may be additive to, or subtractive from, the nominal waveform (IEEE-1100-2005, 2.2.83) [60]. A transient is a sudden, non-power frequency change in the steady state condition of voltage, current, or both, that includes both positive and negative polarity values.

- **Noise** is unwanted electrical signals that produce undesirable effects in the circuits of the control systems in which they occur (IEEE 1100, 2.2.49) [60].

- **A Harmonic** is the term used for current flow on power system at frequencies other than the principle frequency (i.e. 50Hz or 60Hz).

- **Flicker** is an impression of unsteadiness of the visual sensation induced by a light stimulus whose luminance or spectral distribution fluctuates with time (IEEE 1159-2009) [61].

- **Voltage interruption** is the disappearance of the supply voltage on one or more phases. It is usually qualified by an additional term indicating the duration of the interruption (e.g., momentary, temporary, sustained) (IEEE 1159-2009) [61].

- **Notch**: A switching (or other) disturbance in the normal power voltage waveform, lasting less than 0.5 cycles, which is initially of opposite polarity than the waveform and is thus subtracted from the normal waveform in terms of the

peak value of the disturbance voltage. This includes complete loss of voltage for up to 0.5 cycles [61].

3.3 Detection Using Morphology Edge Detection

The time location of power disturbances can be detected using the following procedures which have been developed as morphology edge detection, and can be seen in Figure 3.1.

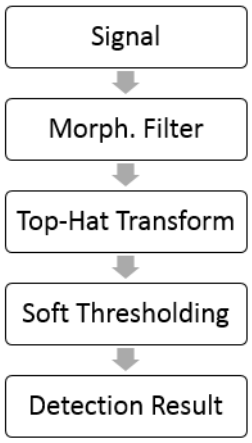

Figure 3.1: Morphology edge detection

3.3.1 Morphological Filter

In this strategy, firstly the input signal is filtered using a morphological filter. This is based-on an open-close filter (OCF) and a close-open filter (COF). The mathematical expression for a OCF:

$$OCF(f) = (f \circ g_1) \bullet g_2 \tag{3.3.1}$$

where: g_1 = structuring element 1; g_2 = structuring element 2

whilst that for an COF is:

$$COF(f) = (f \bullet g_1) \circ g_2 \tag{3.3.2}$$

The morphology filter can be written as follows:

$$\psi = [OCF(f) + COF(f)]/2 \tag{3.3.3}$$

3.3.2 Morphology Gradient

MM can be used in the detection of power quality problems. It has a good capability to detect not only the location of the faults, but also their duration in the time domain [62]. One of the techniques in detecting the edge of an image or a signal is a morphology gradient. There are some fundamental principles of edge detection operators in mathematical morphology based on boundary detection of the internal and external boundary. The internal boundary (β_1) can be found using a dilation operator on the edge detection and it is denoted by:

$$\beta_1 = f - (f \ominus g) \tag{3.3.4}$$

Using the erosion edge detection operator, the external boundary (β_2) of the signal can be found which is denoted by:

$$\beta_2 = (f \oplus g) - f \tag{3.3.5}$$

The basic morphological gradient (MG) is defined as an arithmetic difference between the dilation and the erosion by the elementary structuring element (B) of the considered grid. This means that the MG is the subtraction of an erosion (ε) from a dilation (δ), and can be denoted by ρ:

$$\rho_B = \delta_B - \varepsilon_B \tag{3.3.6}$$

In order to detect either the internal or the external boundary of an edge, the *half gradient* can be used. The *half gradient* by erosion or internal gradient ρ^- is defined as the difference between the original image (i_d) and the eroded image:

$$\rho_B^- = i_d - \varepsilon_B \tag{3.3.7}$$

The $half\ gradient$ by dilation or external gradient ρ^+ is defined as the difference between the dilated image and the original image:

$$\rho_B^+ = \delta_B - i_d \tag{3.3.8}$$

The internal and external gradient are complementary operators:

$$\rho^- = \rho^{+c} \tag{3.3.9}$$

$$\rho = \rho^+ + \rho^- \tag{3.3.10}$$

The *thick gradient* will be generated if the size of the SE is greater than 1. It gives the maximum variation in a neighborhood of size n.

$$\rho_{nB} = \delta_{nB} - \varepsilon_{nB} \tag{3.3.11}$$

where;

- δ_{nB} = dilation of image
- ε_{nB} = erosion of image

Directional Gradients are defined by replacing the isotropic SE with a line segment L in a given direction α:

$$\rho_{L\alpha} = \delta_{L\alpha} - \varepsilon_{L\alpha} \tag{3.3.12}$$

In order to obtain an accurate result, the directional perpendicular to the smallest directional gradient should also be considered rather than just defining the largest directional gradient [63].

The mathematic formula of the morphology gradient is:

$$f_{grad} = (f \oplus g) - (f \ominus g) \tag{3.3.13}$$

The gradient peaks are located on the edges, but the internal and external gradients are located at each side of the edges. The internal and external gradients should be thinner than the gradient. The values of all gradients will be positive or non-negative when the value of the structuring element is bigger or equal to zero.

The effect of the morphology gradient on a signal is shown in Figure 3.2.

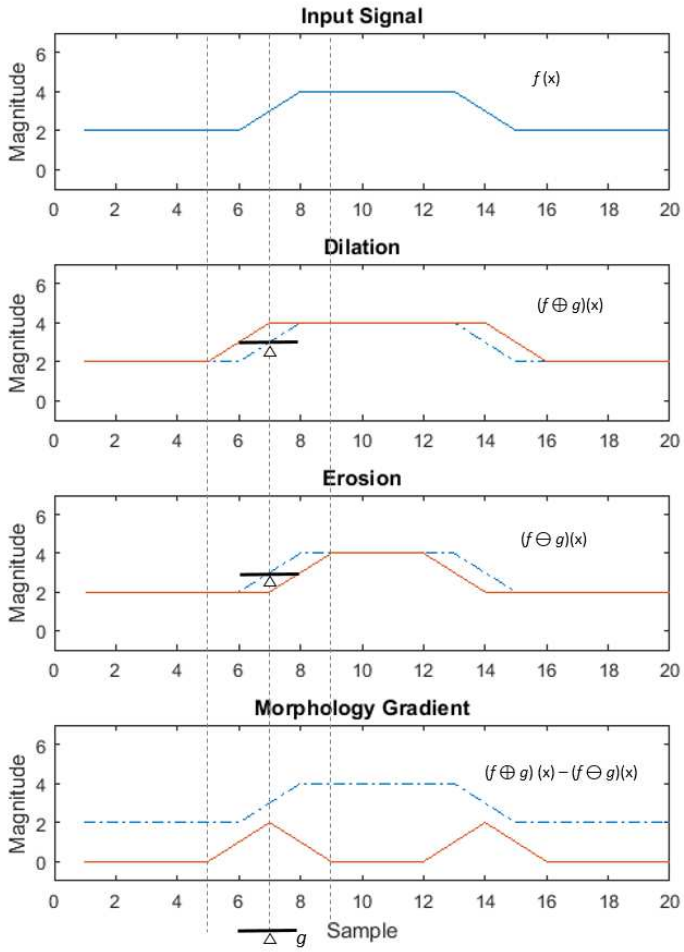

Figure 3.2: Morphology gradient

3.3.3 Top-Hat Transform

In order to extract the features of the signal for the time location of disturbances, the top-hat transform is applied after the Morphology gradient process.

There are two type of the top-hat transform which are described as follows:

The white top-hat transform (T_{w}) is the difference between the input and its opening by some structuring element, and it can be denoted by:

$$T_w(f) = f - (f \circ g) \tag{3.3.14}$$

The black top-hat transform (T_{b}) is the difference between the closing and the input, and is given by:

$$T_b(f) = (f \bullet g) - f \tag{3.3.15}$$

In this step, the white top-hat transform was used. Applying the top-hat transform of the morphological gradient (f_{HAT}) using the flat SE to find the time location of disturbances can be denoted by:

$$f_{\mathrm{HAT}} = f_{\mathrm{grad}} - (f_{\mathrm{grad}} \circ g) \tag{3.3.16}$$

where: f_{grad} = morphology gradient of the filtered signal.

By using a top-hat transform, the crest signal of disturbances are extracted by the opening process, but the signal still has some noise. In order to clean the noise up from the signal, the soft threshold τ_s is applied:

$$\tau_s = \sigma\sqrt{2\log N} \tag{3.3.17}$$

where *N* is the total sampling number and σ is denoted by:

$$\sigma = (\sum_{n=0}^{N-1} |f_{\mathrm{HAT}}(n)|/N)/0.6745 \tag{3.3.18}$$

The morphological edge detection results f_{ed} can be:

$$f_{ed} = \begin{cases} 0 & ; f_{\mathrm{HAT}} \leq \tau_s \\ f_{\mathrm{HAT}} & ; f_{\mathrm{HAT}} > \tau_s \end{cases} \tag{3.3.19}$$

3.3.4 Morphological Skeletonization

The morphological skeletonization (S_{f}) method is introduced in order to improve the accuracy of the results. The basics of skeletonization can be denoted by the following formula:

$$S = (f \ominus k_g) - ((f \ominus k_g) \circ g) \tag{3.3.20}$$

where: k_g = sequence of k erosion.

3.3.5 Time Location of Disturbances

In order to find the time location of disturbances, the values of the signal that are more than 0.1 are projected to 1 using the following equation:

$$f_{loc} = f_{grad} > 0.1 \tag{3.3.21}$$

Using this equation, not only the disturbances in the system, but also noise can be detected and plotted in 3D.

3.4 Simulation and Result

A Matlab simulation was undertaken to identify the time location of some disturbances in the system, such as voltage sag, voltage swell and interruption, under

noise-free and noisy condition. Different sizes of SE were used such as, 3 for morphology gradient and 5 for the top-hat method while the sampling frequency was 6.4 kHz.

The important step of measurement is to obtain samples of the event waveforms. It is necessary that the sampling rate and the resolution of the signal are adequate to record the disturbance. Due to the fact that the monitor is also used to obtain the harmonic spectrum, typical samples per cycle are 128 or 256 [64]. The IEC 61000-4-30 [65] standard does not give any direct information on sampling rate and resolution for voltage dip measurements. However, in most cases the same equipment will be used for obtaining information on the harmonic spectrum,which will require a sampling rate of at least 80 samples per cycle 128 or 256 being typical values. Voltage sampling is synchronized with the system frequency. In this way the sampling frequency is not expressed as a constant number of samples per second but as the constant number of samples per cycle [66].

By choosing 128 samples per cycle, the sampling frequency becomes 6.4 kHz for a 50Hz power signal. This sampling frequency is used for optimized monitoring and recording, a digital fault recorder with 16/32 bit micro-controller operates in acquisition sample rate up to 128 samples per cycle (6.4kHz @ 50Hz).

In this simulation, the signal with three type of disturbances was used. All of this input signals were generated by using the equation in Matlab based on the IEEE Standard 1159-2009. The equations for normal signal (V_{nor}), sag (V_{sag}), swell (V_{swe}), and interruption (V_{int}) were denoted as follows:

$$\begin{aligned} V_{nor} &= 10\cos(2\pi f_0 t_0) \\ V_{sag} &= -5\sin(2\pi f_0 t_1) \\ V_{swe} &= -18\sin(2\pi f_0 t_1) \\ V_{int} &= -0.0002\sin(2\pi f_0 t_1) \end{aligned} \tag{3.4.1}$$

where f_0 is the frequency of the signal (50Hz) and t_0 and t_1 are the duration of the signal.

Number of samples for each signal is 1234 samples with the sampling frequency at 6.4kHz. All of the disturbances were set occurring at 44.06ms as the start point and at 93.13 as the end point with the total duration of the signal was 192.8ms. Figure 3.3 shows the input signal with this three type of disturbances.

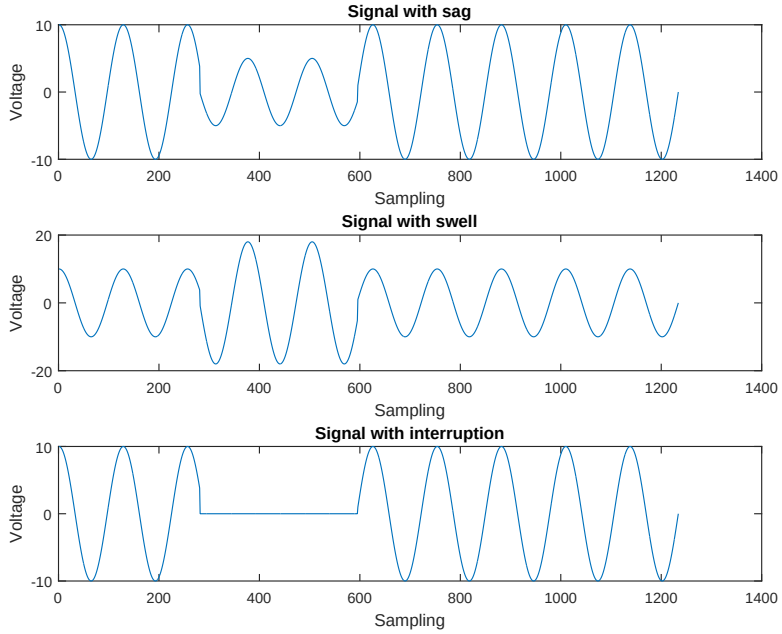

Figure 3.3: Input signal with sag, swell and interruption disturbances, respectively

The first step of this method is applying the morphology filter and morphology gradient for a signal with disturbances. Then by using the top-hat method, the initial starting and ending of the PQ event can be detected. The final step is using projection of the signal values greater than 0.1 to 1 to determine the location of disturbances in the system.

Figure 3.4 shows the simulation results of noise-free disturbances respectively (a) disturbance signal, (b) morphology gradient, (c) top-hat transform, and (d) result

of detecting sag location in the system. In this figure, sag disturbances can be detected using morphology gradient and the top-hat transform, and then projected to 1 to ensure the time location of the disturbances as can see in Figure 3.4.

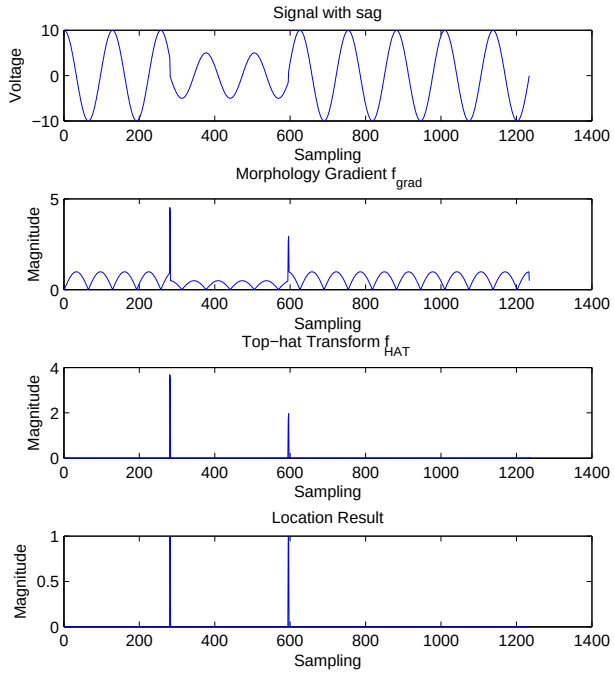

Figure 3.4: Location of voltage sag

For sag disturbances, the filtered signal (f_{grad}) is plotted in 3D in spherical coordinates to make the visual identification easier. This 3D is generated by using cylinder function in Matlab. This function generates x-, y-, and z-coordinates of a unit cylinder. The Matlab command to generate cylinder as follows:

[X,Y,Z] = cylinder(r)

This means the $x-$, $y-$, and z-coordinates of a cylinder using r to define a profile curve. Cylinder treats each element in r as a radius at equally spaced heights along the unit height of the cylinder. There are 20 equally spaced points around the cylinder's circumference.

The cylindrical object can be drawn using surf or mesh, or draw it immediately by not

providing output arguments. In this research, all 3D cylinder is drawn using surf as follows:

surf(X,Y,Z)

This command creates a three-dimensional surface plot where this function plots the values in matrix Z as heights above a grid in the $x - y$ plane defined by X and Y. For the color data, this function also uses Z to make the color is proportional to the height.

The result in 3D for the sag can be seen in Figure 3.5. In this figure, the starting and the ending of the sag disturbances can be seen in blue and green respectively. The gap between them shows the lower voltages compared to the normal voltages. By plotting the signal in 3D, the location of the disturbances can be identified with their different colors and different shapes. In this case, the beginning of the disturbance are in blue while the ending is in green. The starting and the ending point of the disturbances can be identified by their shapes, which features a bigger circle than the other signal.

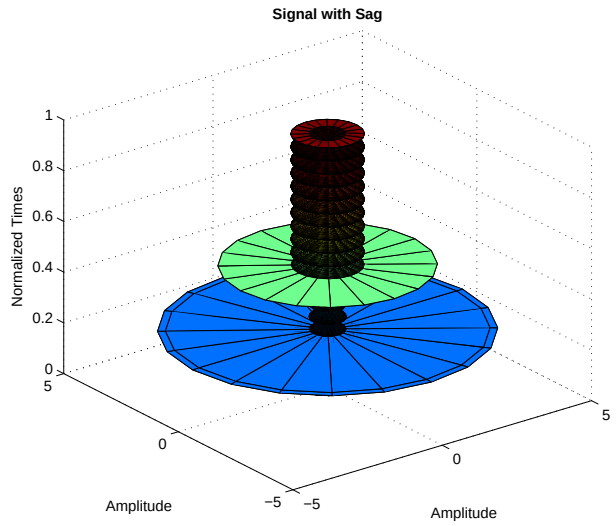

Figure 3.5: Location of voltage sag in 3D

The same method was applied to voltage swell and voltage interruption and the result can be seen in Figures 3.6 to 3.9 respectively. In these figures, the time location of the disturbances can be detected accurately both at the starting points and ending points in the system. So, the duration of the power quality disturbances occurring in the system can be

measured.

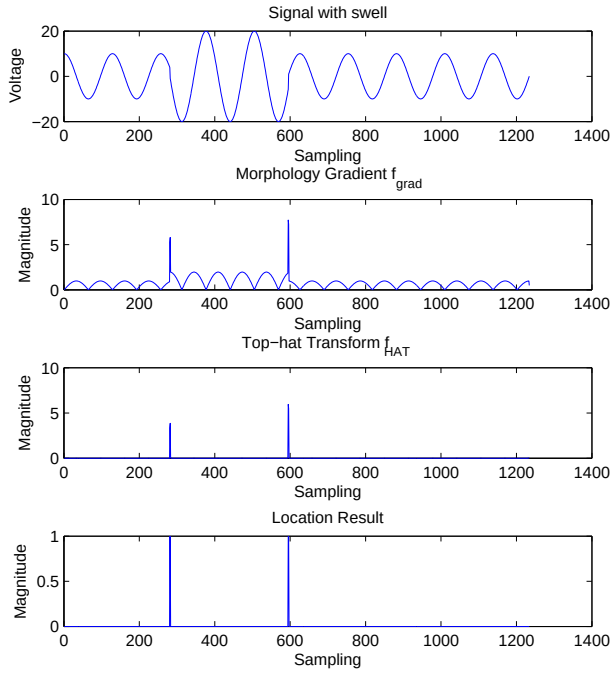

Figure 3.6: Location of voltage swell

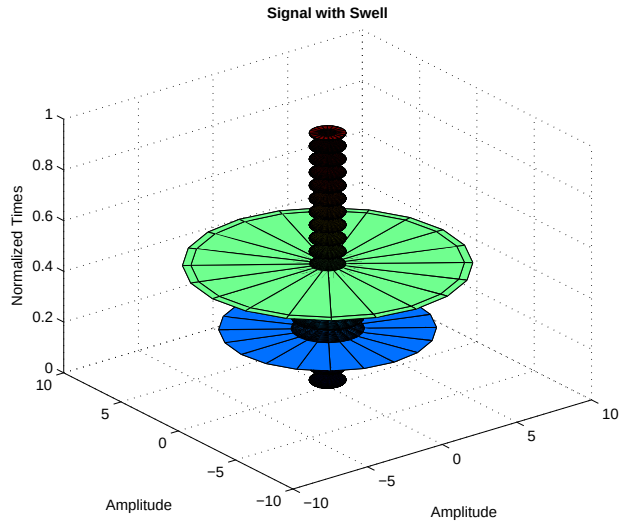

Figure 3.7: Location of voltage swell in 3D

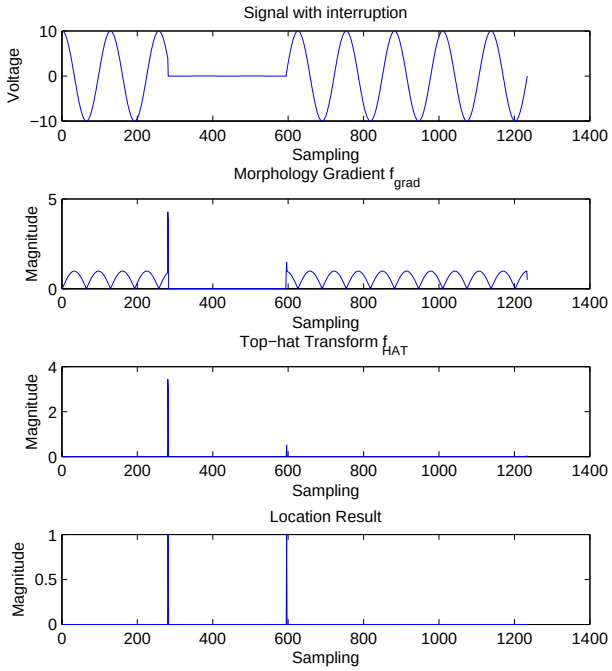

Figure 3.8: Location of voltage interruption

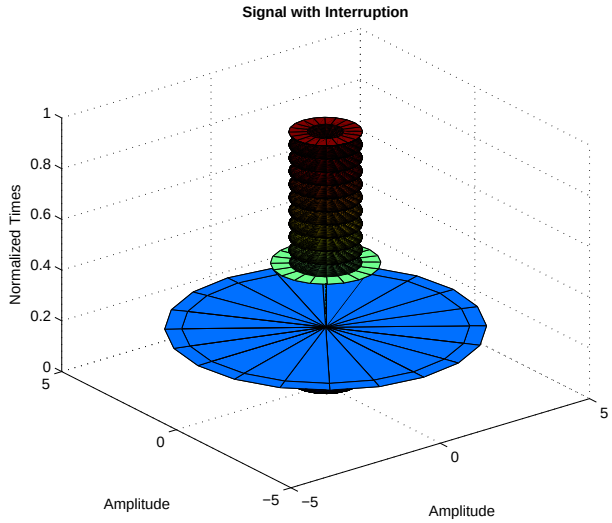

Figure 3.9: Location of voltage interruption in 3D

In this simulation, the errors in the detection of various disturbances location can be seen

in Table 3.1. T_s in the table is the sampling period that equals to $1/f_s$. The result shows that average error of this method is the same as the f_{ed} method [13] with value less than half sampling frequency.

Table 3.1: Simulation result of disturbances detection using morphology gradient and skeletonization of mathematical morphology in 3D

PQ Events	Voltage Sag		Voltage Swell		V. Interruption	
	begin	end	begin	end	begin	end
Actual position (ms)	44.06	93.13	44.06	93.13	44.06	93.13
Result (ms)	43.91	93.13	44.06	92.97	44.06	93.13
error/Ts	1	0	0	1	1	0
error/Ts*	0.5	0.5	0	1	0	1

Note: * = Result using f_{ed} [13]

3.4.1 Time Location of Noise

Noise, or interference, can be defined as undesirable electrical signals, which distort or interfere with an original (or desired) signal. Noise could be transient (temporary) or constant [67]. Sources of noise can be external or internal to the system itself. Noises from external system can be enter the system by electromagnetic interference (EMI), radio frequency interference (RFI), cross talk, or natural origins like electrostatic interference, lightning and electrical storms while internal noises may be caused due to thermal noise or imperfections in the electrical design. Large electrical motors being switched on, fluorescent lighting tubes, solid-state converters or drive systems can also produce noise.

Noise that is produced by switching off a device can cause a notching, this is one type of disturbances that has the sharp inverted spikes in the waveform of the signal. High frequency harmonic currents are also generated by this power switching that will lead the EMI in the signal circuit.

In this section, skeletonization is applied to the signal to recognize the availability of the noise. By detecting this noise, some steps such as, low pass filter or smoothing operation to reduce the effect of noise can be undertaken especially for noise-sensitive equipment. It is also able to control harmonic currents, avoiding ground loops or adding adequate shielding for the sensitive equipment.

The system without noise can be seen in Figure 3.10. In this figure, normal signal is plotted to 3D and 2D to evaluate the occurrence of the noise in the system. When the system was injected by various Gaussian white noise with SNR (signal to noise ratio) value from -20 to 50dB, this method has the capability to detect the location of the noise as can be seen in Figures 3.11 to 3.15. As can be seen in these figures for the 3D projection, the noise can be detected as a black color along the colored cylinder. The different visuals for this noise can be seen in the 2D projection.

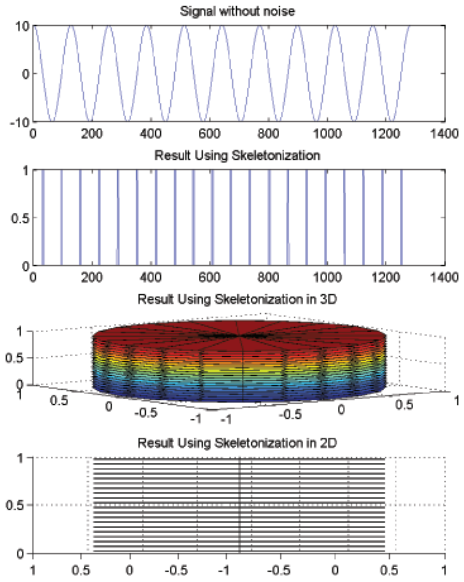

Figure 3.10: Skeletonization without noise

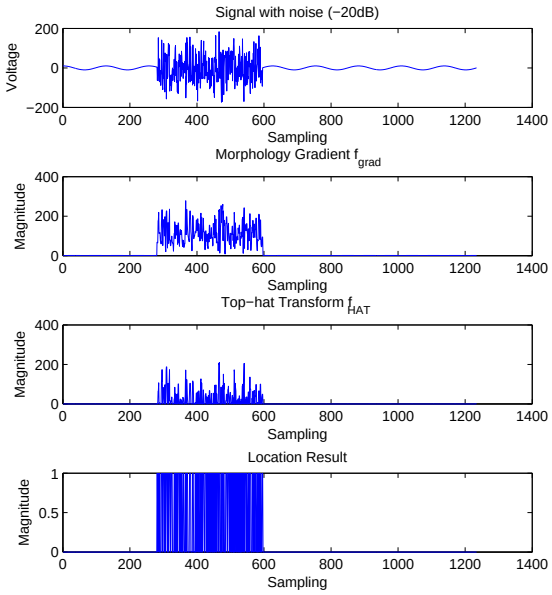

Figure 3.11: Signal with SNR = -20dB

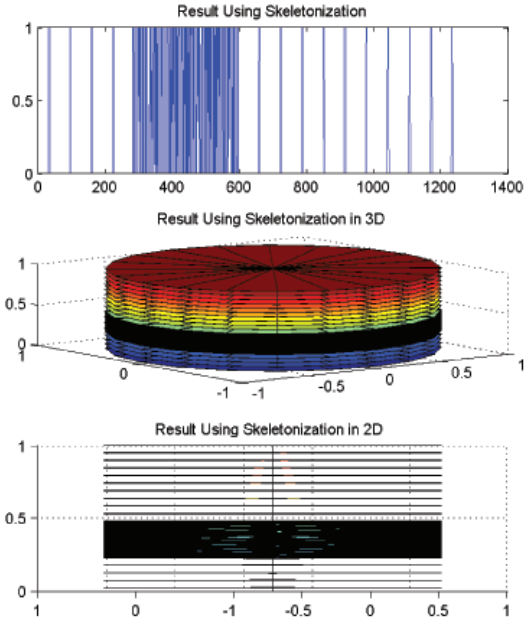

Figure 3.12: Skeletonization with -20dB noise

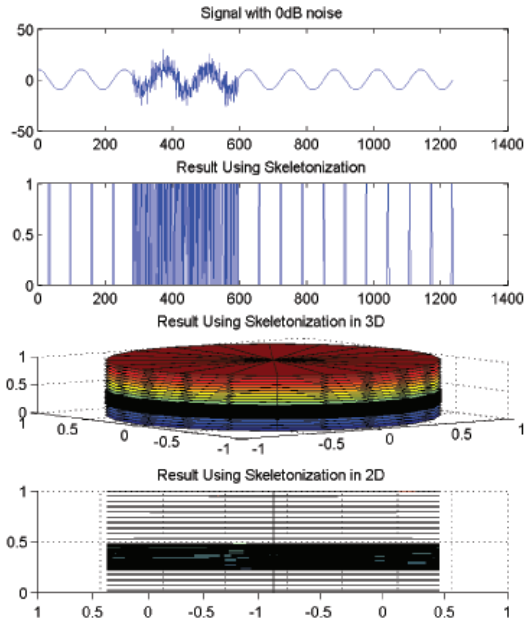

Figure 3.13: Skeletonization with 0dB noise

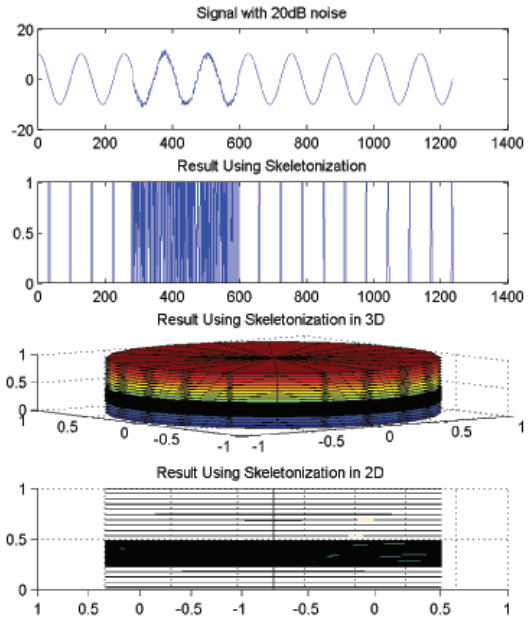

Figure 3.14: Skeletonization with 20dB noise

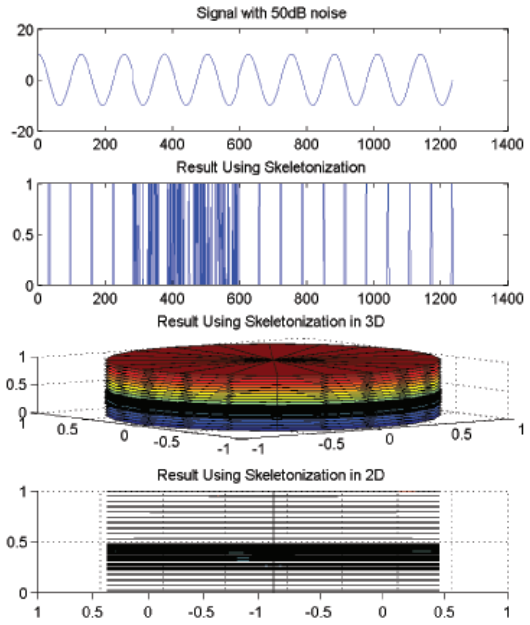

Figure 3.15: Skeletonization with 50dB noise

3.5 Combined Strategy

In this section, a new combination of skeletonization and morphology edge detection is proposed to find the accurate time location of disturbances. This proposed strategy is simulated by using MATLAB for voltage sag, swell, and interruption, both for noise-free signals and for signals that contains noise. Firstly, signals with disturbances were filtered using a morphology gradient then they were run through a morphology edge detection using a top-hat transform with a flat structuring element. After that, a soft thresholding was applied to eliminate background noise. In this step, the result still has an error, so skeletonization was introduced to the system to find accurate time location of disturbances both in noise-free signals and for signals with noise.

The time location of power disturbances can be detected using some procedures that have been developed using the combination of morphological edge detection and skele-

tonization and it can be seen in Figure 3.16.

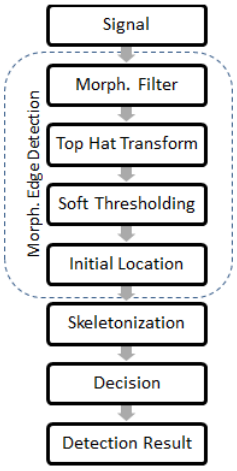

Figure 3.16: Proposed method

3.5.1 Criteria

The results of the detection on the signal that is presented in the previous section still have some errors. These error are eliminated using skeletonization. By using skeletonization, all magnitude signals after background noise elimination are projected to 1. The decision result of the time location of disturbances can be found by using decision method as follows:

$$S_{\mathrm{f}} = \begin{cases} 1 & ; S_{\mathrm{n}} = 1, S_{\mathrm{n-1}} = 0 \\ 0 & ; Else \end{cases} \tag{3.5.1}$$

where n= sampling point

An example of a swell signal is shown in Figure 3.17. The morphology edge detection has some error in the detection of the start and end point of this disturbance. By using skeletonization and then applying the criteria, a better result for detection can be achieved. This is shown in Figure 3.18.

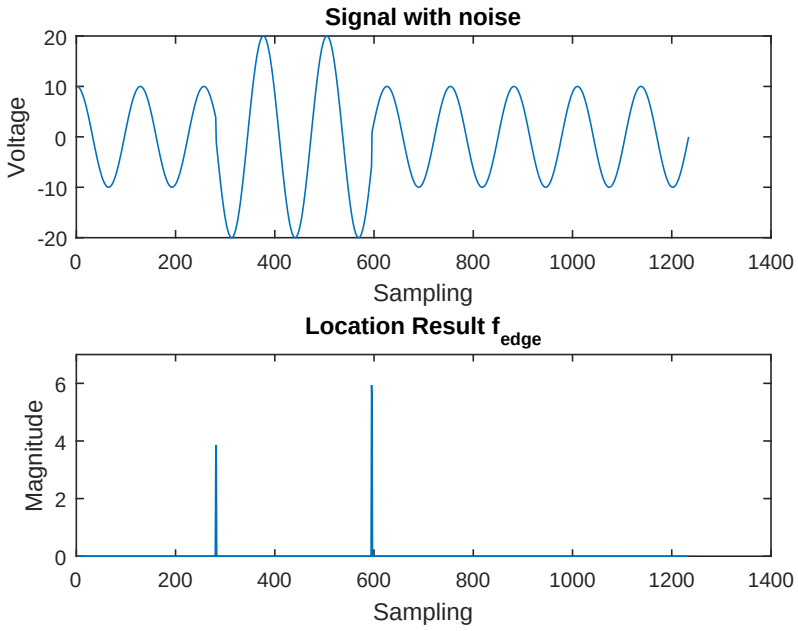

Figure 3.17: An example of edge detection on swell signal

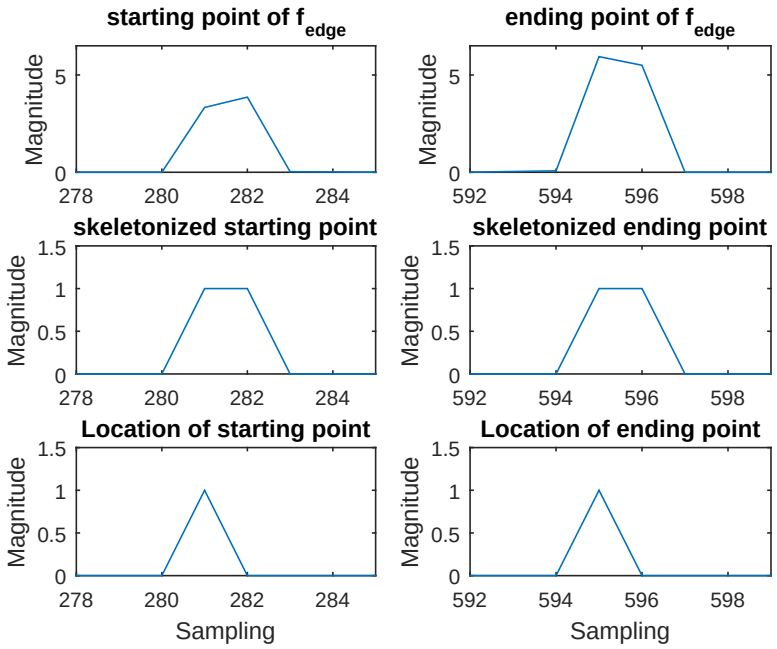

Figure 3.18: Effect skeletonization and applied criteria

From Figure 3.18 show that more than one point (2 or 3) is detected as the results of the morphology edge detection. In this method, the time between that 2 point is chosen as the detection result. This strategy leads to errors in the detection of PQ disturbances. Using skeletonization which criteria, this error can be eliminated to find an accurate result in the detection process.

3.6 Simulation and Result for Combined Strategy

3.6.1 Time Location of Disturbances under Noise-free Signal

A Matlab simulation was used to identify the time location of some disturbances in the system, such as voltage sag, voltage swell and interruption, under noise-free. The length size of SE was chosen using adaptive selection [13], and the sampling frequency was 6.4 kHz.

The first step for this method is applying a morphology filter and morphology gradient for a noise-free signal with voltage sag disturbances. Then, by using the top-hat method, the initial starting and ending PQ event could be detected. The next step is implementing soft thresholding in order to eliminate the background noise. After that, an edge detection strategy was used to determine the location of disturbances in the system. In this step, the result still had an error.

The final step is adding morphological skeletonization to the edge detection morphology results to find the more accurate result as shown in Figure 3.19.

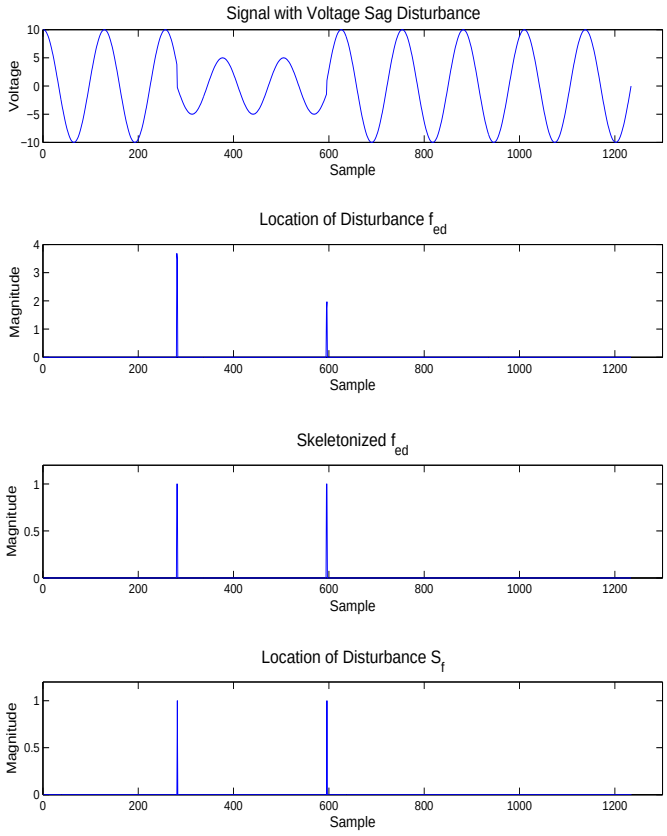

Figure 3.19: Location of voltage sag after skeletonization

The same method was applied to voltage swell and to voltage interruption and the results can be seen in Figure 3.20 and 3.21 respectively. In these figures, the time location of the disturbances can be detected accurately both for the start points and end points in the system for voltage swell. There is no error in the start point, but a slight error in the end point of the disturbance for the voltage interruption simulation.

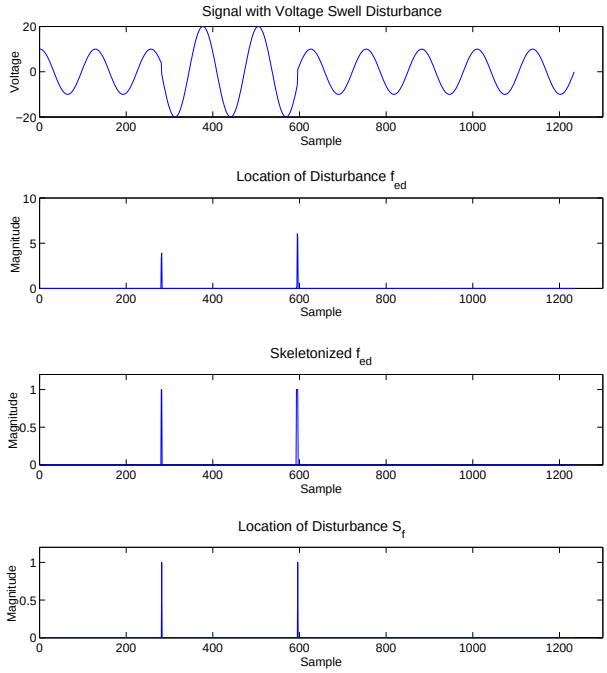

Figure 3.20: Location of voltage swell after skeletonization

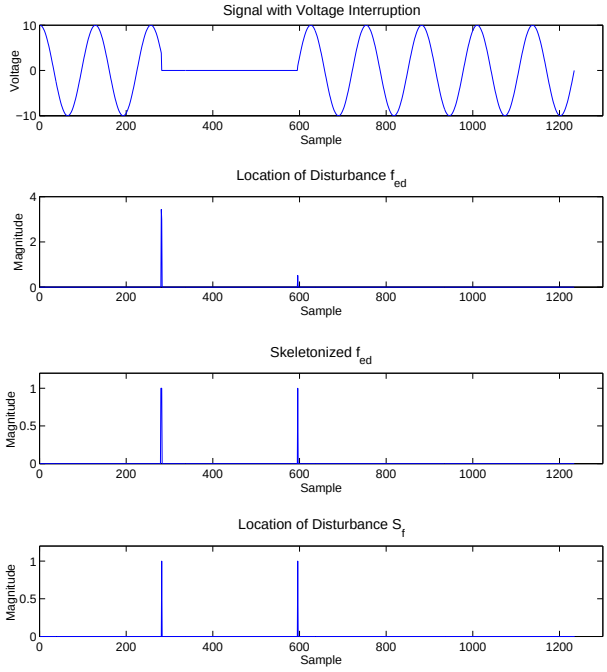

Figure 3.21: Time location of voltage interruption after skeletonization

3.6.2 Time Location of Disturbances in Signal with Noise

The simulation is carried out not only for noise-free signal but also for the disturbances with a signal corrupted by noise. Additive White Gaussian Noise (AWGN) was added to the signal with a signal to noise ratio (SNR) of 30 dB. The other parameters have the same values as for the simulation of the noise-free signal. Using the proposed method, the location of the voltage sag, swell and interruption can be detected as seen in Figures 3.22 to 3.26 respectively.

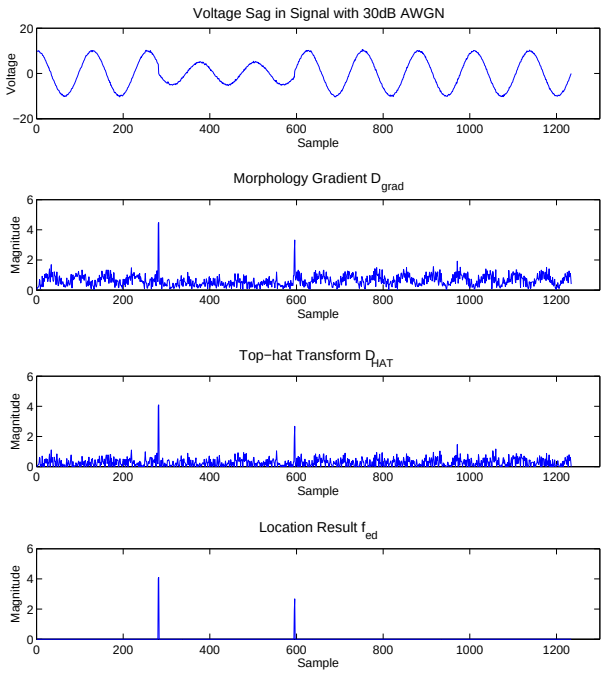

Figure 3.22: Location of Sag in 30dB signal using edge detection

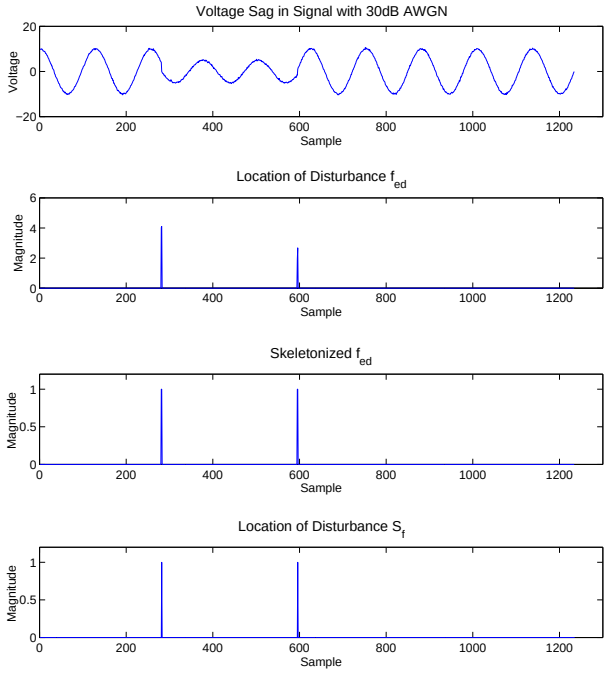

Figure 3.23: Time location of sag in 30dB signal after skeletonization

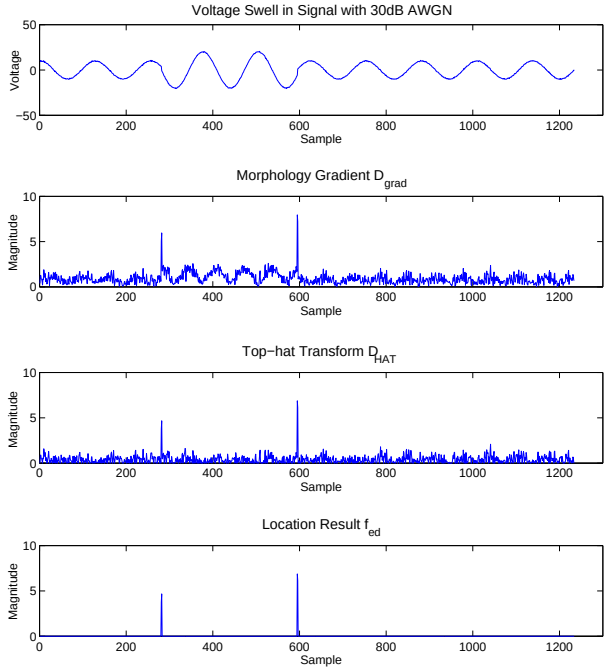

Figure 3.24: Time location of swell in 30dB signal using edge detection

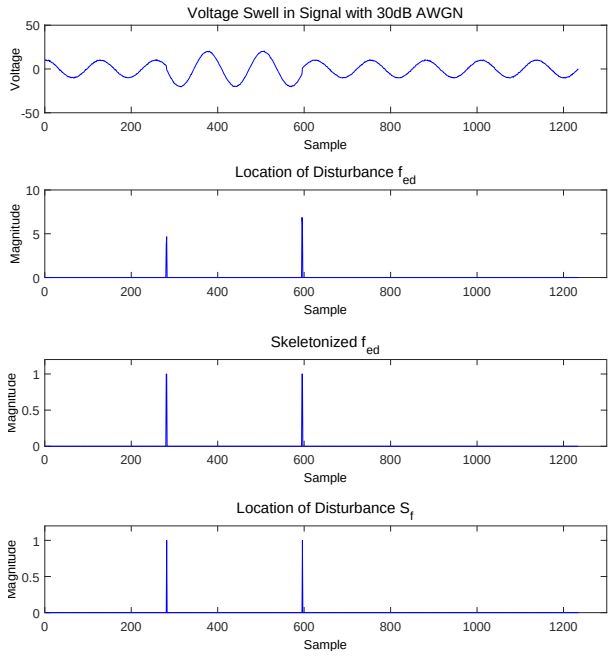

Figure 3.25: Time location of swell in 30dB signal using skeletonization

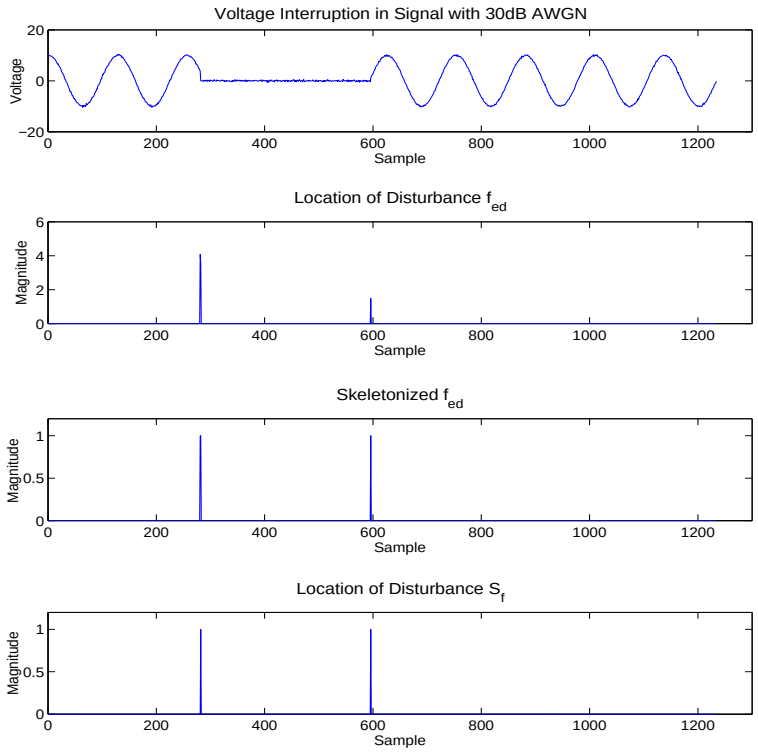

Figure 3.26: Time location of interruption in 30dB signal using skeletonization

The error results in the detection of various disturbances location can be seen in Table 3.2. T_{s} in the table is the sampling period that equals to $1/f_{\mathrm{s}}$ where f_{s} is the sampling frequency. The precise results without error are obtained for both voltage sag and swell disturbance. To detect voltage interruption disturbances, there is no error in detecting start point, but a slight error in detecting the end point.

The overall results show that average error of this method is better than the f_{ed} method [13] with average value 0.1667 sampling period, far less than half the sampling period. So, adding skeletonization to the results of morphology edge detection can improve the performance of the method by about 33% (from 0.5 or 50% to 0.1667 or 16.67%) in the detection time location of power disturbances.

Table 3.2: Simulation result of combination of skeletonization and morphology edge detection for detecting time location of power system disturbances

PQ Events	Voltage Sag		Voltage Swell		V. Interruption	
	begin	end	begin	end	begin	end
Actual position (ms)	43.91	92.97	43.91	92.97	43.91	92.97
Result (ms)	43.91	92.97	43.91	92.97	43.91	93.13
error/T_s	0	0	0	0	0	1
error/T_s^*	0.5	0.5	0	1	0	1

Note: * = Result using f_{ed} [13]

3.6.3 Reliability of the Proposed Method

The simulation was also applied to the block signal to check the reliability of the proposed strategy to detect every changing in the block signal. The result shows that the proposed method can detect the changing of the signal accurately as can seen in Figure 3.27.

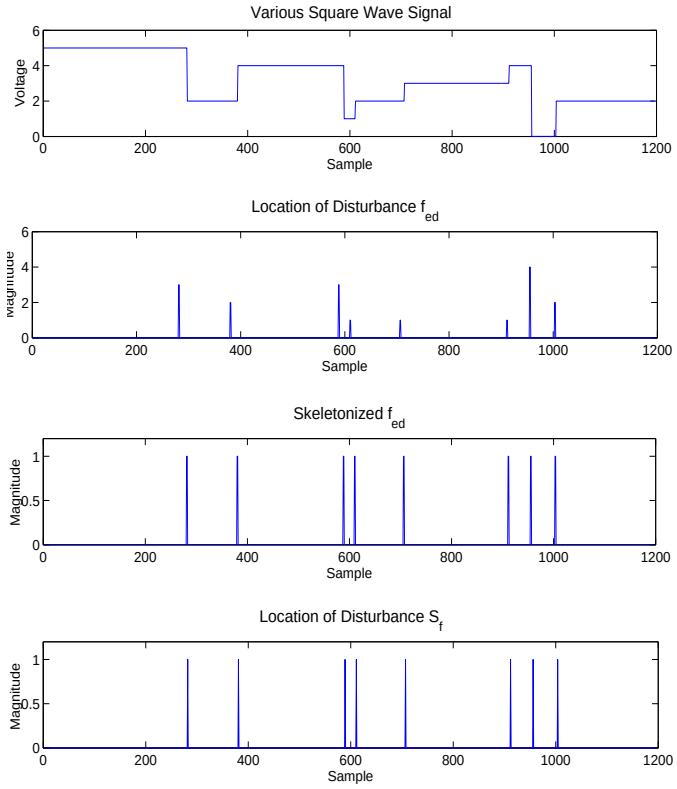

Figure 3.27: Time location of various block signals using skeletonization

3.7 Summary

This chapter presents one method for the detection of disturbances in power systems by using morphology gradient as an initial detection. The top-hat transform is then applied and the projection of top-hat transform has the same result as morphology edge detection in locating power quality disturbances especially for voltage swell, sag and interruption with an average error for this method is just half the sampling period. By plotting the filtered signal to 3D, the location of the disturbances can be identified with the different colors and different shapes as pattern recognition.

Skeletonization was introduced in this chapter to detect the noise in the system. The noise location in the system can be shown as black color on 3D plotting, and it can be identified when it has a signal to ratio (SNR) less than 50dB. Plotting the results of the

detection of disturbances and also the location of the noise in 3D makes it easier to identify the location of disturbances with or without noise with different color and shapes for pattern recognition.

A new combination of skeletonization and morphology edge detection is also proposed to accurately detect the time location of disturbances in the system for both noise-free signals and signal with noise. The average error for this proposed method is just 0.1667 sampling period, far less than half the sampling period. Using this proposed method, accurate results without error can be reached in locating the voltage swell and sag. The overall results show the reduction of the error significantly by 33% compared to the result of morphology edge detection strategy. With a different SNR, there is no error in the detection of disturbances for SNR higher than 30dB while the error increased gradually for the signal with SNR less than 30dB.

Chapter 4

Signal to Image Matrix Conversion Strategy for Detecting Time Location of Power Quality Disturbances

4.1 Introduction

In this chapter, a new strategy is presented to find the location of disturbances. The idea of this strategy is changing a signal to an image then as an image, it is processed by using some of the methods that are used in image processing. In this proposed method, a signal as a one-dimensional discrete-time signal is converted to two-dimensional discrete-time signals or images. Boundary extraction of the Mathematical Morphology (MM) is used in one step of this method. The image result is then evaluated by using control chart to find the location time of disturbances. The beginning and ending of disturbances can be seen as a violation points in control chart. The simulation results show that this proposed strategy has the capability in detecting the location time of disturbances accurately compared to existing methods.

4.2 Procedures in the Detection of Disturbances Location

The time location of power disturbances can be detected using the procedures that have been developed. The flow diagram of this proposed strategy using signal to image matrix conversion (SIMC) strategy can be seen in Figure 4.1. The idea of this strategy is converting a signal to an image. As an image, the disturbances can be detected using methods that have been applied in the image processing area.

4.2.1 SIMC Strategy

Matrix Distributing

A general form of sinusoidal function is:

$$y(t) = A\ sin(\omega t + \varphi) \tag{4.2.1}$$

A one-dimensional discrete-time signal is typically represented by an array as a row vector. This function is a row vector, with a $(1 \times n)$ matrix or a horizontal arrangement of numbers. It is also denoted by the vector symbol as follows

$$\mathbf{y} = [y_{1j}]_{j=1,\ldots,n} = [y_{11}\ y_{12}\ \cdots\ y_{1n}] \tag{4.2.2}$$

This row vector then is distributed to a general $(m \times n)$ matrix, and is denoted by the matrix symbol $A = [a_{i,j}]_{i=1,\ldots,m;\ j=1,\ldots,n}$ or

$$A_{m,n} = \begin{pmatrix} a_{1,1} & a_{1,2} & \cdots & a_{1,n} \\ a_{2,1} & a_{2,2} & \cdots & a_{2,n} \\ \vdots & \vdots & \ddots & \vdots \\ a_{m,1} & a_{m,2} & \cdots & a_{m,n} \end{pmatrix} \tag{4.2.3}$$

This arrangement is typically used for two-dimensional discrete-time signals or images.

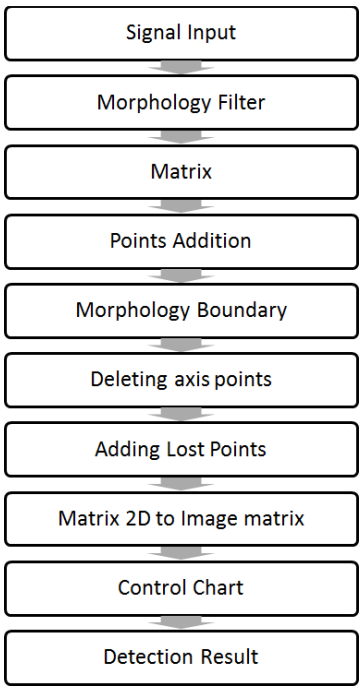

Figure 4.1: Flow diagram proposed strategy

The strategy to make a $(m \times n)$ matrix can be described by using an example as follows:

First set a value for ϱ of the matrix that will be a maximum value of the signal. In order to put the signal into the matrix, it needs to refer that there is no (0,0) in the matrix as found in the cartesian coordinate system. So, the (0,0) should be in the first row and in the center of the length of column (C_t) of the new matrix. By using this strategy, the coordinate of (0,0) will be (a_{1,C_t}) in the matrix.

$$\textbf{(0,0)} \Longrightarrow (a_{1,C_t}) \tag{4.2.4}$$

C_t is set a half of the length of the matrix by rounding up it. If the length of a new matrix is 10 or 9, then (C_t) = 5, as a result, the coordinate of (0,0) will be $(a_{1,5})$

Then signal $y(1 \times n) = [y_{11}\ y_{12}\ \ldots\ y_{1n}]$ will become:

$$A_{m,n} = A_{(\alpha,\varrho)} = \begin{pmatrix} a_{1,1} & a_{1,2} & \cdots & a_{1,\varrho} \\ a_{2,1} & a_{2,2} & \cdots & a_{2,\varrho} \\ \vdots & \vdots & \ddots & \vdots \\ a_{\alpha,1} & a_{\alpha,2} & \cdots & a_{\alpha,\varrho} \end{pmatrix} \tag{4.2.5}$$

In this proposed strategy, the value of the signal is converted to **1** as a *white pixel* in the image matrix while **0** is a *black* pixel. Before doing this, the ratio of the matrix need to be found in order to make it fit in the new matrix by rounding the matrix y to matrix y_1 then finding M_{max}, the maximum value of y_1. The ratio of the matrix can be denoted as:

$$R_m = C_t / M_{max} \tag{4.2.6}$$

After that, the matrix y should be multiplied by R_m. The new matrix is denoted as:

$$M_{a(1,\alpha)} = R_m.y \tag{4.2.7}$$

By using this, the condition for Equation 4.2.7:

$$A_{(\alpha,\varrho)} = \{\alpha, \varrho \mid \alpha = n, \forall(C_t + M_{a(1,\alpha)}) \in \varrho\} \tag{4.2.8}$$

$$A_{(\alpha,\varrho)} = \begin{cases} 1 \quad if \quad \varrho = C_t + M_{a(1,\alpha)} \\ \\ 0 \quad if \quad \varrho \neq C_t + M_{a(1,\alpha)} \end{cases} \tag{4.2.9}$$

where:

$\alpha = n$

$\varrho = 2 \times C_t$

$C_t =$ Center of the length of column of the new matrix

$M_{a(1,\alpha)} =$ The new matrix after multiplication.

For examples:

y = [0 1.1 2.2 3 2 1 0 -1.1 -2.3 -2.9 -2 -1 0]

so the length of the matrix = 13.

The value of the matrix y should be rounded to make it as an integer. Then the matrix becomes:

y_1 = [0 1 2 3 2 1 0 -1 -2 -3 -2 -1 0]

Then finding the maximum value of the matrix y_1 (M_{max}) and it is 3.

So, if $C_t = 4$, the value of $R_m = 4/3 = 1.33$ then this value is need to be rounded to 1 as an integer.

$M_{a(1,\alpha)}$ = [0 1 2 3 2 1 0 -1 -2 -3 -2 -1 0]

then:

According to Equation 4.2.9, the component of matrix $A_{(\alpha,\varrho)}$ that will have a 1 value are:

$a_{1,4+0} = a_{1,4} = 1;$ $a_{2,4+1} = a_{2,5} = 1$

$a_{3,4+2} = a_{3,6} = 1;$ $a_{4,4+3} = a_{4,7} = 1$

$a_{5,4+2} = a_{5,6} = 1;$ $a_{6,4+1} = a_{6,5} = 1$

$a_{7,4+0} = a_{7,4} = 1;$ $a_{8,4-1} = a_{8,3} = 1$

$a_{9,4-2} = a_{9,2} = 1;$ $a_{10,4-3} = a_{10,1} = 1$

$a_{11,4-2} = a_{11,2} = 1;$ $a_{12,4-1} = a_{12,3} = 1$

$a_{13,4+0} = a_{11,4} = 1;$

Then the matrix size will be:

$(\alpha, \varrho) = (n, 2C_t) = (13 \times 8).$

The new matrix will be as follows:

$$A_{(\alpha,\varrho)} = \begin{pmatrix} 0 & 0 & 0 & \mathbf{1} & 0 & 0 & 0 & 0 \\ 0 & 0 & 0 & 0 & \mathbf{1} & 0 & 0 & 0 \\ 0 & 0 & 0 & 0 & 0 & \mathbf{1} & 0 & 0 \\ 0 & 0 & 0 & 0 & 0 & 0 & \mathbf{1} & 0 \\ 0 & 0 & 0 & 0 & 0 & \mathbf{1} & 0 & 0 \\ 0 & 0 & 0 & 0 & \mathbf{1} & 0 & 0 & 0 \\ 0 & 0 & 0 & \mathbf{1} & 0 & 0 & 0 & 0 \\ 0 & 0 & \mathbf{1} & 0 & 0 & 0 & 0 & 0 \\ 0 & \mathbf{1} & 0 & 0 & 0 & 0 & 0 & 0 \\ \mathbf{1} & 0 & 0 & 0 & 0 & 0 & 0 & 0 \\ 0 & \mathbf{1} & 0 & 0 & 0 & 0 & 0 & 0 \\ 0 & 0 & \mathbf{1} & 0 & 0 & 0 & 0 & 0 \\ 0 & 0 & 0 & \mathbf{1} & 0 & 0 & 0 & 0 \end{pmatrix} \tag{4.2.10}$$

Another example for this strategy:

y = [0 1.2 2 3.3 2.4 1 0.1 -1 -1.9 -2.8 -2.5 -1 0]

If the C_t is 7, then R_m will be 2. So the first step is changing the matrix y, then the result can be seen as follows:

$M_{a(1,\alpha)}$= [0 2 4 7 5 2 0 -2 -4 -6 -5 -2 0]

Because the C_t is 7, the size of the matrix A will be (13×14). Then by using Equation 4.2.5 and 4.2.7, the matrix becomes:

$$A_0 = \begin{pmatrix}
0 & 0 & 0 & 0 & 0 & 0 & \mathbf{1} & 0 & 0 & 0 & 0 & 0 & 0 & 0 \\
0 & 0 & 0 & 0 & 0 & 0 & 0 & 0 & \mathbf{1} & 0 & 0 & 0 & 0 & 0 \\
0 & 0 & 0 & 0 & 0 & 0 & 0 & 0 & 0 & 0 & \mathbf{1} & 0 & 0 & 0 \\
0 & 0 & 0 & 0 & 0 & 0 & 0 & 0 & 0 & 0 & 0 & 0 & 0 & \mathbf{1} \\
0 & 0 & 0 & 0 & 0 & 0 & 0 & 0 & 0 & 0 & 0 & \mathbf{1} & 0 & 0 \\
0 & 0 & 0 & 0 & 0 & 0 & 0 & 0 & \mathbf{1} & 0 & 0 & 0 & 0 & 0 \\
0 & 0 & 0 & 0 & 0 & 0 & \mathbf{1} & 0 & 0 & 0 & 0 & 0 & 0 & 0 \\
0 & 0 & 0 & 0 & \mathbf{1} & 0 & 0 & 0 & 0 & 0 & 0 & 0 & 0 & 0 \\
0 & 0 & \mathbf{1} & 0 & 0 & 0 & 0 & 0 & 0 & 0 & 0 & 0 & 0 & 0 \\
\mathbf{1} & 0 & 0 & 0 & 0 & 0 & 0 & 0 & 0 & 0 & 0 & 0 & 0 & 0 \\
0 & \mathbf{1} & 0 & 0 & 0 & 0 & 0 & 0 & 0 & 0 & 0 & 0 & 0 & 0 \\
0 & 0 & 0 & 0 & \mathbf{1} & 0 & 0 & 0 & 0 & 0 & 0 & 0 & 0 & 0 \\
0 & 0 & 0 & 0 & 0 & 0 & \mathbf{1} & 0 & 0 & 0 & 0 & 0 & 0 & 0
\end{pmatrix} \tag{4.2.11}$$

Adding Some Points

Matrix A_0 that is the result from the previous step should be changed to make the points connect to each other. So some points are need to be added for the matrix as follows:

$$A_1 = \begin{pmatrix} 0 & 0 & 0 & 0 & 0 & 0 & \mathbf{1} & \mathbf{1} & 0 & 0 & 0 & 0 & 0 & 0 \\ 0 & 0 & 0 & 0 & 0 & 0 & \mathbf{1} & \mathbf{1} & \mathbf{1} & 0 & 0 & 0 & 0 & 0 \\ 0 & 0 & 0 & 0 & 0 & 0 & \mathbf{1} & \mathbf{1} & \mathbf{1} & \mathbf{1} & \mathbf{1} & 0 & 0 & 0 \\ 0 & 0 & 0 & 0 & 0 & 0 & \mathbf{1} & \mathbf{1} & \mathbf{1} & \mathbf{1} & \mathbf{1} & \mathbf{1} & \mathbf{1} & \mathbf{1} \\ 0 & 0 & 0 & 0 & 0 & 0 & \mathbf{1} & \mathbf{1} & \mathbf{1} & \mathbf{1} & \mathbf{1} & \mathbf{1} & 0 & 0 \\ 0 & 0 & 0 & 0 & 0 & 0 & \mathbf{1} & \mathbf{1} & \mathbf{1} & 0 & 0 & 0 & 0 & 0 \\ 0 & 0 & 0 & 0 & 0 & 0 & \mathbf{1} & \mathbf{1} & 0 & 0 & 0 & 0 & 0 & 0 \\ 0 & 0 & 0 & 0 & \mathbf{1} & \mathbf{1} & \mathbf{1} & 0 & 0 & 0 & 0 & 0 & 0 & 0 \\ 0 & 0 & \mathbf{1} & \mathbf{1} & \mathbf{1} & \mathbf{1} & \mathbf{1} & 0 & 0 & 0 & 0 & 0 & 0 & 0 \\ \mathbf{1} & \mathbf{1} & \mathbf{1} & \mathbf{1} & \mathbf{1} & \mathbf{1} & \mathbf{1} & 0 & 0 & 0 & 0 & 0 & 0 & 0 \\ 0 & \mathbf{1} & \mathbf{1} & \mathbf{1} & \mathbf{1} & \mathbf{1} & \mathbf{1} & 0 & 0 & 0 & 0 & 0 & 0 & 0 \\ 0 & 0 & 0 & 0 & \mathbf{1} & \mathbf{1} & \mathbf{1} & 0 & 0 & 0 & 0 & 0 & 0 & 0 \\ 0 & 0 & 0 & 0 & 0 & 0 & \mathbf{1} & \mathbf{1} & 0 & 0 & 0 & 0 & 0 & 0 \end{pmatrix} \tag{4.2.12}$$

Boundary Extraction

After adding these points, boundary extraction [68] is applied to the matrix as follows:

$$\beta(A_1) = A_1 - (A_1 \ominus \text{SE}) \tag{4.2.13}$$

where SE = Structuring element.

Using this method, with the SE as a flat structuring element, the matrix A_1 becomes a new matrix A_2 as follows:

$$A_2 = \begin{pmatrix}
0 & 0 & 0 & 0 & 0 & 0 & \mathbf{1} & \mathbf{1} & 0 & 0 & 0 & 0 & 0 & 0 \\
0 & 0 & 0 & 0 & 0 & 0 & \mathbf{1} & 0 & \mathbf{1} & 0 & 0 & 0 & 0 & 0 \\
0 & 0 & 0 & 0 & 0 & 0 & \mathbf{1} & 0 & 0 & \mathbf{1} & \mathbf{1} & 0 & 0 & 0 \\
0 & 0 & 0 & 0 & 0 & 0 & \mathbf{1} & 0 & 0 & 0 & 0 & \mathbf{1} & \mathbf{1} & \mathbf{1} \\
0 & 0 & 0 & 0 & 0 & 0 & \mathbf{1} & 0 & 0 & \mathbf{1} & \mathbf{1} & \mathbf{1} & 0 & 0 \\
0 & 0 & 0 & 0 & 0 & 0 & \mathbf{1} & 0 & \mathbf{1} & 0 & 0 & 0 & 0 & 0 \\
0 & 0 & 0 & 0 & 0 & 0 & \mathbf{1} & \mathbf{1} & 0 & 0 & 0 & 0 & 0 & 0 \\
0 & 0 & 0 & 0 & \mathbf{1} & \mathbf{1} & \mathbf{1} & 0 & 0 & 0 & 0 & 0 & 0 & 0 \\
0 & 0 & \mathbf{1} & \mathbf{1} & 0 & 0 & \mathbf{1} & 0 & 0 & 0 & 0 & 0 & 0 & 0 \\
\mathbf{1} & \mathbf{1} & 0 & 0 & 0 & 0 & \mathbf{1} & 0 & 0 & 0 & 0 & 0 & 0 & 0 \\
0 & \mathbf{1} & \mathbf{1} & \mathbf{1} & 0 & 0 & \mathbf{1} & 0 & 0 & 0 & 0 & 0 & 0 & 0 \\
0 & 0 & 0 & 0 & \mathbf{1} & \mathbf{1} & \mathbf{1} & 0 & 0 & 0 & 0 & 0 & 0 & 0 \\
0 & 0 & 0 & 0 & 0 & 0 & \mathbf{1} & 1 & 0 & 0 & 0 & 0 & 0 & 0
\end{pmatrix} \tag{4.2.14}$$

Deleting Axis points

This matrix still has an axis that does not represent a value of the signal, so it has to be eliminated.

$$A_3 = \begin{pmatrix} 0 & 0 & 0 & 0 & 0 & 0 & \mathbf{0} & \mathbf{1} & 0 & 0 & 0 & 0 & 0 & 0 \\ 0 & 0 & 0 & 0 & 0 & 0 & 0 & 0 & \mathbf{1} & 0 & 0 & 0 & 0 & 0 \\ 0 & 0 & 0 & 0 & 0 & 0 & 0 & 0 & 0 & \mathbf{1} & \mathbf{1} & 0 & 0 & 0 \\ 0 & 0 & 0 & 0 & 0 & 0 & 0 & 0 & 0 & 0 & 0 & \mathbf{1} & \mathbf{1} & \mathbf{1} \\ 0 & 0 & 0 & 0 & 0 & 0 & 0 & 0 & 0 & \mathbf{1} & \mathbf{1} & \mathbf{1} & 0 & 0 \\ 0 & 0 & 0 & 0 & 0 & 0 & 0 & 0 & \mathbf{1} & 0 & 0 & 0 & 0 & 0 \\ 0 & 0 & 0 & 0 & 0 & 0 & \mathbf{0} & \mathbf{1} & 0 & 0 & 0 & 0 & 0 & 0 \\ 0 & 0 & 0 & 0 & \mathbf{1} & \mathbf{1} & 0 & 0 & 0 & 0 & 0 & 0 & 0 & 0 \\ 0 & 0 & \mathbf{1} & \mathbf{1} & 0 & 0 & 0 & 0 & 0 & 0 & 0 & 0 & 0 & 0 \\ \mathbf{1} & \mathbf{1} & 0 & 0 & 0 & 0 & 0 & 0 & 0 & 0 & 0 & 0 & 0 & 0 \\ 0 & \mathbf{1} & \mathbf{1} & \mathbf{1} & 0 & 0 & 0 & 0 & 0 & 0 & 0 & 0 & 0 & 0 \\ 0 & 0 & 0 & 0 & \mathbf{1} & \mathbf{1} & 0 & 0 & 0 & 0 & 0 & 0 & 0 & 0 \\ 0 & 0 & 0 & 0 & 0 & 0 & \mathbf{0} & \mathbf{1} & 0 & 0 & 0 & 0 & 0 & 0 \end{pmatrix} \tag{4.2.15}$$

Adding lost points

The consequence of deleting axis points is that some points that are a representation of the value of the signal are lost too. In order to resolve this problem, some points are added to the matrix. So the final matrix will be:

$$A_{(\alpha,\varrho)} = \begin{pmatrix} 0 & 0 & 0 & 0 & 0 & 0 & \mathbf{1} & \mathbf{1} & 0 & 0 & 0 & 0 & 0 & 0 \\ 0 & 0 & 0 & 0 & 0 & 0 & 0 & 0 & \mathbf{1} & 0 & 0 & 0 & 0 & 0 \\ 0 & 0 & 0 & 0 & 0 & 0 & 0 & 0 & 0 & \mathbf{1} & \mathbf{1} & 0 & 0 & 0 \\ 0 & 0 & 0 & 0 & 0 & 0 & 0 & 0 & 0 & 0 & 0 & \mathbf{1} & \mathbf{1} & \mathbf{1} \\ 0 & 0 & 0 & 0 & 0 & 0 & 0 & 0 & 0 & \mathbf{1} & \mathbf{1} & \mathbf{1} & 0 & 0 \\ 0 & 0 & 0 & 0 & 0 & 0 & 0 & 0 & \mathbf{1} & 0 & 0 & 0 & 0 & 0 \\ 0 & 0 & 0 & 0 & 0 & 0 & \mathbf{1} & \mathbf{1} & 0 & 0 & 0 & 0 & 0 & 0 \\ 0 & 0 & 0 & 0 & \mathbf{1} & \mathbf{1} & 0 & 0 & 0 & 0 & 0 & 0 & 0 & 0 \\ 0 & 0 & \mathbf{1} & \mathbf{1} & 0 & 0 & 0 & 0 & 0 & 0 & 0 & 0 & 0 & 0 \\ \mathbf{1} & \mathbf{1} & 0 & 0 & 0 & 0 & 0 & 0 & 0 & 0 & 0 & 0 & 0 & 0 \\ 0 & \mathbf{1} & \mathbf{1} & \mathbf{1} & 0 & 0 & 0 & 0 & 0 & 0 & 0 & 0 & 0 & 0 \\ 0 & 0 & 0 & 0 & \mathbf{1} & \mathbf{1} & 0 & 0 & 0 & 0 & 0 & 0 & 0 & 0 \\ 0 & 0 & 0 & 0 & 0 & 0 & \mathbf{1} & \mathbf{1} & 0 & 0 & 0 & 0 & 0 & 0 \end{pmatrix} \tag{4.2.16}$$

The comparison of the final result versus the first converting matrix can be seen in Figure 4.2.

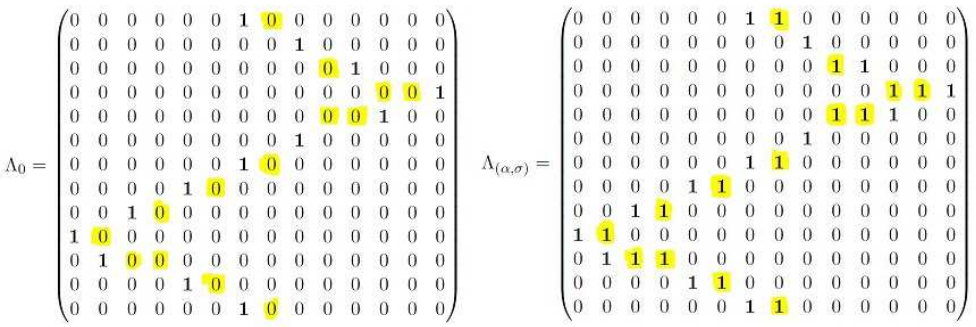

Figure 4.2: Comparison of first vs final result

From the first matrix, there are no connection points between each other. After the process has been applied to the first matrix, the final matrix had some additional connected points. The number of additional point depends on the size of the matrix and the elements of the matrix that has value 1. In this case, the number of additional points was 14.

Results of SIMC in Images

The images results in this strategy can be seen in Figure 4.3 to 4.5. In Figure 4.3, the value of the converted signal is represented by points. Then in Figure 4.4, the image of the signal has some additional points. Figure 4.5 is the image of the signal after the final process.

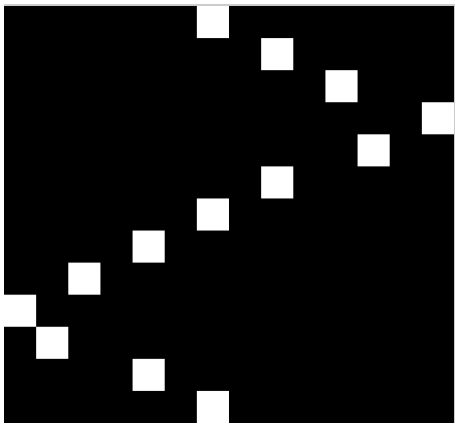

Figure 4.3: First converted image

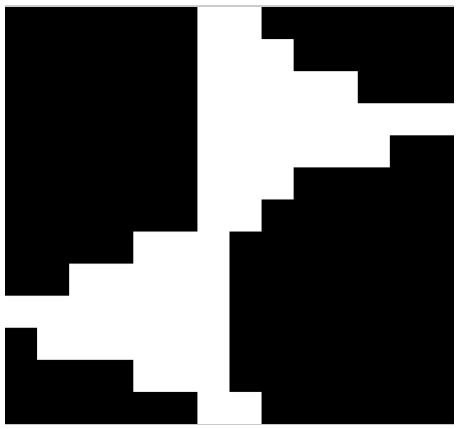

Figure 4.4: Image after points added

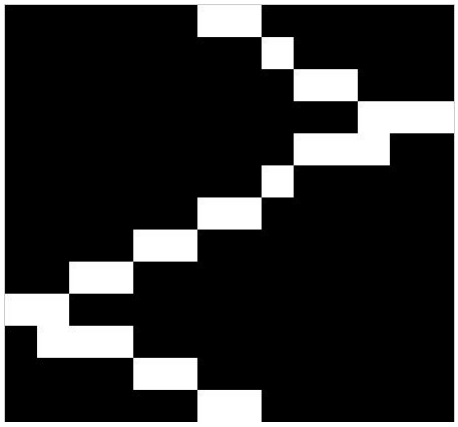

Figure 4.5: Final image

Changing the value of C_t to 100 gives the results is seen in Figures 4.6 to 4.8. All images will be wider than the ones before. The matrix size of this image will be (13×200).

Figure 4.6: First converted image with C_t = 100

Figure 4.7: Image after points added with C_t = 100

Figure 4.8: Final image with C_t = 100

The value of C_t can be chosen as an initial value based on the differentiation between the neighbourhood elements of Matrix y $(1 \times n)$. By using this, the size of matrix $A_{\alpha,\varrho}$ may be too high and it would not be handled by Matlab or it would take a long time to process to find the final matrix. So it is preferable to choose the initial value of C_t to make the conversion from a signal to an image matrix more flexible. When the value of the signal is

small (i.e. 5 volt), the final matrix is wider (Figure 4.6 - 4.8). On the other hand, when the value of the signal is high (380 volt), the final matrix shrink. This is because the process makes the signal fit to the size of the new matrix.

4.2.2 Detecting Location Time of Disturbances using SIMC

A **control charts** is applied to the matrix in order to detect the location of the disturbances, start time and end time of the disturbances. The control chart, developed by Walter A. Shewhart [69], is a graph used to study how a process changes over time. In a control chart, as shown in Figure 4.9, there are some main features such as:

- *Points* - They are quality characteristic in samples taken from the process at different times
- *Mean Value* - the mean calculation of all samples
- *A Center Line* - It is drawn at the value of the mean of the signal
- *Standard Error* - It is for all samples.
- *Upper and Lower Control Limits (UCL/LCL)* indicate the threshold at which the process output is considered statistically 'unlikely' and are drawn typically at 3 standard errors from the centre line

Other features that are on the chart:

- *Upper and lower warning or control limits* - is two standard errors above and below the centre line that are drawn as separate lines.
- *Division into zones*- with the addition of rules governing frequencies of observations in each zone
- *Annotation with events of interest*- as determined by the Quality Engineer in charge of the process's quality

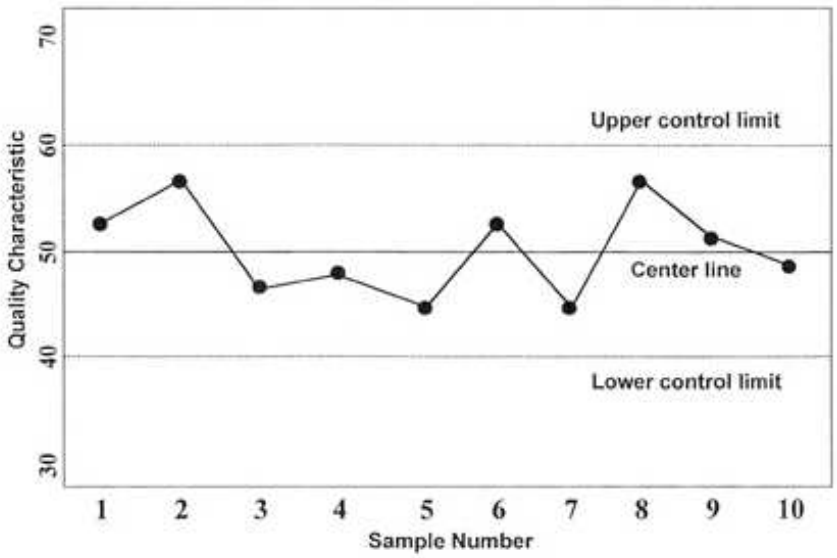

Figure 4.9: An example of the control chart

The location of disturbances in the chart can be seen as some violation points, where the first violation point is a start point of the disturbance while the second one is the end point. The last violation point is just the ending of the simulation only as it can be seen in Figure 4.10.

4.3 Simulation and Results of SIMC

The simulation for this proposed strategy was done by using Matlab. The signals with variety of disturbances, such as voltage sag, swell, and voltage interruption are used. Using the value of C_t 100, sampling period 6.4 kHz, the simulation results can be seen in the following figures.

Signal with Voltage Sag

The location time of the signal with voltage sag can be detected using this following steps from Figure 4.11 to **??**.

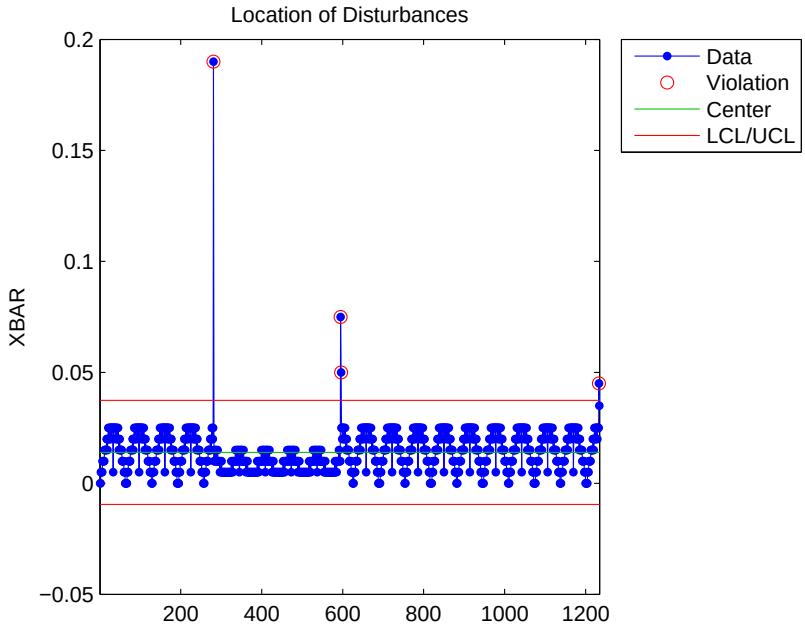

Figure 4.10: An example of control chart of location time of disturbance

The initial signal with voltage sag can be seen in Figure 4.11. After that, it was converted into image matrix. Then the points of the matrix are connected by adding some points, running boundary extracting process, deleting the axis and adding the lost points. The image of this process can be seen in Figure 4.12, while the detection of the location time of the voltage sag can be seen in Figure 4.13.

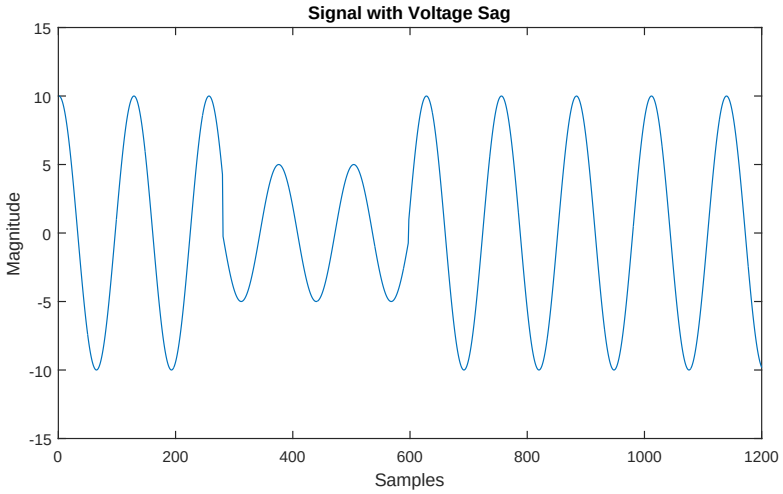

Figure 4.11: Signal with voltage sag

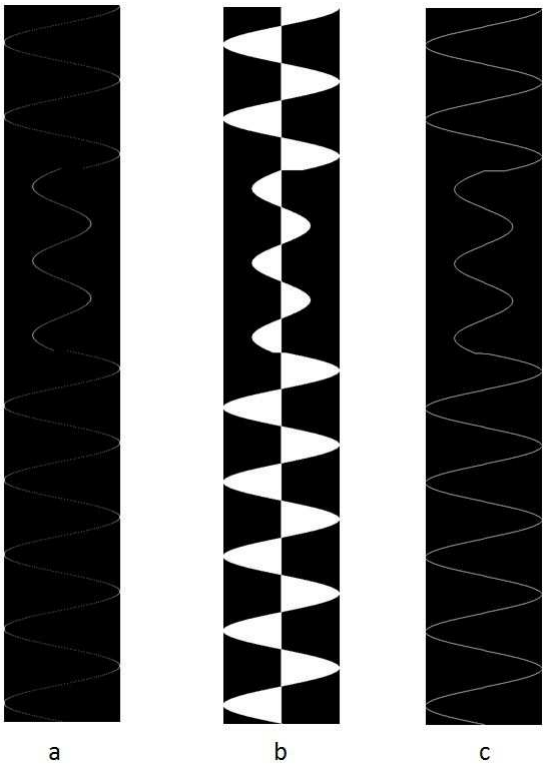

Figure 4.12: Image of signal

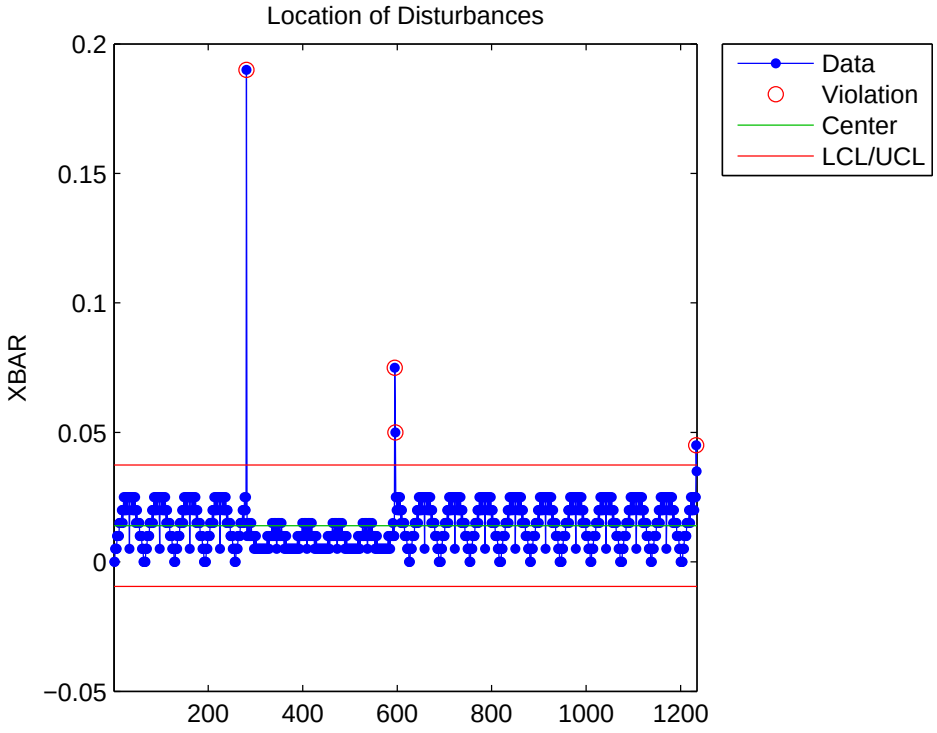

Figure 4.13: Location of voltage sag

By using control chart, the violation points can be detected as the location time of the disturbances. In Figure 4.13, the start and end time location of the voltage sag can be obtained.

Signal with Voltage Swell

Using the same process, the voltage swell (Figure 4.14) in the system can be detected and find the time location of this disturbances as shown in Figure 4.15.

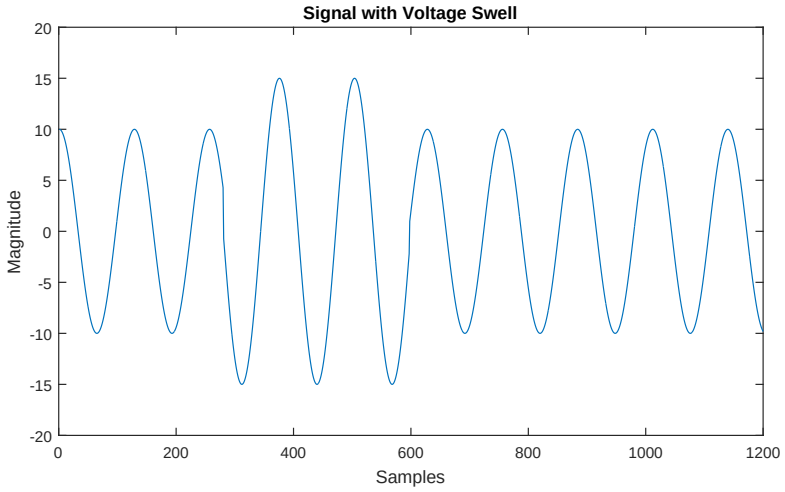

Figure 4.14: Signal with voltage swell

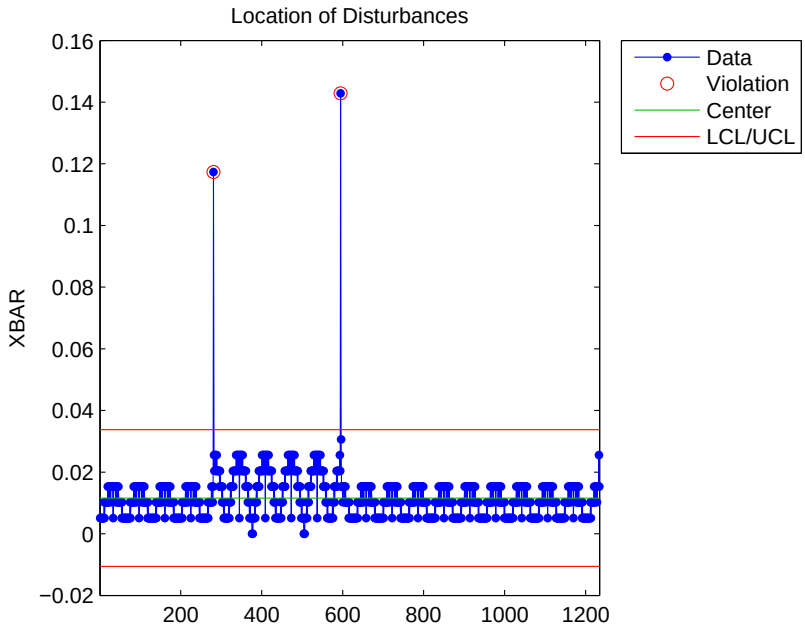

Figure 4.15: Location of voltage swell

Signal with Voltage Interruption

To detect the location time of the voltage interruption disturbance (Figure 4.16), the previous strategy was applied, and the result can be seen in Figure 4.17.

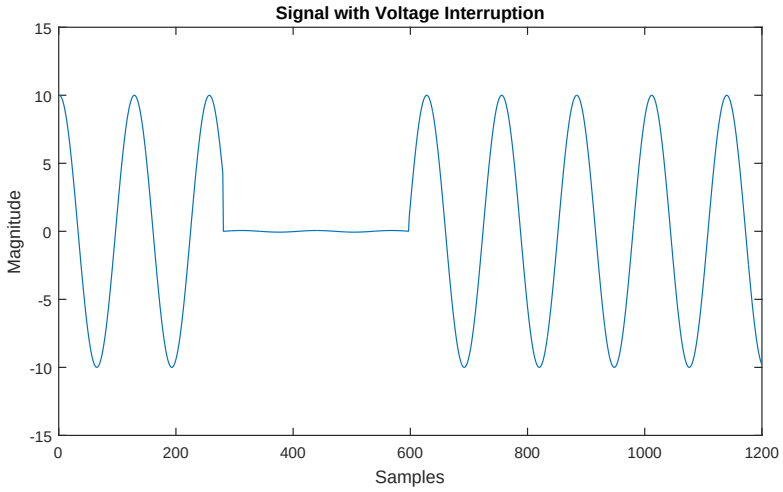

Figure 4.16: Signal with voltage interruption

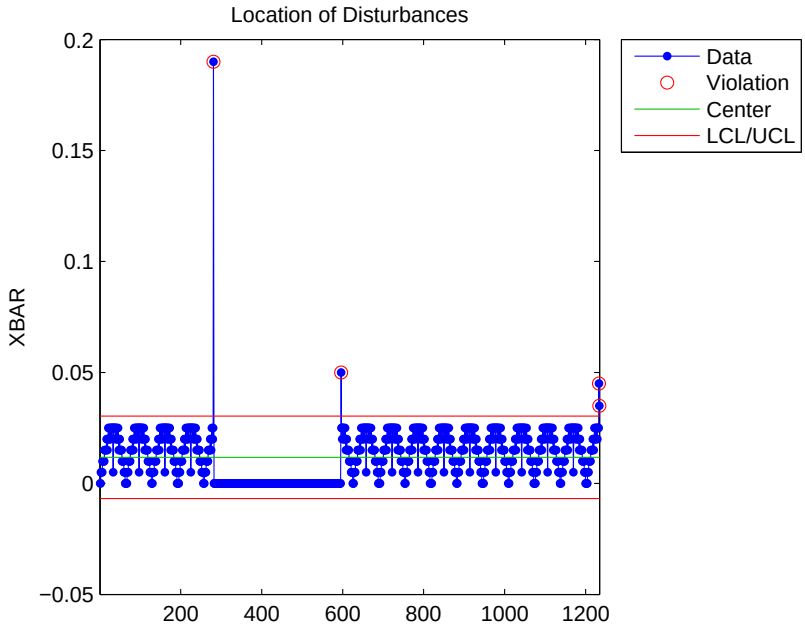

Figure 4.17: Location of voltage interruption

The location result of the proposed strategy compare to the f_{ed} method [13] can be seen in Table 4.1. The results show that the average of $error/Ts$ using the proposed method are half sampling period, and it was the same as the results of the f_{ed} method. The pro-

posed strategy generates a better result in the detection of the location time of the voltage interruption compare to f_{ed} method. It is be able to detect the location time of the voltage interruption precisely.

Table 4.1: Simulation results of the signal to image matrix conversion strategy for detecting the time location of power quality disturbances

PQ Events	Voltage Sag		Voltage Swell		V. Interruption	
	start	end	start	end	start	end
Proposed Strategy						
Actual position (ms)	44.06	93.13	44.06	93.13	44.06	93.13
Result (ms)	43.91	93.13	44.06	92.97	44.06	93.13
error/Ts	**1**	**0**	**0**	**1**	**0**	**0**
f_{ed} **Strategy**						
Result of (ms)	43.75	96.88	43.75	96.88	43.75	96.88
Result (ms)	43.83	96.95	43.75	97.03	43.75	97.03
error/Ts	**0.5**	**0.5**	**1**	**0**	**0**	**1**

For the different SNR (from 0 dB - 100 dB), this method has good results for SNR above 30 dB, and then the error is increased when the value of SNR is decreased. These results can be seen in Figure 4.18.

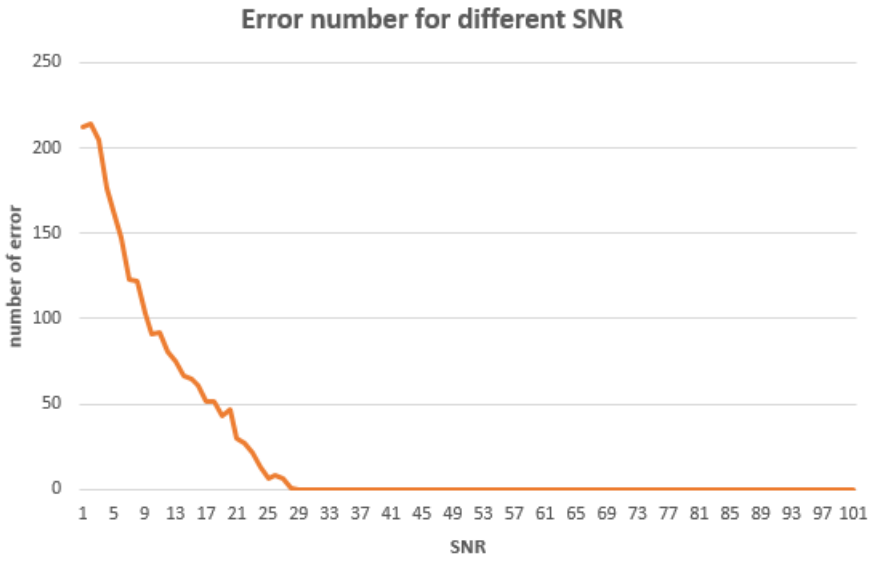

Figure 4.18: Error in different SNR

4.4 Signal to Image Matrix Conversion using Small Data Window

In this section, a new strategy for disturbance detection is presented based on the vector to matrix conversion with MM as presented in the previous section. This proposed method uses a small window size, and it call as Signal to Image Matrix Conversion using Small Data Window (SIMC-SDW). After the conversion of the vector to the matrix, then the mean value of each row of the new matrix is then calculated and compared with the mean of the normal signal in order to find the time location of the disturbances. The higher mean value of each row indicates the time location of disturbances. By using only 4 data samples, the detection process is fast and can be applied as a real time detection method.

The timing of power disturbances in power systems can be detected using the developed procedures shown in Figure 4.19. The proposed strategy uses the same conversion. Signals are converted into an image. An image processing strategy is then used to detect the distur-

bances in the power system. The signal is initially filtered using a Morphology Filter before being converted into a signal/image matrix. The location of disturbances can be detected by comparing the mean value of each row of the matrix with the mean value of the normal signal. The difference from the previous method is the number of samples, as only 4 samples are used. By choosing only 4 samples from 128 samples per cycle (for 6.4 kHz sampling frequency) the window size of the detection becomes very small, 1/32 cycle. Mathematical morphology is used in this strategy, which has the advantages of high-speed calculation and excellent de-noising performance [70]. This means that this strategy can be used for real time disturbances detection.

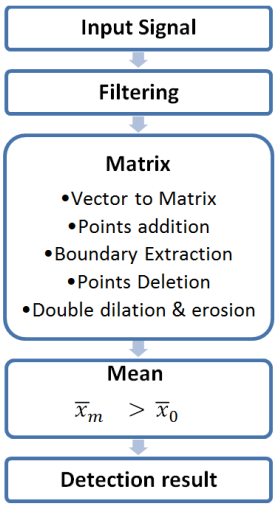

Figure 4.19: Block diagram of SIMC-SDW strategy

4.4.1 Matrix Distribution in SIMC-SDW Method

Vector to Matrix Conversion.

In this SIMC-SDW strategy, most of steps in the signal to image conversion are the same. Some changes will be presented as follows:

First, the length of the matrix should be set as the number of columns of the input vector. The number of columns should be twice the maximum value of the disturbances signal

that will be encountered. To handle voltage of disturbances to +-511 volts, the number of columns of the matrix is 1024 using integer values. In practice, this could be data acquired using a 10 bit or greater analog to digital converter. Therefore the range of the voltages was from -512 to +511 volts.

The number of columns of the vector (n) is converted to be the number of rows (m_0) of the matrix. In this example, the number of data that is used is 4, so m_0 is 4.

All values of the signal as a vector $y = [y_{1j}]$ are rounded as a new vector $y_r = [y_{1k}]$. By matrix distribution, the signal $[y_{1k}]$ becomes $[a_{k,n}]$, where $n = C_t + [y_{1k}]$. C_t is the center of the width of the column while $[y_{1k}]$ is a value of each element of the vector. The new matrix can be denoted as follows:

$$A_{(m_0,n_0)} = A_{(4,1024)} = \begin{pmatrix} a_{1,1} & a_{1,2} & \cdots & a_{1,1024} \\ a_{2,1} & a_{2,2} & \cdots & a_{2,1024} \\ \vdots & \vdots & \ddots & \vdots \\ a_{4,1} & a_{4,2} & \cdots & a_{4,1024} \end{pmatrix} \tag{4.4.1}$$

The starting point of the matrix is located in the first row and in the center of the length of column ($C_t = n/2$) of the matrix. So, the coordinate of (0,0) is (a_{1,C_t}) in this matrix. The number of columns of the matrix (n_0) is 1024, then C_t will be 512, as a result, the coordinate of (0,0) is $(a_{1,512})$.

In this proposed strategy, the value of the signal is converted to **1** as a *white color* in the image matrix while **0** represents a *black* one using this condition:

$$A_{0(m_0,n_0)} = \begin{cases} 1 & \text{for} \quad n = C_t + y_{1k} \\ \\ 0 & \text{for} \quad else \end{cases} \tag{4.4.2}$$

where:

y_{1k} = value of the vector after the rounding process

$C_t = n/2 = 512$, center column of the matrix

So each element of matrix can be written as:

$$a_{k,n} = a_{k,C_t+(y_{1k})} = 1 \tag{4.4.3}$$

For example, lets say y =[-3.1 -1.2 0 4.0], and then by the integer rounding process it becomes y_r= [-3 -1 0 4]. With the number of columns of the matrix = 9, C_t= 5, then the first element of data sets the element of the matrix:$a_{1,5(-3)} = a_{1,2}$= 1. The same process applies for the other values of y_r, so all element of matrix that are converted to 1 are: $a_{1,2};\ a_{2,4};\ a_{3,5};\ a_{4,9}$, and all the other elements of the matrix are converted to 0. The resulting matrix:

$$A_{m,n} = \begin{pmatrix} 0 & 1 & 0 & 0 & 0 & 0 & 0 & 0 & 0 \\ 0 & 0 & 0 & 1 & 0 & 0 & 0 & 0 & 0 \\ 0 & 0 & 0 & 0 & 1 & 0 & 0 & 0 & 0 \\ 0 & 0 & 0 & 0 & 0 & 0 & 0 & 0 & 1 \end{pmatrix} \tag{4.4.4}$$

The number of samples for every loop is 4. For the signal $f(x)$ = [1 2 3 4 5 6 7 8 9 10], the first sample is [1 2 3 4], the second samples is [4 5 6 7], and the last one is [7 8 9 10]. So, samples that are used for the looping process s_j from n_i to $\{n_i + 3\}$ can be denoted as follows:

$$s_j = n_i \cdots (n_i + 3) \tag{4.4.5}$$

where $i = 3_j - 2$, and $j = 1, 2, ..., (\frac{l}{3} - 3)$ where l is the total number of samples in the signal.

Adding Connectivity Points

Matrix A_0 which is the result of the previous step should be modified to make the points connected with each other. Therefore points need to be added to the matrix as follows:

$$A_{1(m_0,n_0)} = 1 \quad \text{from} \quad m_0 = C_t \quad \text{to} \quad m_0 = C_t + y_{1n} \tag{4.4.6}$$

Boundary Extraction

The same step as the SIC, the boundary extraction, $\beta(A_1)$ is applied on the matrix which is the result of the adding connectivity points process, and it can be denoted as:

$$\beta(A_1) = A_1 - (A_1 \ominus SE) \tag{4.4.7}$$

Using this method, where the SE is a flat structuring element, matrix A_1 is transformed into matrix A_2.

Points deletion

After boundary extraction, matrix A_2 still has some points in the center of the matrix that are not representing the values of the signal. To eliminate them, the following formula can be applied with N = 1,2,3,4:

$$A_{2(N,C_t)} = 0 \tag{4.4.8}$$

Double dilation and double erosion

By deleting axis points, some points that are the representation of the value of the signal will be lost. In order to fix this problem, dilation is applied twice and then followed by the application of erosion twice which could be denoted using this equation:

$$A_3 = ((((A_2 \oplus \text{SE}) \oplus \text{SE}) \ominus \text{SE}) \ominus \text{SE}) \tag{4.4.9}$$

Equation 4.4.10 shows an example of the final result (A_3) of the matrix $A_{m,n}$ with 9 columns. From the first matrix $A_{m,n}$, there are no additional points between each other, but it has a gap between 1 in some elements of the matrix. After the proposed process has been applied to the first matrix, there are some additional connected points in the final matrix. The number of additional points for every row depends on the gaps in the matrix.

$$A_3 = \begin{pmatrix} 0 & 1 & 1 & 0 & 0 & 0 & 0 & 0 & 0 \\ 0 & 0 & 0 & 1 & 0 & 0 & 0 & 0 & 0 \\ 0 & 0 & 0 & 0 & 1 & 0 & 0 & 0 & 0 \\ 0 & 0 & 0 & 0 & 0 & 1 & 1 & 1 & 1 \end{pmatrix} \tag{4.4.10}$$

4.5 Detecting the Time Location of Disturbances Using SIMC-SDW

In order to detect the location of the disturbances, the mean value ($\bar{x}$) of each row should be found. In this strategy, the mean value of the signal is calculated using the following formula:

$$\bar{x} = \frac{\sum_{i=1}^{n} x_i}{n} \tag{4.5.1}$$

where x_i is a value of each component of the matrix, and n is the number of columns of the matrix.

The first matrix has one point for every value of the signal that has been converted to a value of 1. The flow of the signal has been changed as a matrix which goes from top to bottom, so the mean of every row of the matrix can be calculated. When a disturbance occurs, a sudden change of waveform will occur in the signal. By transforming the matrix, a different gap from another row will be identified. Additional points are added for these gaps, and as a result, the mean of that row becomes higher than the other points. By comparing the mean value of this matrix ($\bar{x}_m$) to the mean value of the normal signal ($\bar{x}_0$), the time location (T_L) of the disturbances can be detected.

$$\mathrm{T}_L = \bar{x}_m > \bar{x}_0 \tag{4.5.2}$$

For a noise-free signal, the mean value is 0.0107 for every row of the matrix. This value was found by processing the normal signal and then calculating the mean value of this signal. From this process, the maximum number of the matrix that has the value of 1 are 11. So by dividing 11 to 1024 is equal to 0.0107. When the signal is contaminated with noise with a SNR at 30dB, the mean value is higher. After some experiments to determine the optimum filtering process, the mean value of this signal in the matrix is 0.03024. So, the location of the disturbance can be detected when $\bar{x}_m > 0.03024$ for the signal with a SNR at more than 30dB. This $\bar{x}_m$ value is only effective for the range of SNR between 30

-100dB. For a signal that has SNR value at lower than 30dB, this method will produce an error in the detection process.

4.6 Simulations and Results for SIMC-SDW Method

4.6.1 Simulations of SIMC-SDW

Simulations of this proposed strategy were undertaken using Matlab. The input signals contained 3 types of disturbances: voltage sags, swell, and voltage interruption and are shown in Figure 4.20. The first condition of the simulation is for signals without noise, and then continued for the signals contain noise by adding Additive White-Gaussian Noise (AWGN) with a SNR (Signal to Noise Ratio) at 30 dB. The value of C_t is set to 512, so n_0 becomes 1024, with a sampling frequency of 6.4 kHz, the size of the window is 1/32 cycle with 4 samples in every looping detection process.

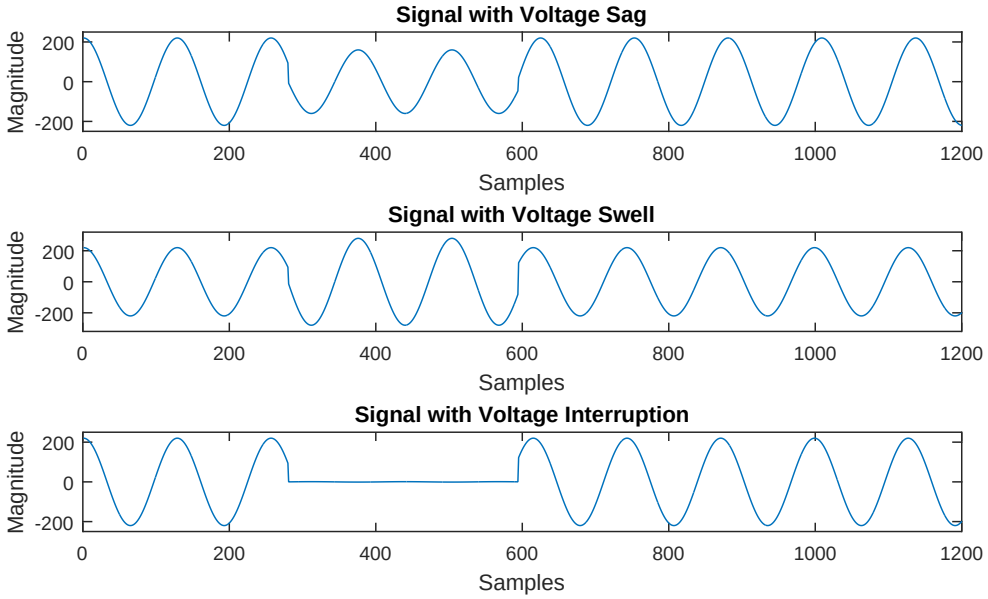

Figure 4.20: Signals with voltage sag, swell, and interruption

4.6.2 Results of SIMC-SDW

After applying the strategy proposed in this chapter the detected time location of the sag disturbances can be seen in Figure 4.21 and 4.22 both for noise free signal and for signal with 30 dB noise. Is it clearly seen in these figures that starting point and ending point of disturbances are successfully detected using this method. The same successful results have also been found in detection of swell and interruption in both conditions, noise-free and SNR at 30dB, as shown in Figure 4.23 to 4.26

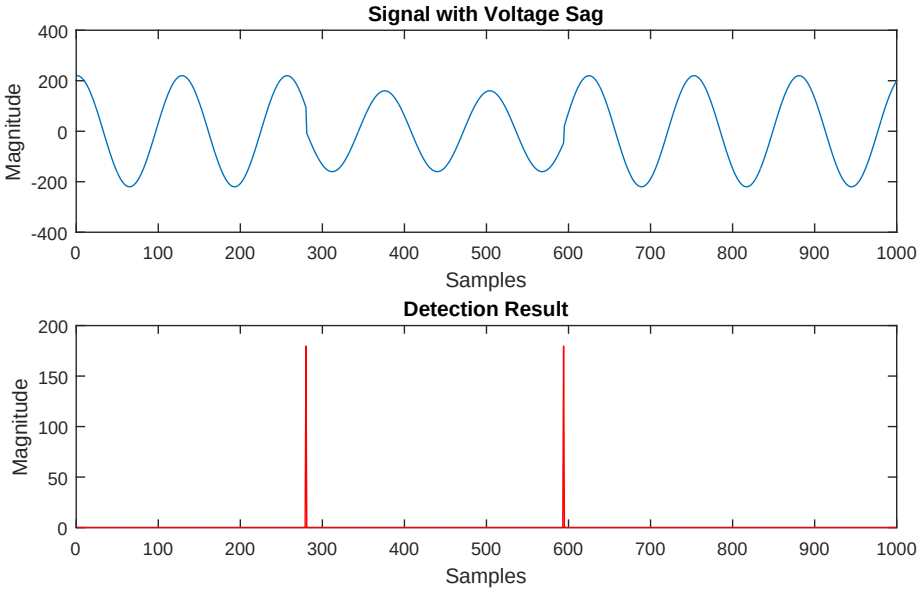

Figure 4.21: Detection results for sag in noise-free signal

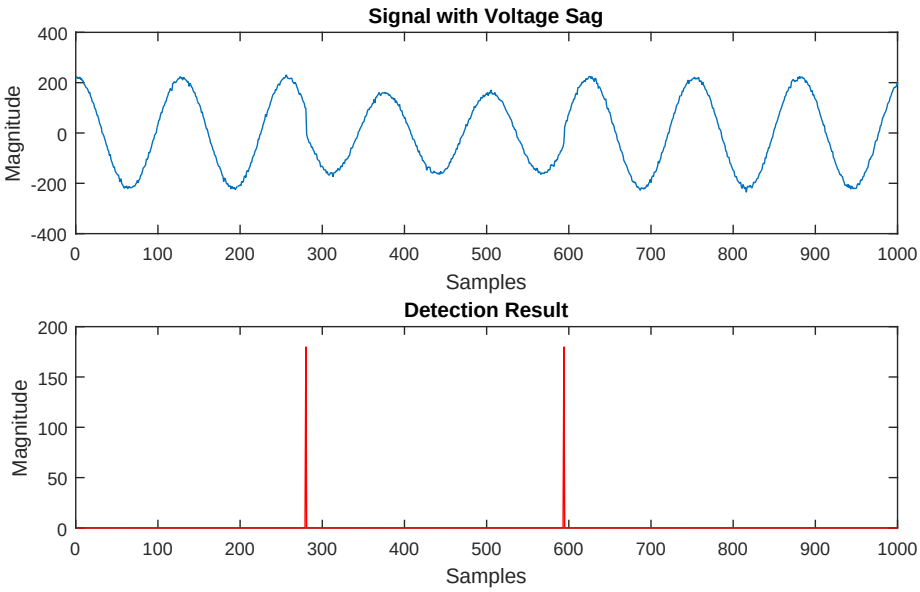

Figure 4.22: Detection results for sag in 30 dB noise signal

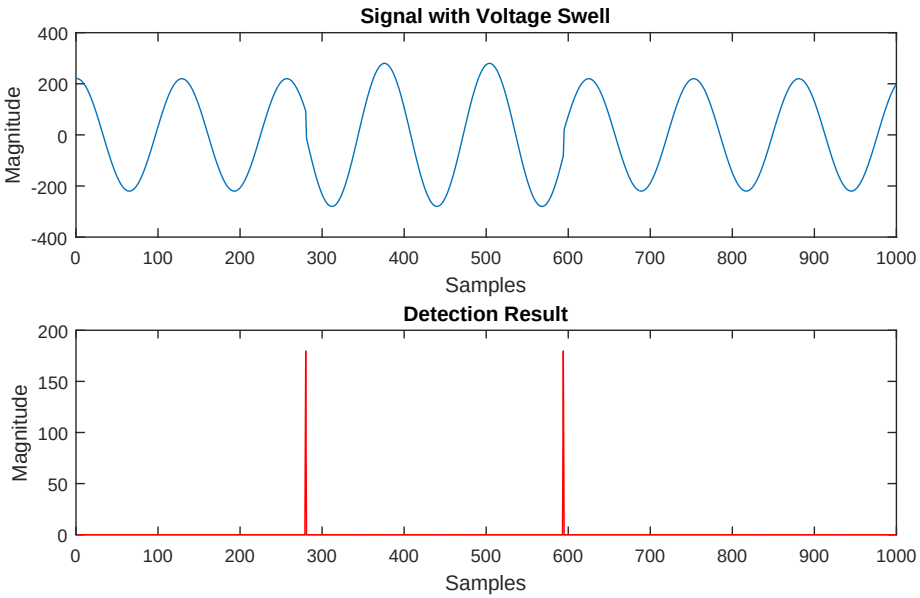

Figure 4.23: Detection results for swell in noise-free signal

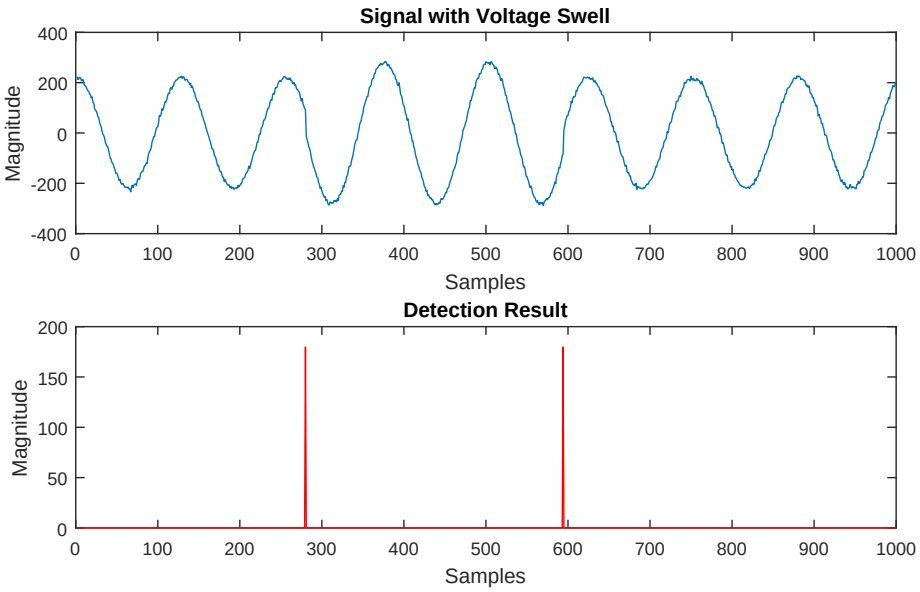

Figure 4.24: Detection results for swell in 30 dB noise signal

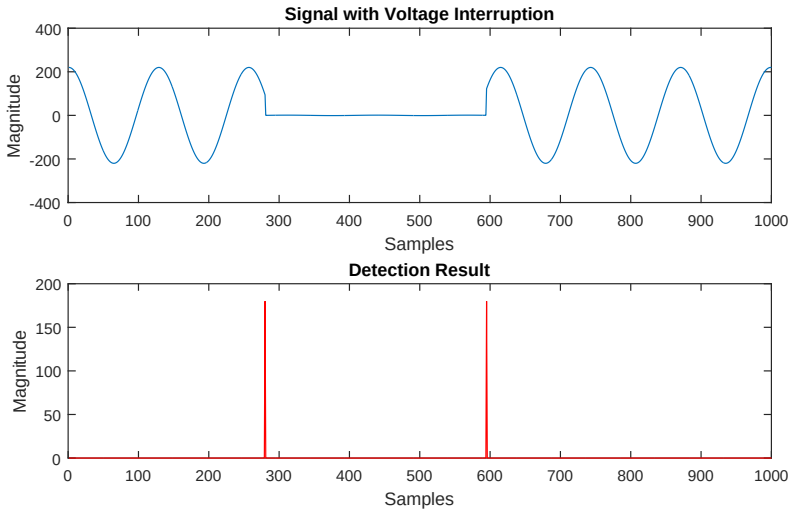

Figure 4.25: Detection results for interruption in noise-free signal

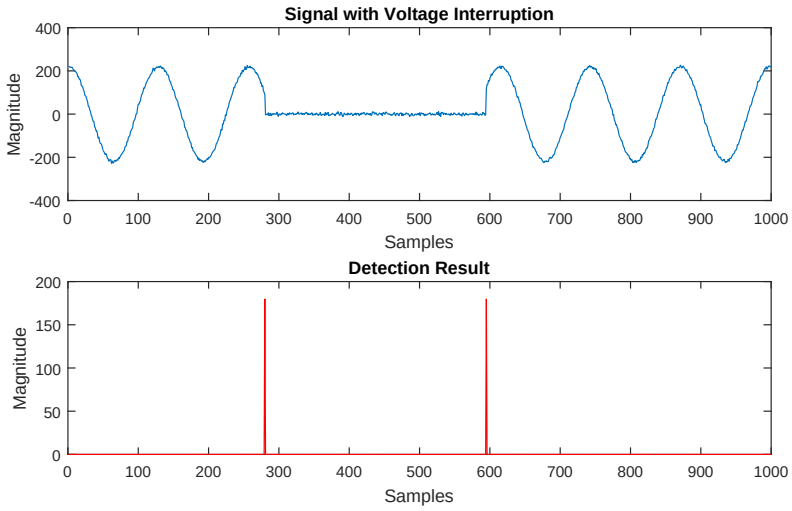

Figure 4.26: Detection results for interruption in 30 dB noise signal

Simulations also have been conducted for various SNR values, and each SNR value was analysed 100 times. The error results for these simulations are shown in Table 4.2. In this table, the proposed method is successful in detecting all three kind of disturbances with the maximum value of the SNR being 35dB. At 30dB, this method still can handle the sag and the interruption with only 14% and 3% error but with a high error (76%) for swell. This method cannot when SNR is lower than 25dB.

Table 4.2: Percentage of error in detecting disturbances using SIMC-SDW

No	**Disturbances**	**SNR**						
		40	**35**	**32**	**30**	**28**	**25**	**20**
1	Sag	0%	0%	1%	14%	58%	100%	100%
2	Swell	0%	0%	12%	76%	100%	100%	100%
3	Interruption	0%	0%	0%	3%	30%	99%	100%

This strategy was also tested in condition when the signal has the different SNR (from 0db - 100dB) for voltage sag, voltage swell and voltage interruption, as shown in Figure 4.27. From this graph, it is clearly seen that this strategy has a capability in handling a

signal with SNR above 30dB. Below this point (30dB) the error is increased exponentially when the value of SNR is decreased to zero.

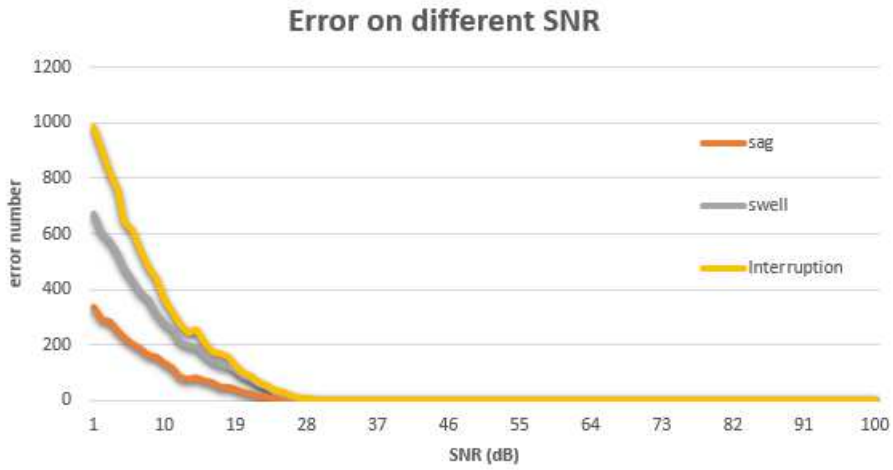

Figure 4.27: Error results in different SNR using SIMC-SDW method for sag, swell and interuption

As mentioned before the signal as a vector has been converted to an image matrix, so some kind of the structuring element that used in image processing can be used in this matrix. In this case, the diamond and disk structuring elements with different radius are applied to this strategy. Table 4.3 shows the detection results for all three types of disturbances using the different SE (b_1 and b_2).

For the different types and radiuses of the structuring elements in the filtering step, the results varied. The best result for disturbances detection can be found using a diamond structuring element with the size of radius (the distance from the structuring element origin to the points of the diamond) being 1. This proposed strategy successfully detects the start and end of the voltage sag and swell accurately for both noise-free signals and signals contaminated with noise. For the voltage interruption, the starting point of the disturbance can be detected accurately by this strategy, but not the end point. This is because the type and length of the structuring element deletes the important part of the signal to locate the end of this disturbance. This can be seen in Table 4.3, when the disk SE rather than the diamond SE

Table 4.3: Simulation results of SIMC-SDW method

PQ Events		**Voltge Sag**		**Voltage Swell**		**V. Interruption**	
		start	end	start	end	start	end
Actual Position		280	594	280	594	280	594
Results for different Structuring Element							
b_1= $\odot$, 1	n-f	280	594	280	594	280	x
b_2= $\odot$, 1	n-n	280	594	280	594	x	x
b_1= $\odot$, 1	n-f	280	594	280	594	280	-
b_2= $\odot$, 2	n-n	280	x	x	x	280	x
b_1= $\odot$, 2	n-f	280	594	280	594	280	-
b_2= $\odot$, 1	n-n	280	x	x	x	280	594
b_1= $\odot$, 2	n-f	280	-	280	594	280	594
b_2= $\odot$, 2	n-n	280	-	x	x	280	594
b_1= $\diamond$, 1	n-f	280	594	280	594	280	-
b_2= $\diamond$, 1	n-n	280	594	280	594	280	-
b_1= $\diamond$, 1	n-f	280	594	280	594	-	-
b_2= $\diamond$, 2	n-n	x	x	x	x	280	x
b_1= $\diamond$, 2	n-f	280	594	280	594	280	-
b_2= $\diamond$, 1	n-n	280	594	x	x	280	594
b_1= $\diamond$, 2	n-f	280	-	280	594	280	-
b_2= $\diamond$, 2	n-n	280	-	x	x	x	x

Note:

- = no result found.

x = some points are detected including actual points.

n-f = noise free signal, n-n = signal with 30dB noise

$\odot$ = disk, $\diamond$ = diamond

can detect this type of disturbance, although the disk SE does not generate the best results for overall performance.

The results of this strategy for detecting the time location of the disturbances compared with different methods can be seen in Table 4.4. This table shows that wavelet method has an error for detecting both the start and end points of the disturbances. Morphology edge detection [13] also has some errors in the detection of disturbances with an average error of half the sampling period. Skeletonization [71] finds the time location of the start of the disturbances more accurately. The only error is in finding the end point of the voltage interruption. The proposed method also has accurate results for sag and swell detection. For interruption detection, by using a diamond with radius 1 for both SEs in the filtering process, this method can detect the starting point of interruption but has an error of 1 sample while detecting the end point. This is because the variation of the signal after end point was small, making the detection result was not in accurate point but at one sample after the actual point. The Skeletonization method has the same result for detection, but it needs a bigger window size (1/2 cycle with 64 samples) while the proposed method just needs 1/32 cycle of a window size or 4 samples only.

Table 4.4: Comparison results with other methods in the time domain

Disturbances	**Sag**		**Swell**		**Interruption**	
	start	end	start	end	start	end
Actual Location	280	594	280	594	280	594
Detect. Result	280	594	280	594	280	595
Error for:						
Proposed Method	0	0	0	0	0	1
$Wavelet$	1	1	1	1	1	1
$Morph.Edge_{[13]}$	0.5	0.5	0	1	0	1
$Skeletonization_{[71]}$	0	0	0	0	0	1

4.7 Summary

From the previous explanation, a conclusion can be made that the proposed strategy in detecting location time of power quality disturbances is based on the signal to image matrix conversion. By converting the signal into image, the detection process can use the methods developed from image processing. The conversion steps are points addition, morphology boundary, deleting axis points, and adding lost points.

Three types of disturbances, sag, swell and interruption has been simulated using the proposed method. In this simulation, the detection results show that the accurate location time of disturbances can be detected as violation points in control chart.

The SIMC-SDW strategy to detect the times of power quality disturbances uses small data samples of the signal (4 samples) and it makes the size of the window small (1/32 cycle). In addition, by using mathematical morphology, which has an excellent speed of calculation, this method can be implemented as a real time detection strategy.

The results of SIMC-SDW method show the ability of this strategy in detecting disturbances, especially for swell and sag. For the voltage interruption, the starting point can be found accurately while the end point cannot be determined at the exact location but has an error at 1 sample. For this purpose, it is essential to choose the parameter value and type of structuring element accurately based on the type of disturbance. This strategy has an improvement compared to the wavelet method or Morphology edge detection strategy.

Chapter 5

Disturbances Detection Using Half Multi-resolution Morphology Gradient

5.1 Introduction

In this chapter, a new strategy in disturbance detection is presented using Half Multi-resolution Morphology Gradient (HMMG). This strategy is based on Multi-resolution Morphology Gradient (MMG) that has the capability to detect ascending and descending edges of the waveform. This is different to MMG, as this proposed strategy uses only half the processes of MMG, and also is only applied at level 1. By doing this, the time of the computational process can be reduced.

5.1.1 Morphology Gradient

Morphology gradient (MG) is widely used for edge detection in image and signal processing. There are two types of residual in MG. The first ones is the dilation residual, G_d, which is the difference between the dilation of the input signal f by structuring element g

and f, and can be denoted as:

$$G_d(f) = (f \oplus g) - f \tag{5.1.1}$$

The second one is the erosion residual, G_d, as a difference between f and the erosion of f and g, and can be denoted as:

$$G_e(f) = f - (f \ominus g) \tag{5.1.2}$$

the MG is defined as:

$$G(f) = (f \oplus g) - (f \ominus g) = G_d(f) + G_e(f) \tag{5.1.3}$$

5.1.2 Multi-resolution Morphological Gradient

Another development on MG was a multi-resolution morphological gradient (MMG). MMG has the capability in extracting a travelling waveform by depressing the steady state components and enhancing the transient ones. This method can detect not only the location of waveform changes but also their polarities [72]. The design of this strategy is using a scalable flat line structuring element, with different origins, and it can be written as a mathematical expression as follows:

$$g^+ = \{g_1, g_2, ..., g_{l-1}, \underline{g_l}\} \tag{5.1.4}$$

$$g^- = \{\underline{g_1}, g_2, ..., g_{l-1}, g_l\} \tag{5.1.5}$$

where:

- g^+ = the SE used for extracting the ascending edges
- g^- = the SE used for extracting the descending edges
- $l = 2^{1-a} l_g$,
- a = the level of MMG to be processed

- l_g = the primary length of g at level 1

The dyadic MMG with level a, ρ_g^a is defined as:

$$\rho_{g^+}^a = \delta_{g^+}(\rho^{a-1}) - \varepsilon_{g^+}(\rho^{a-1}) \tag{5.1.6}$$

$$\rho_{g^-}^a = \varepsilon_{g^-}(\rho^{a-1}) - \delta_{g^-}(\rho^{a-1}) \tag{5.1.7}$$

$$\rho_g^a = \rho_{g^+}^a + \rho_{g^-}^a \tag{5.1.8}$$

A MMG will represent the input signal if a=1. This is because $\rho_g^0 = S$ or the input signal.

The detection of the ascending and descending edges of the waveform can be seen in this formula:
Since $\delta_g(\rho^{a-1}) \subset \varepsilon_g(\rho^{a-1}) : g \neq \emptyset$, then $\rho_{g^+}^a > 0$ and $\rho_{g^-}^a < 0$

The result of the MMG input signal (f) and the structuring element g = 3 can be seen in Figure 5.1.

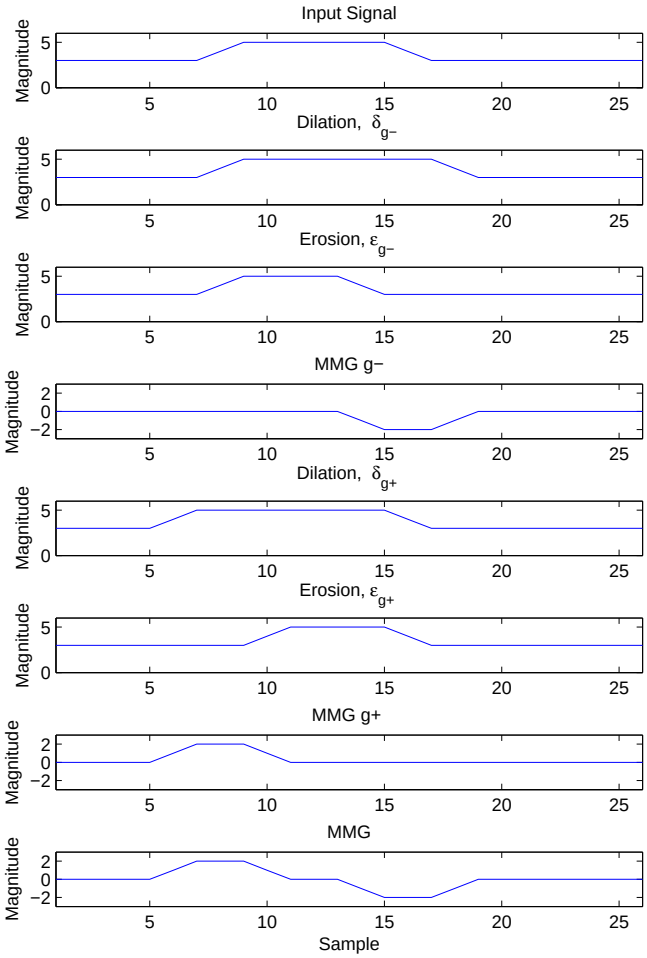

Figure 5.1: Results of the MMG for $g = 3$ and $a = 1$

5.1.3 Proposed Method

In this section, a Half Multi-resolution Morphological Gradient (HMMG) is proposed for the detection of disturbances. HMMG is based on the Multi-resolution Morphological Gradient Algorithm (MMGA) [44], where only half the calculations of MMGA are processed. The *HMMG* at level a, ρ_g^a can be denoted as the difference between the original signal, $f(x)$, and the dilated signal:

$$\rho^{a}_{g^-} = f(x) - (\rho^{a-1} \oplus g^-)(x) \tag{5.1.9}$$

and as difference between the original signal and the eroded signal:

$$\rho^{a}_{g^+} = f(x) - (\rho^{a-1} \ominus g^+)(x) \tag{5.1.10}$$

So, the HMMG can be defined as follows:

$$\rho_h = \rho^{a}_{g^+} + \rho^{a}_{g^-} \tag{5.1.11}$$

Unlike the MMG strategy, whose result can be obtained at $a = 2$ [73], in this method, the process can be done in level 1 only, or $a = 1$. Using this method, the location of waveform changes and their polarities can be detected. For the same input signal $f(x)$, the result of this proposed signal can be seen in Figure 5.2.

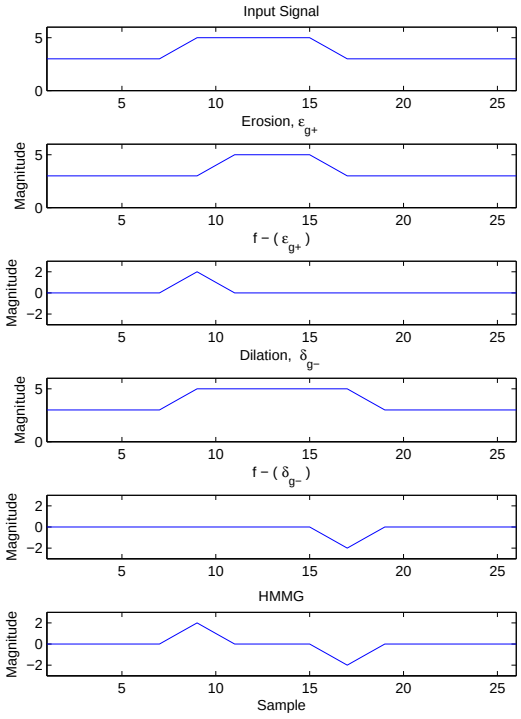

Figure 5.2: Results of HMMG for $g = 3$ and $a = 1$

In order to get the result of the location of disturbances, a threshold is used for the processed signal to clean some unwanted value of the signals. The threshold (θ) can be denoted as follows:

$$\theta = \varrho(g-1)V_{max} \tag{5.1.12}$$

and

$$\varrho_{100} = 303.2(f_s)^{-0.996} \tag{5.1.13}$$

$$\varrho_{30} = 305(f_s)^{-0.997} \tag{5.1.14}$$

where: ϱ_{100} is a constant of equation for SNR = 100. ϱ_{30} is a constant of equation for SNR = 30. V_{max} is the maximum voltage value of the signal in per unit or volt. f_s is the sampling frequency.

5.1.4 Classification of Disturbances

In order to classify the detected disturbances in the signal, the magnitude of the signal will be calculated using the root mean square value (rms) as follows:

$$V_{rms} = \sqrt{\frac{1}{N}\sum_{n=0}^{N-1} V^2(n)} \tag{5.1.15}$$

where:

$V(n)$ = the instantaneous value of the voltage in the n-th sample interval

N = number of sampling cycles over an integral multiple of the period of the input signal.

The type of disturbances analysed in this thesis are shown in Table 5.1. The classification of the disturbances is undertaken using parameters from this table in term of the extracted features of the signal. The signal during the disturbances is investigated by calculating the rms value and their period.

Table 5.1: Power disturbance classifications

Category	Spectral content	Typical duration	Magnitude
Transient	up to 5 MHz	ns - ms	0 - 8 pu
Notching		steady state	
Flicker	<25 Hz	steady state	0.9 - 1.1 pu
Sag		0.5 cycle - 1 min	0.1 - 0.9 pu
Swell		0.5 cycle - 1 min	1.1 - 1.8 pu
Interruption		>0.5 cycle	<0.1 pu

5.2 Simulations and Results

5.2.1 Oscillatory Transient and Notching

The simulation of this proposed strategy was undertaken using Matlab to analyse the input signal with added disturbances, i.e.; oscillatory transient, notching, sag, swell, interruption, and flicker. The sampling frequency for all simulations was 6.4 kHz on 50Hz ac signals.

The results of the HMMG method for transient and notching disturbances can be seen in Figure 5.3 and 5.4 respectively.

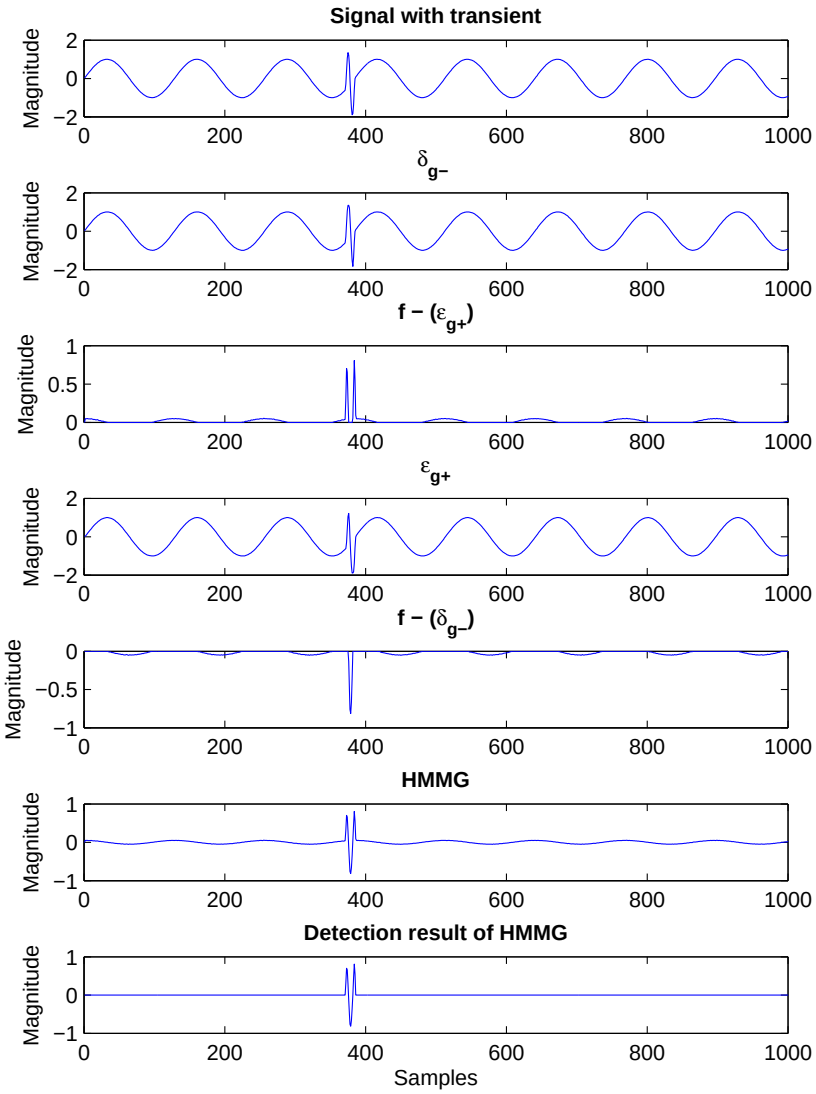

Figure 5.3: Detection result for an oscillatory transient

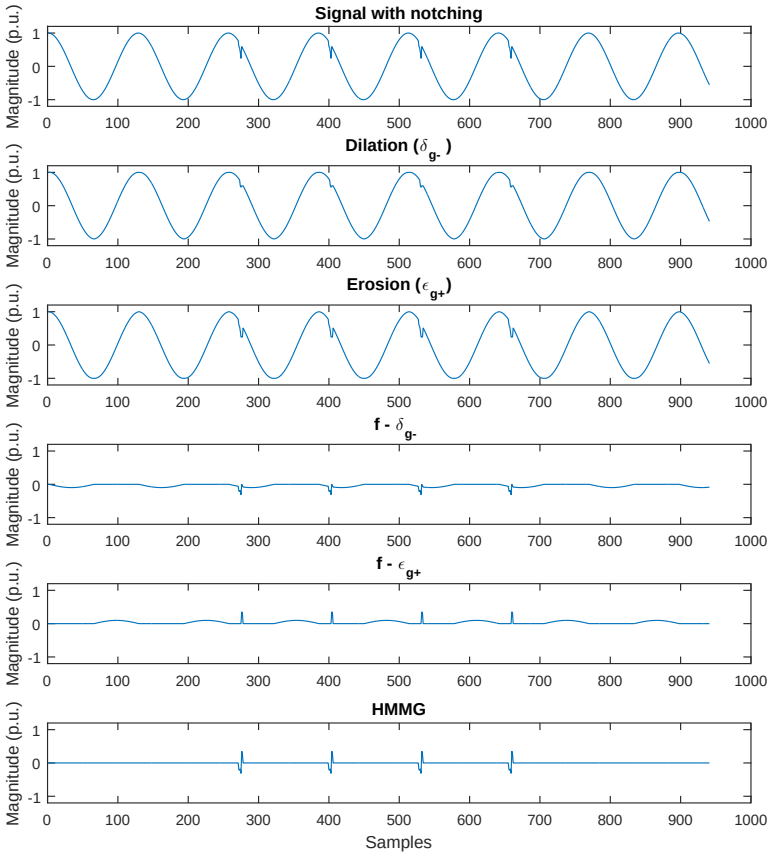

Figure 5.4: Detection result for notching

For the oscillatory transient and notching, the proposed method not only detects the disturbances in the signal, but also the polarity of the signal.

5.2.2 Sag, Swell and Interruption

Figures 5.5 and 5.6 show a comparison of the detection of sag and swell disturbances results using the MMG and the HMMG strategies. For the voltage interruption, the result of both detection methods can be seen in Figure 5.7.

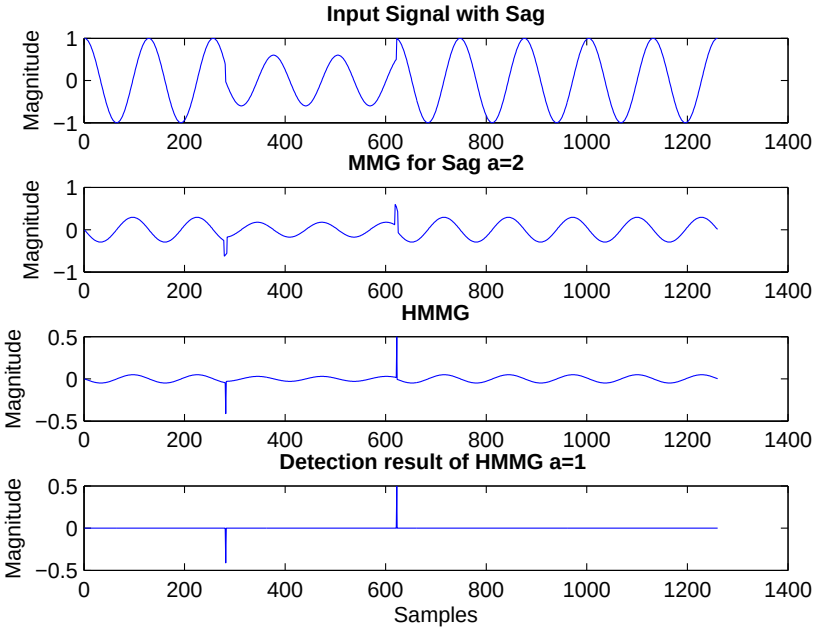

Figure 5.5: MMG and HMMG results for sag

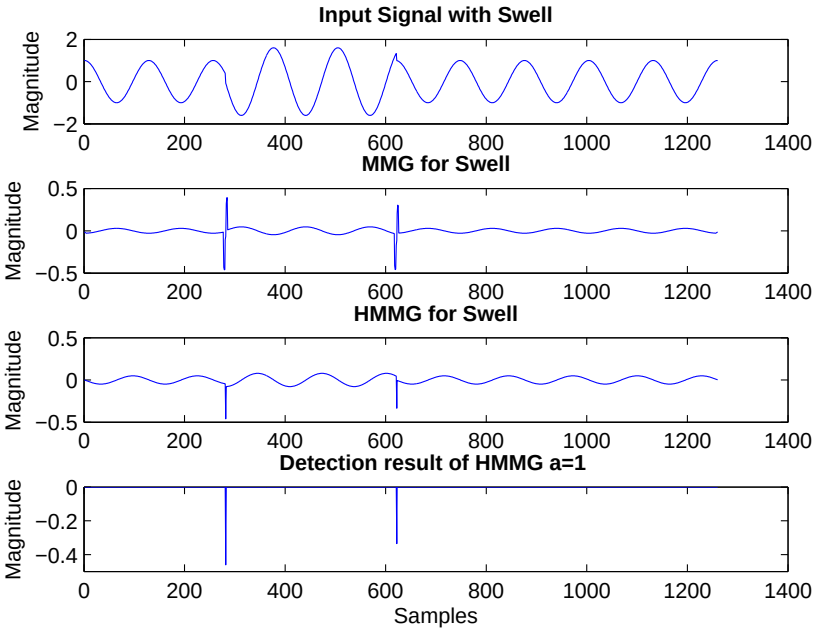

Figure 5.6: MMG and HMMG results for swell

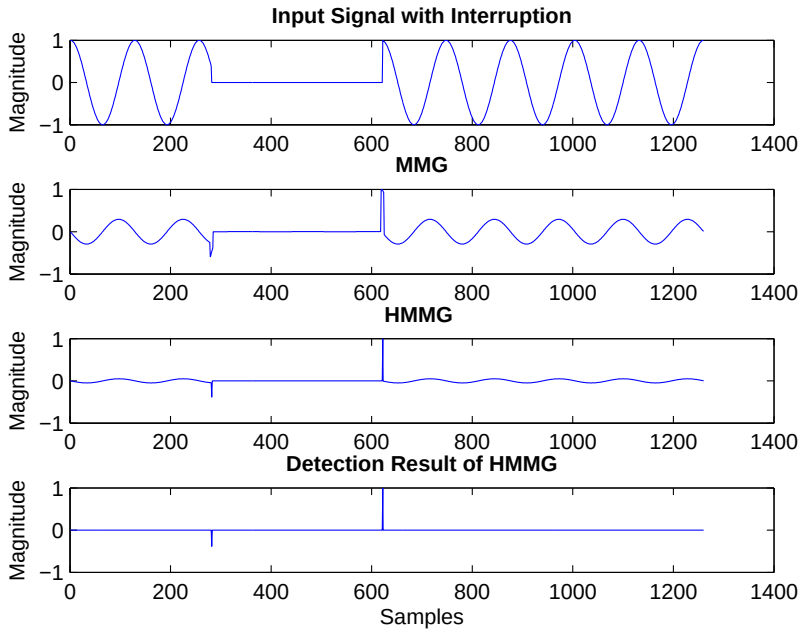

Figure 5.7: MMG and HMMG results for voltage interruption

The accuracy of the proposed method compared to the MMG method for sag, swell and voltage interruption can be seen in Table 5.2.

Table 5.2: Comparison of the MMG and HMMG methods

Method	**Accuracy in %**					
	Sag		Swell		Interruption	
	Start	**End**	**Start**	**End**	**Start**	**End**
MMG	98.43	96.09	96.88	96.09	95.31	98.43
HMMG	99.22	100	100	100	100	100

From Table 5.2 it can be seen that the HMMG strategy has the capability to detect sag, swell and voltage interruption more accurately than MMG. For swell and interruption, this method has 100% accuracy at both the beginning and end of the disturbances while there is only a small error in detecting the starting point of the sag disturbance.

5.2.3 Flicker

This method was also simulated on signal with flicker with SNR = 50, in order to analyse the performance of the proposed strategy. The result of flicker detection can be seen in Figure 5.8.

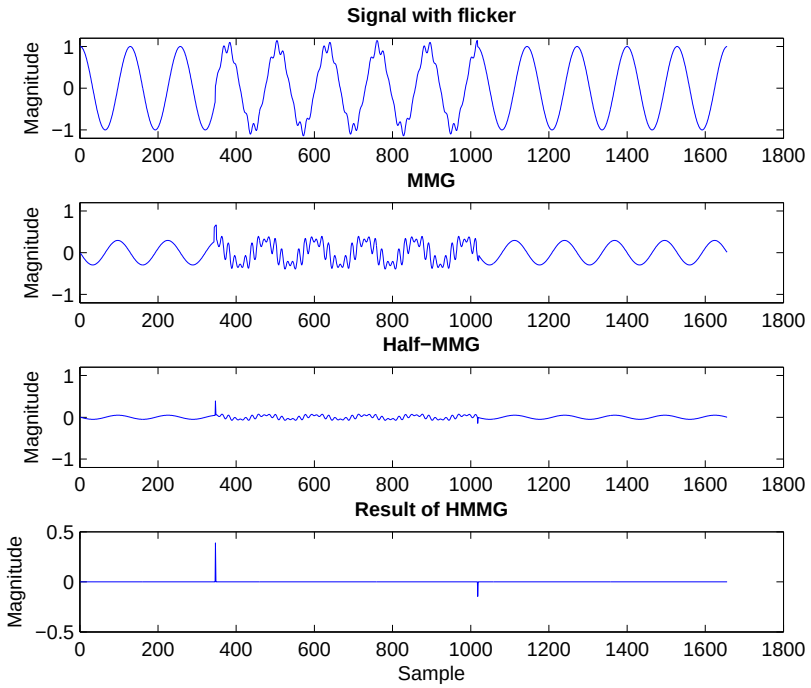

Figure 5.8: MMG and HMMG results for flicker

In these results, flicker can be detected in the signal more accurately using HMMG compared to MMG at g = 3 and a = 1.

5.2.4 Classification Results

To classify the disturbances, the properties of the features extracted by the HMMG are used especially the number of crest and trough signals and also the RMS value of the signal during the disturbances. Their time and frequency can be seen in Table 5.3.

From Table 5.3, the transient disturbance can be detected by its magnitude at 0.9836

Table 5.3: Features extracted for the classification of disturbances using HMMG

	Time	Frequency	RMS (p.u)	Crest	Trough
Transient	2.0 ms	500 Hz	0.9836	2	1
Notching	2.0 ms	-	-	1	2
Flicker	104.8 ms	-	0.9962	-	-
Sag	49 ms	50 Hz	0.504	1	1
Swell	49 ms	50 Hz	1.80	1	1
Interruption	49 ms	50 Hz	0.0001	1	1

p.u., and it has 2 crests and 1 trough. The frequency of this disturbance can be estimated using FFT at about 500Hz and it occurred for 2 ms. The detection of the notching has the same results as transient for its duration and its frequency but has a different number of its crests and troughs. The number of crests and troughs are 1 and 2 respectively.

Sag, swell, and interruption can be classified using their RMS value (*per unit*) based on Table 5.1 with the number of crests and troughs being only 1.

5.2.5 Calculation Speed Test

In order to know the processing time between the MMG and the HMMG, the calculation speed test has been undertaken using Matlab. A personal computer was used for this simulation with specifications as follows:

- System Model: HP Compaq Elite 8300 SFF
- System Type: x64-based PC
- Processor: Intel(R) Core(TM) i3-3220 CPU @3.30GHz, 2 Core(s), 4 Logical Processing(s)
- Installed Physical Memory (RAM): 8 GB

- Total Virtual Memory: 15.8 GB
- Microsoft Windows 7 Enterprise
- Matlab R2015a

Input data are signals with sag, swell and interruption. These signals were generated following IEEE Std 1159-2009. The sampling frequency is 6.4kHz with frequency system at 50Hz. The number of sample is 1280 or 10 cycles, so the duration of the samples is 500ms. The simulation was done in 100 repetitions then finding the average result of the calculations. The result of the calculation of processing time for both MMG and HMMG at level 1 and 2 can be seen in Table 5.4.

Table 5.4: Processing time result between MMG and HMMG at level 1 and 2

Type of Disturbances	**MMG**		**HMMG**	
	Level 1	**Level 2**	**Level 1**	**Level 2**
Sag	15.50 ms	31.40 ms	9.90 ms	19.70 ms
Swell	16.40 ms	32.60 ms	10.30 ms	20.80 ms
Interruption	15.40 ms	31.50 ms	9.90 ms	20.00 ms
Average	**15.77** ms	**31.83** ms	**10.03** ms	**20.17** ms

Table 5.4 shows that the HMMG is faster than the MMG in both level for processing all of three signal with disturbances. In average, the MMG has a slower processing time at about 1.5 time of the HMMG.

For the different sampling frequency (1kHz to 20kHz), the processing time of the MMG and the HMMG can be seen in Figures 5.9 where the HMMG is faster than the MMG. The higher frequency sampling, the faster the HMMG compared to the MMG.

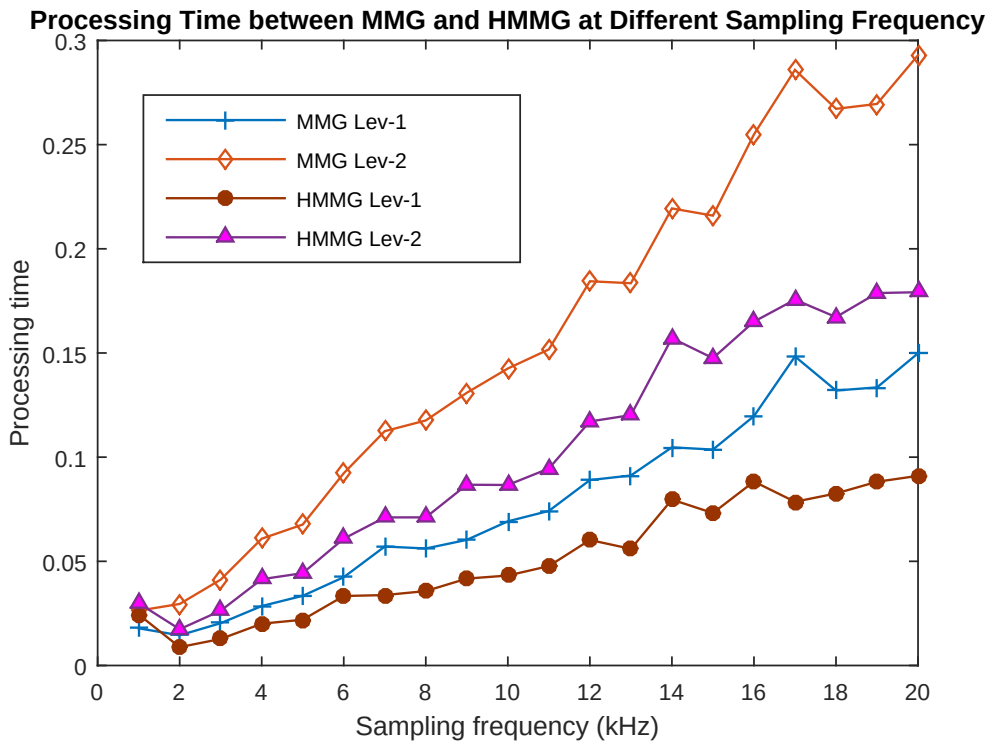

Figure 5.9: Processing time between MMG and HMMG at different sampling frequency

5.3 Summary

The proposed strategy in detecting the times of power quality disturbances using HMMG is based on MMG. Only half the processes of MMG are used for this strategy. Furthermore, the level of a is set at 1, so the processing time of the strategy is reduced.

Simulations for this method have been undertaken using Matlab. The results show some improvement in the detection of disturbances in the system compared to MMG. Like the MMG method, the HMMG approach has the capability to detect the polarity of the disturbances. The classification strategy for all disturbances was undertaken calculating the RMS value of the signal during the disturbances especially for sag, swell and momentary interruption. Transients, notching and flicker can be classified by using an FFT to find the number

of crests and troughs, and also their frequencies.

For real data simulations, there is some noise in the results of this strategy for sag, swell and interruption. In order to clean this noise, an appropriate filter needs to be applied to the input signal. This is because the input signals are not noise-free signals.

Chapter 6

Frequency Estimation Using Top-Hat and Bottom-Hat Transform

6.1 Frequency Estimation

In order to detect and analyse power quality disturbances, conventional strategies based on Fourier transforms have been applied. In this chapter, a new strategy in estimating the frequency of the signal in time domain is presented. This proposed strategy is based on top-hat and bottom-hat transforms. The signal is processed using both transforms, then the results are compared to find the frequency estimation of the signal. By simulating this strategy using Matlab, the results show good estimation for noise-free signal and signal with SNR at higher than 30dB. The accuracy of the results decreases when analysing the signal with SNR less than 30dB.

One of applications of frequency estimator is in a Phasor Measurement Unit (PMU). This frequency Estimation is a key role in the PMU's architecture as a frequency tracking and as a frequency compensation. It includes:

- Changing the sampling window
- Providing the frequency for phasor correction

Several methods for frequency estimation have been applied on the signal such as Zero Crossing method [74, 75]. This method has good performance for well filtered or perfect waves. It also has a high sensitivity to noise. Prony algorithm [76–79] also has a good performance in estimating the frequency in a signal. This proposed which gives reliable estimates in presence of noise but has a problem in the existent of the outliers due to the process on minimising the error between the estimated signal and original signal.

Another method for estimating frequency is Kalman filter [80]. This method is suitable for noise rejection, but it has a drawback where the process is slower compared with other methods. This method is dependent on the model parameters adjustment (variance and covariance noise matrices).

Demodulation is also can be used to estimate the frequency [75]. The main idea for this method is to multiply the scalar input with a sine and cosine signal with a know frequency. This has a sensitivity to large negative sequence component especially for fault conditions.

Phasor measurement angle changing [81] is also able to estimate the frequency signal. This method uses a positive sequence phasor estimation. This method presents satisfactory results under large frequency variations and is used in commercial PMUs.

In this chapter, the new strategy in estimating the frequency of a sinusoidal signal is presented. Even though for frequency estimation, the phasor angle changing method and demodulation strategy generated satisfactory results, but this strategy gives an alternative for the future application. This is because this method is based on mathematical morphology, the method that just needs some simple calculation.

6.2 Proposed Method

The strategy in estimating of the frequency of the signal is based on top-hat and bottom-hat transforms. The input signal $f(x)$ is initially processed using top-hat and bottom-hat SEs with value of structuring element (g) = 3 that can be denoted as follows:

Top-Hat Transform

$$T_{\mathrm{HAT}} = f - (f \circ g) \tag{6.2.1}$$

Bottom-Hat Transform

$$B_{\mathrm{HAT}} = f - (f \bullet g) \tag{6.2.2}$$

The effect of top-hat and bottom-hat transforms on the signal can be seen in Figure 6.1. A small magnitude represent the peak of the signal in positive value is generated when the signal is processed using the top-hat transform while a negative values is generated by using the bottom-hat transform.

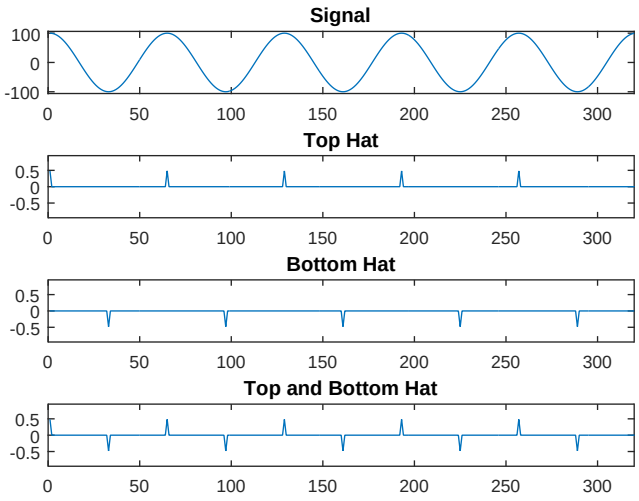

Figure 6.1: Effect of top-hat and bottom-hat on the signal

Frequency Calculation

Results of top-hat and bottom-hat transforms in a signal is used to estimate the frequency of the signal by calculating the location time between the peaks of the signal. The result of

the top-hat transform as a vector or matrix (1 x m) are then used to find the frequency estimation of the signal. From this matrix, the row number of the elements that contain zero value are deleted, and non-zero values is recorded as a new matrix $Tn_1(n)$ as follows:

$$Tn_1(n) = \begin{cases} n, & ; T_{\mathrm{HAT}}(n) > 0 \\ [-], & ; T_{\mathrm{HAT}}(n) = 0 \end{cases} \tag{6.2.3}$$

where n = 1, 2, 3,...,m and m is the length of the processed samples. Then every element of the matrix Tn_1 is subtracted to become a new matrix Tn_2 using this formula:

$$Tn_2(n-1) = Tn_1(n) - Tn_1(n-1) \tag{6.2.4}$$

The same process is used to generate the result of the bottom-hat transform. The new matrix $Bn_1(n)$ is denoted as follows:

$$Bn_1(n) = \begin{cases} n, & ; B_{\mathrm{HAT}}(n) < 0 \\ [-], & ; B_{\mathrm{HAT}}(n) = 0 \end{cases} \tag{6.2.5}$$

Then every element of the matrix Bn_1 is subtracted to become a new matrix Bn_2 using this formula:

$$Bn_2(n-1) = Bn_1(n) - Bn_1(n-1) \tag{6.2.6}$$

From these results, the frequency estimation (f_{es}) can be calculated using the following formula:

$$f_{es} = f_s/(Tn_2 \vee Bn_2); \tag{6.2.7}$$

where f_s is the sampling frequency and ($Tn_2 \vee Bn_2$) is the maximum value of either Tn_2 or Bn_2.

By choosing the maximum value between Tn_2 and Bn_2, the values from the top-hat and bottom-hat transforms process that represent the noise in the signal can be eliminated.

6.3 Simulations and Results

There were some simulations undertaken using Matlab. This proposed strategy was used to calculate the frequency of the signal in different conditions; noise free signals and signals containing noise. All signals were analysed in different frequencies and different values of SNR. The sampling frequency for all simulations was 6.4 kHz with a structuring element (g) = 3.

6.3.1 Noise-Free Signal

For the noise-free signal, the estimation process using the top-hat transform can be seen in Figure 6.2 to 6.4.

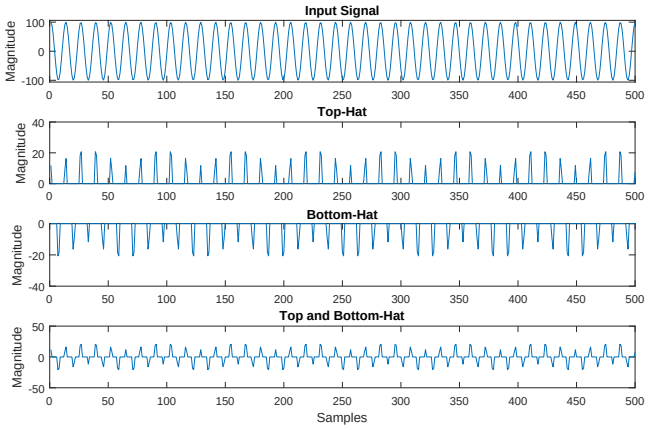

Figure 6.2: Results of top-hat and bottom-hat transform for a noise-free Signal

Figure 6.3 is the comparison of actual frequency and frequency estimation using the top-hat transform for noise-free signal. The errors in this method increase gradually following the increase of the frequency. This error can be seen in Figure 6.4. For frequencies 30 to 60 Hz, the error is less than 1% while at 300 Hz it becomes 5% and also at 500 Hz it is about 8%.

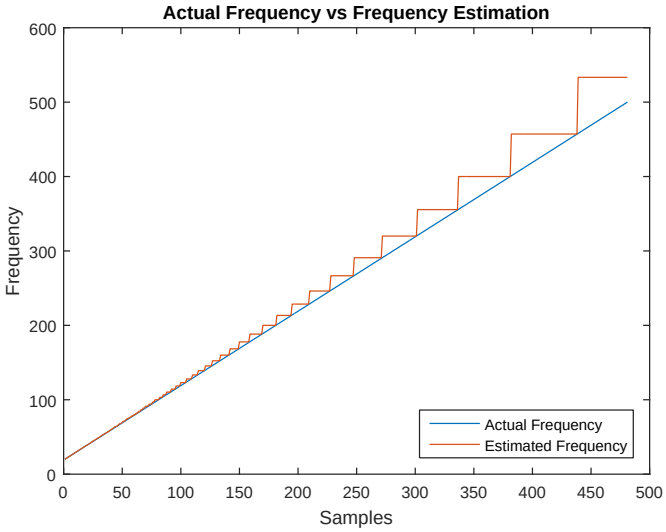

Figure 6.3: Actual frequency vs estimated frequency for noise-free signal

In Figure 6.3 the shape of the error is unique. It has a stair shape with some of the errors are zero or near zero with the largest error is just about 8% for a frequency of 495Hz. This means that some frequency are estimated correctly by this strategy especially for noise-free signals.

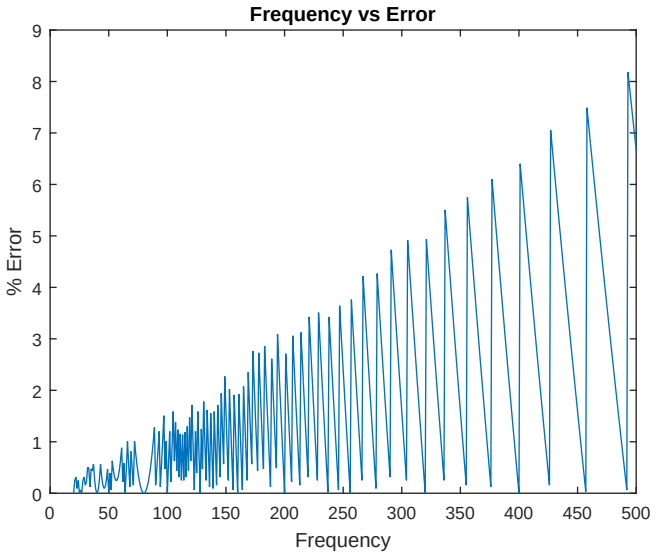

Figure 6.4: Frequency vs error for noise-free signal

6.3.2 Signal with Noise

The simulation has also been undertaken using different values of signal to noise ratio (SNR) to show the effect of noise on the signal. Figures 6.5 to 6.7 show the estimation process using top-hat transform for signal with SNR =30 and the frequency varying from 20Hz to 500Hz.

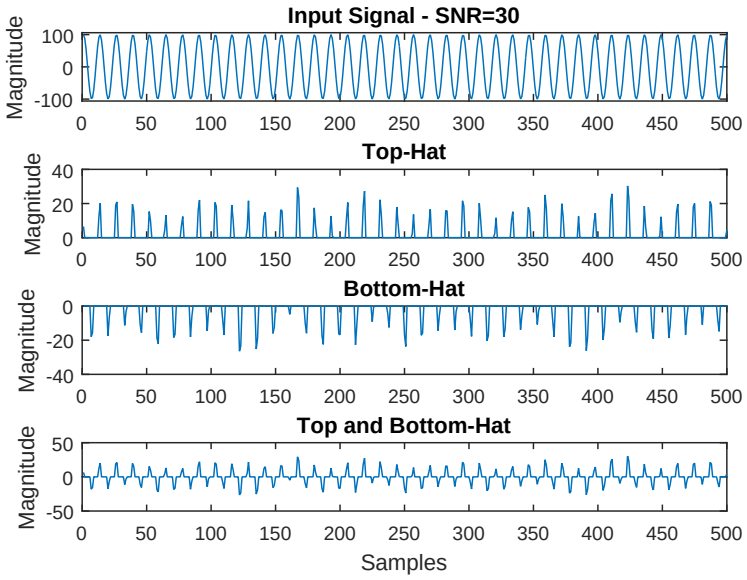

Figure 6.5: Results of top-hat and bottom-hat transform for SNR=30

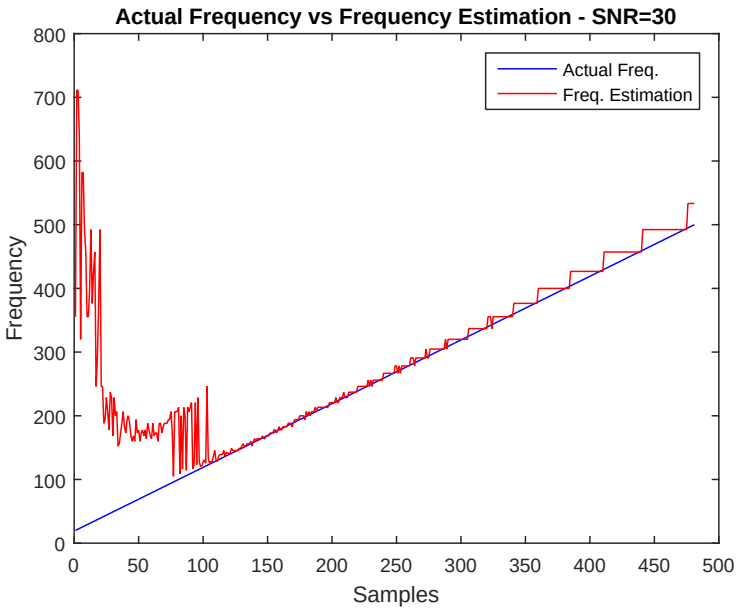

Figure 6.6: Actual vs estimated frequency for SNR=30

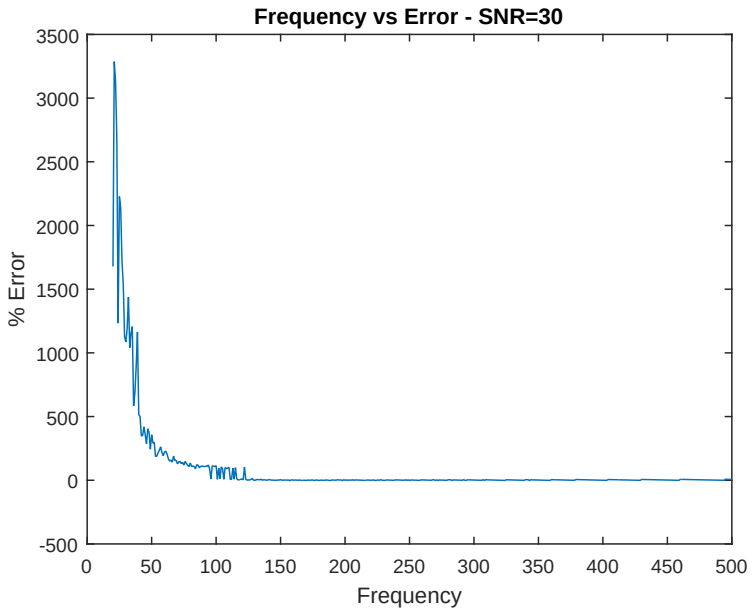

Figure 6.7: Frequency vs error for SNR=30

It is clearly seen in Figure 6.6 that this method has a difficulty in detecting frequency lower than 110Hz. In this frequency range, the errors are high while in the frequency over 110Hz this method generates a better results. The error in this condition can be seen in Figure 6.7 for the different frequency. The error for the frequency of lower than 100Hz happens due to the availability of noise in this signal. This noise is processed by the top-hat transforms making this strategy generate an imprecise estimation. The more noise exists in the signal, the higher the frequency estimation is produced. For example, the result for a signal with frequency of 40Hz is 400Hz or ten times higher than the expected frequency which is shown in Figure 6.7

Figure 6.8 shows the results of the top-hat and bottom-hat transform for a frequency of 100Hz. The actual frequency versus estimated frequency for varies SNR (from 0dB to 100dB) at frequency 100Hz can be seen in Figure 6.9. The error increased when the SNR was lower than 35 dB. This means that more noise makes more errors in this method as can be seen in Figure 6.10.

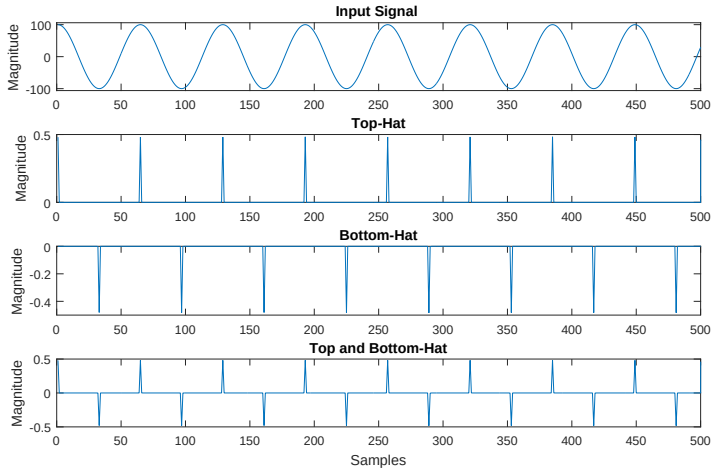

Figure 6.8: Results of top-hat and bottom-hat transforms at 100Hz

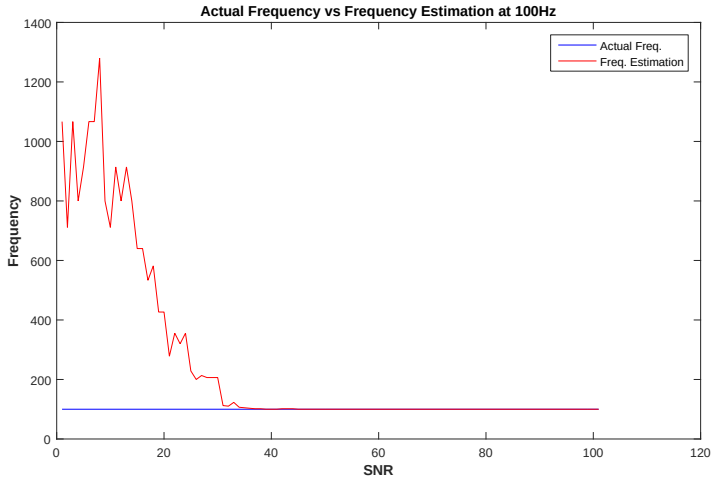

Figure 6.9: Actual vs estimated ftrequency for various SNR at freq. of 100Hz

For the signal with a frequency of 100Hz, the strategy has good results when the SNR value is larger that 35dB.

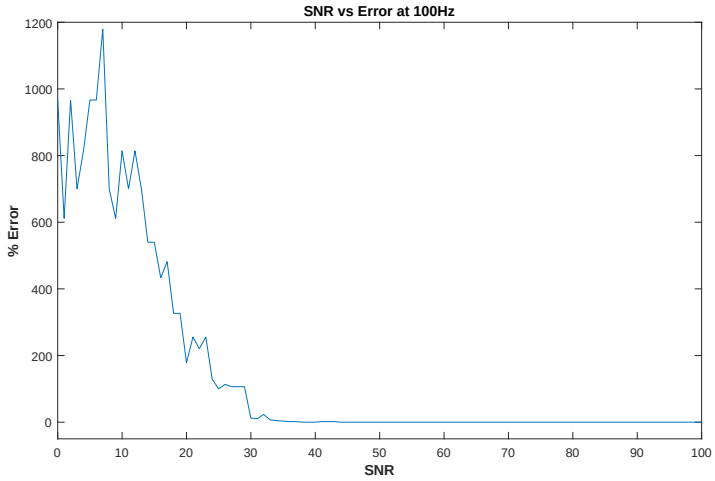

Figure 6.10: SNR vs error at freq. of 100Hz

This strategy successfully estimate the frequency of the signal at 300Hz when the signal has SNR value greater than 18dB. It can be seen in Figures 6.11 to 6.13.

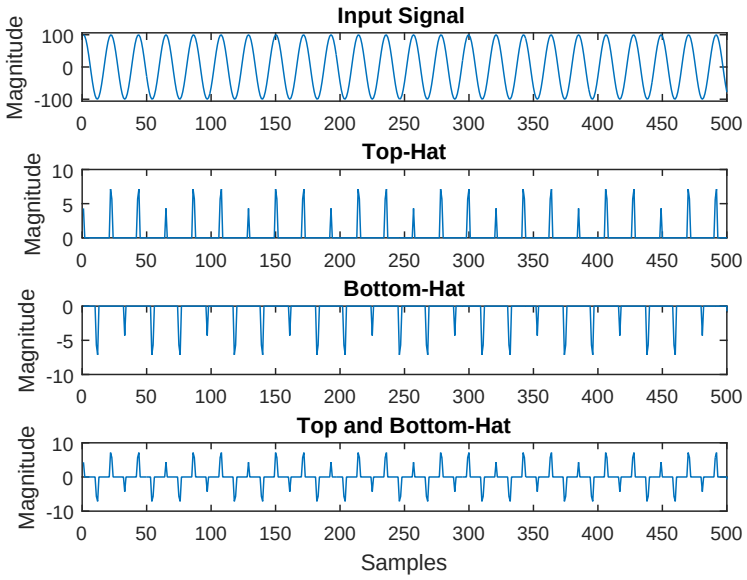

Figure 6.11: Results of top-hat and bottom-hat transform for freq. 300Hz

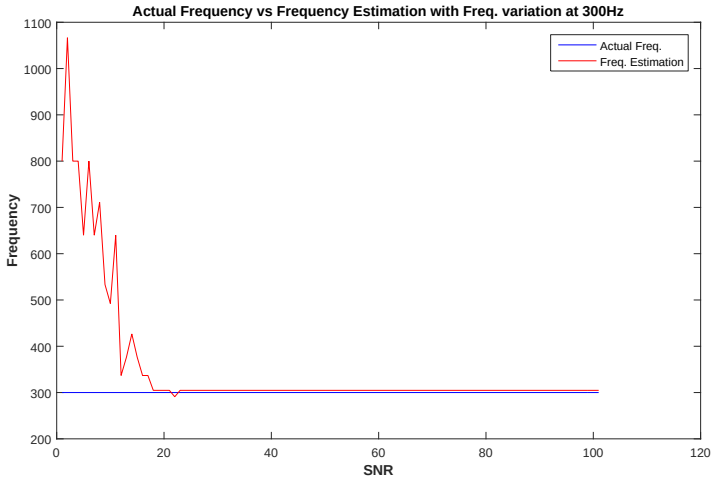

Figure 6.12: Actual frequency vs estimated frequency for various SNR at freq. 300Hz

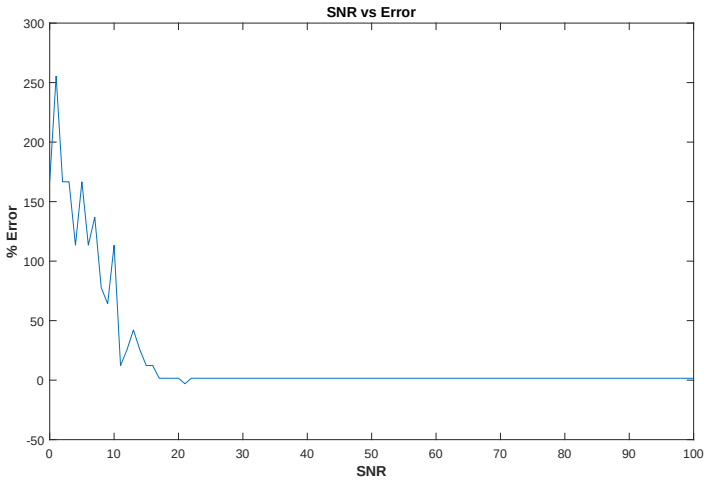

Figure 6.13: SNR vs error at Freq. 300Hz

At 500Hz, error for this strategy is less than 10% of the actual frequency when the SNR value of the signal is bigger than 8dB, and it can be seen in Figures 6.14 to 6.16.

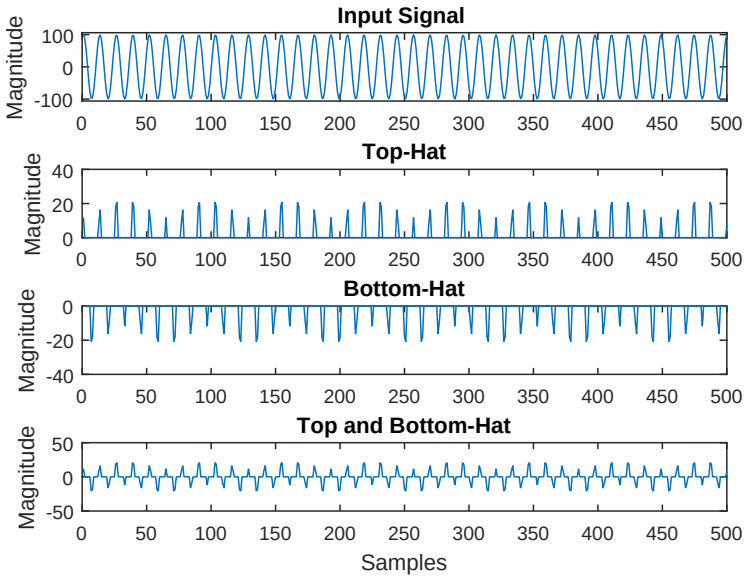

Figure 6.14: Results of top-hat and bottom-hat transforms for freq. 500Hz

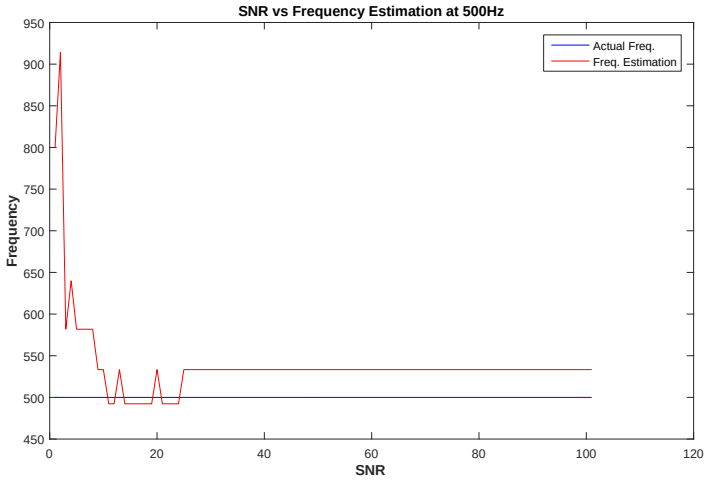

Figure 6.15: Actual vs estimated frequency for various SNR at Freq. 500Hz

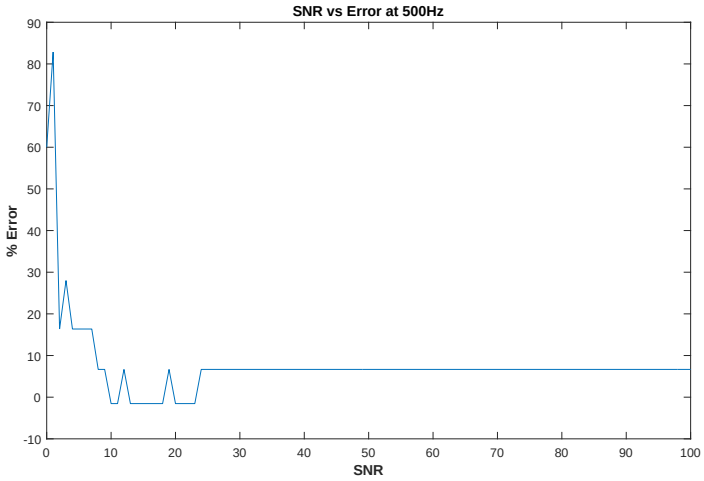

Figure 6.16: SNR vs error at freq. 500Hz

Successful results have been made for this strategy when the signal has a frequency of 800Hz with SNR is higher than 1. The simulation results for this frequency can be seen in Figures 6.17 to 6.19.

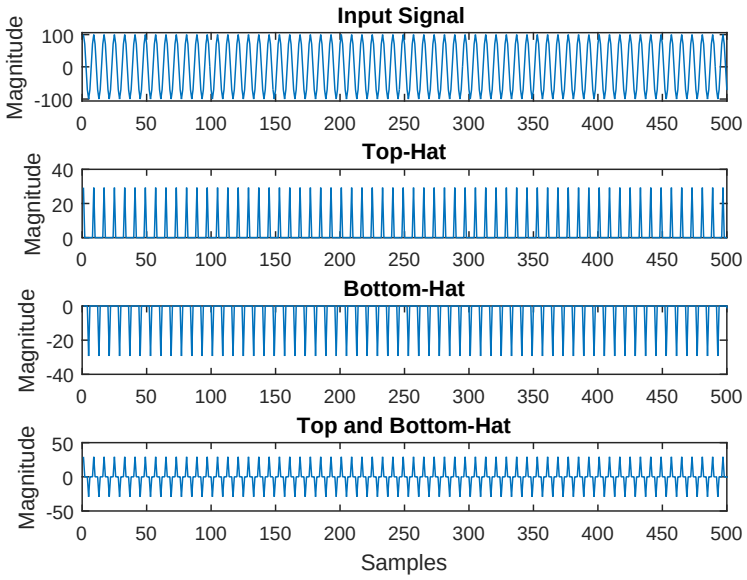

Figure 6.17: Results of top-hat and bottom-hat transforms for freq. 800Hz

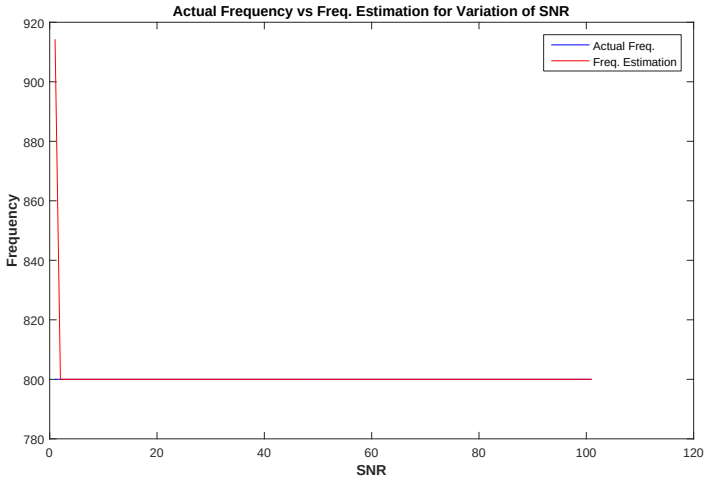

Figure 6.18: Actual vs estimated frequency for various SNR at freq. 800Hz

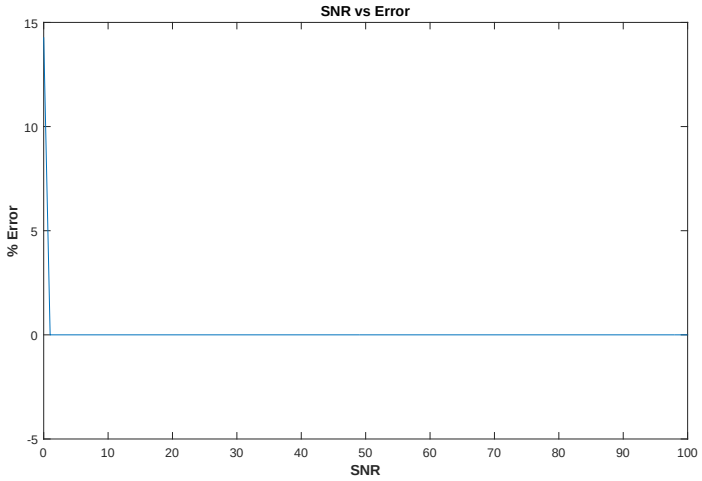

Figure 6.19: SNR vs error at freq. 800Hz

The proposed method also has been tested for frequency of 1kHz. The results can be seen in Figures 6.20 to 6.22.

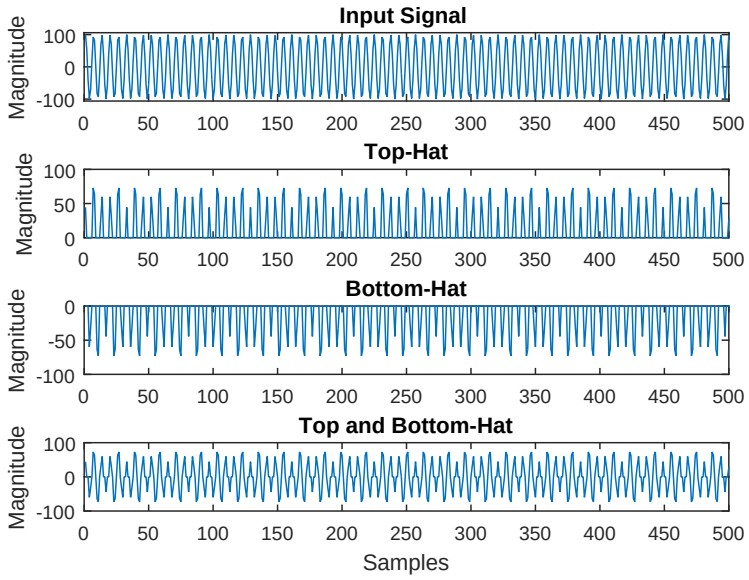

Figure 6.20: Results of top-hat and bottom-hat transforms for freq. 1000Hz

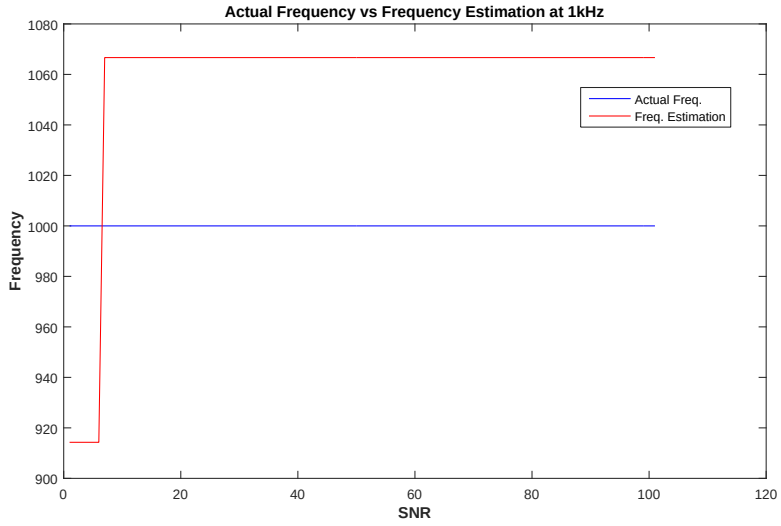

Figure 6.21: Actual vs estimated frequency for various SNR at freq. 1000Hz

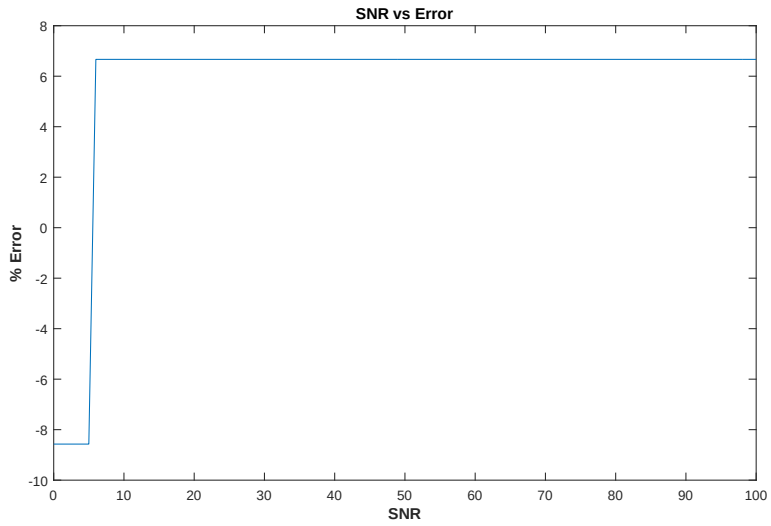

Figure 6.22: SNR vs error at freq. 1000Hz

The error for the signal at 1kHz is 6.5% of the actual frequency for the SNR greater than 8dB, while the estimated frequency dropped to 8.5% below the actual frequency for SNR between 0 to 8dB.

6.3.3 Simulation Results for PMU Application

The simulations have also been done for PMU where the based frequency of the signal at 50Hz or 60Hz. In these simulations, the range of the frequency of the signal were between 45Hz to 65Hz. The results for noise-free and signal with noise with SNR 30dB can be seen in Figures 6.23 to 6.26.

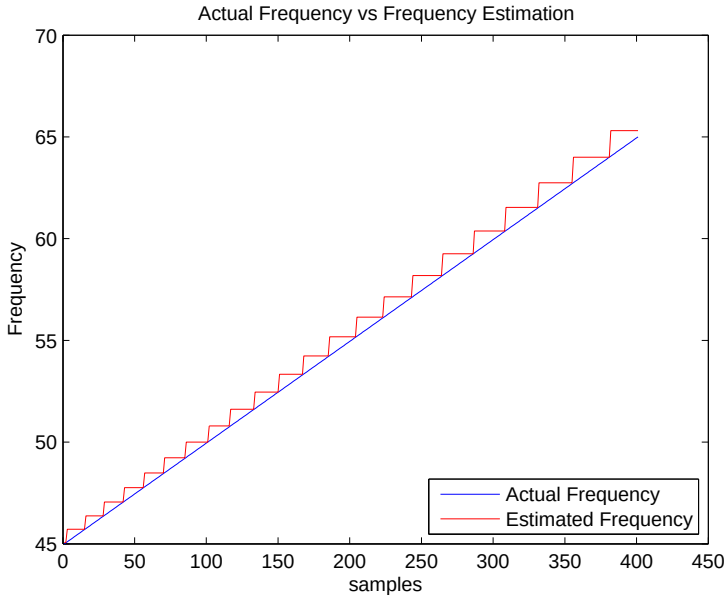

Figure 6.23: Actual vs estimated frequency of noise-free signal for PMU application

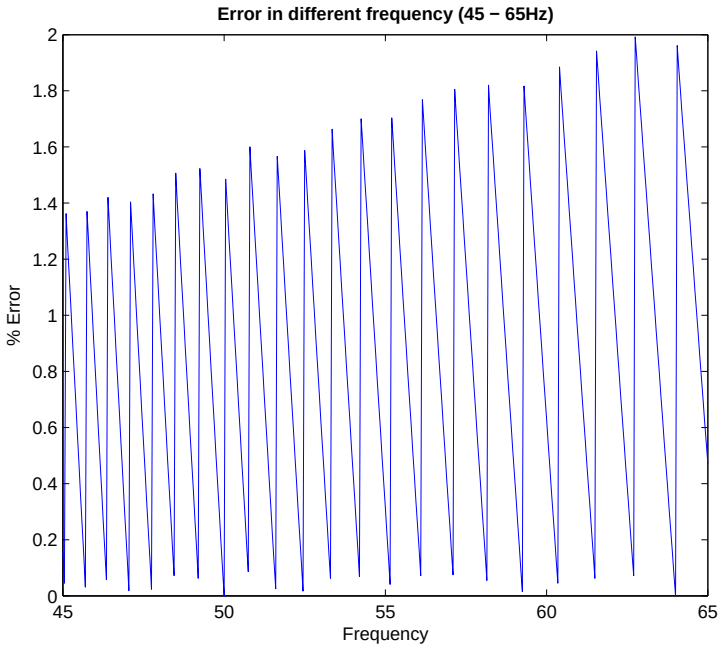

Figure 6.24: Error of estimated frequency of noise-free signal for PMU application

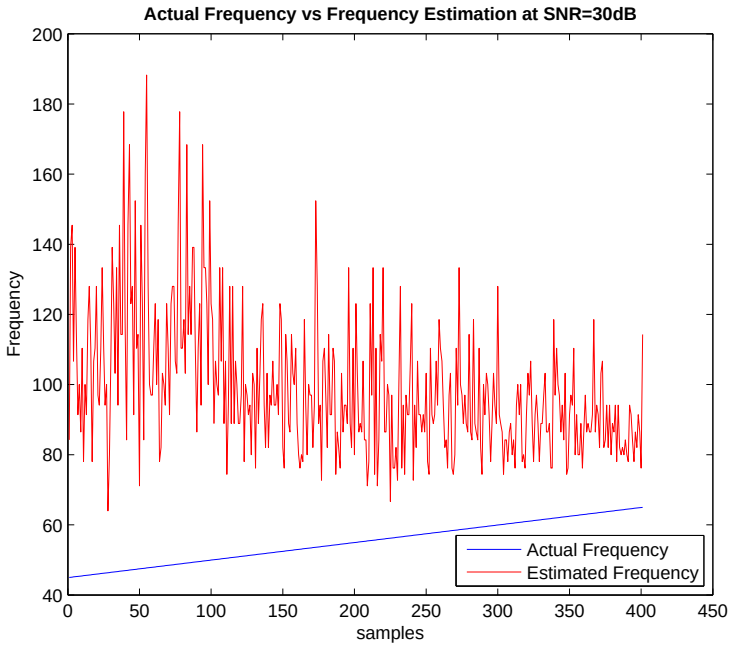

Figure 6.25: Actual vs estimated frequency at SNR = 30dDB for PMU application

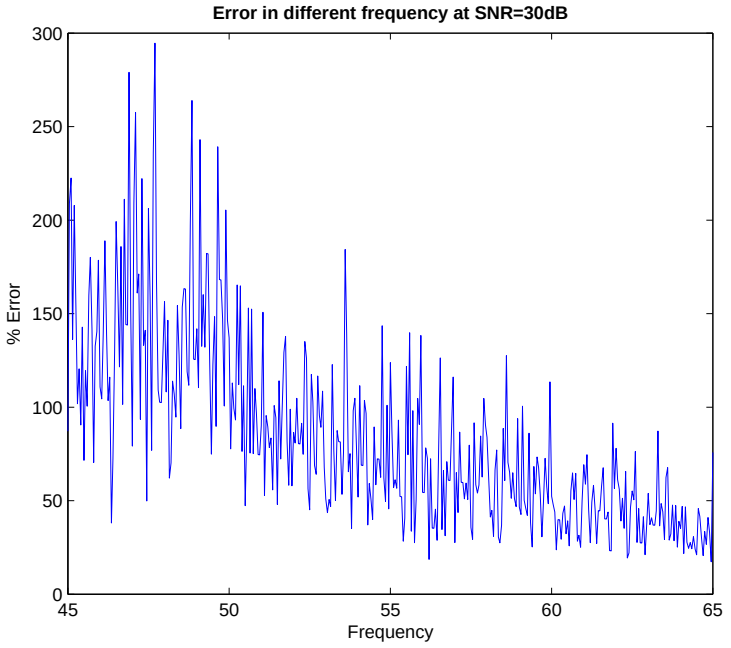

Figure 6.26: Error of estimated frequency at SNR = 30dB for PMU application

From Figures 6.23 to 6.26, it is clearly seen that the proposed method can estimate the frequency of the noise-free signal between 45Hz to 65Hz with the average error is only 0.87%. Contrary for the signal with SNR at 30dB, the estimation has an average error at 84.26591%. This result means that this proposed method is not good enough for estimating the signal with SNR at 30dB.

The simulation has also been conducted using fast fourier transform (FFT), and the result for this FFT comparing with the proposed method can be seen in Figure 6.27

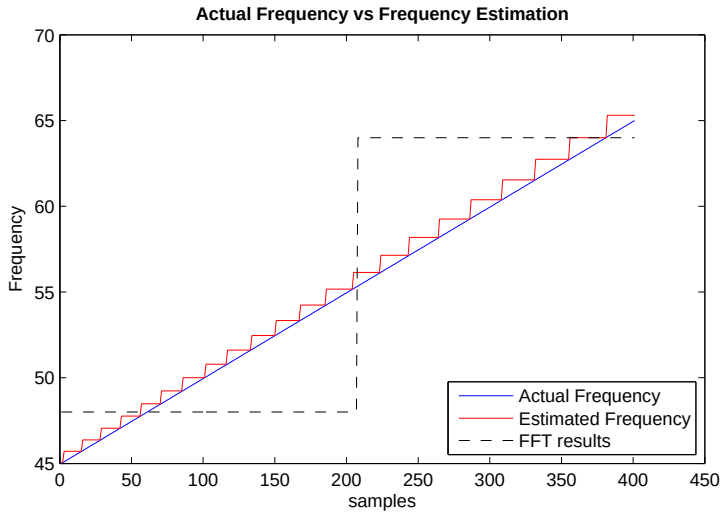

Figure 6.27: Error of estimated frequency at SNR = 30dB for PMU application

As shown in Figure 6.27, the proposed method has a better result with average error was 0.87% compared to the FFT that has 55.74% of average error.

6.4 Summary

This proposed strategy is based on the top-hat and bottom-hat transforms to estimate the frequency of the signal. The results show this method can handle low frequencies when the signal is a noise-free signal while this method cannot handle low frequency, especially lower than 40Hz, in the signal containing noise with SNR below 30 dB. For various values of SNR, the higher the frequency the better results have been obtain with the optimum result

at frequency 800Hz. For the frequency estimation of noise free signal for PMU application, this method gave a good result with the average error is only 0.87%, but this method fail to get an accurate results for signal with SNR at 30dB.

Average error of the proposed method is 0.87%, and this result is better than the FFT that has average error 55.78%

This method is an alternative method in estimating the frequency of a signal. By using MM, the burden in calculation when using traditional methods can be reduced.

This proposed method also found that the errors become bigger for higher frequency. It needs to do some further research for finding the finding the source of the errors and then eliminating them to make a better results.

Chapter 7

Mathematical Morphology and Probabilistic Neural Network for Identification and Classification of Disturbances

7.1 Introduction

Neural networks (NN) has been applied in detecting and classifying power quality disturbances. A self-adapting artificial neural networks (SAANN) is one of the example of the application of NN [82]. A Feed Forward neural network (FFNN) has also been used for classifying disturbances in order to resolve the problem of automatic discriminate of the recorder in power system [83].

NN is also combined with other methods for this purposes. One of them is Discrete wavelet transform (DWT) technique [84] which is integrated with probabilistic neural networks for constructing a classifier. Energy distribution features were extracted using Parseval's theorem. This method can reduce distortion signal. This wavelet transforms and artifi-

cial neural networks has also been investigated for power transformer disturbances [85], for classifying power quality disturbances in the supply to induction motor [86], and also for classifying stator winding insulation faults on a three-phase induction motor [87].

Another method is using S-transform combined with modular neural network [88], S-transform combined with probabilistic neural network (PNN) [89], and S-transform based artificial neural network classifier and ruled-based decision tree [90]. The result of features that were extracted using S-transforms then were trained for automatic classification by using PNN. Artificial neural network was also combined with wavelet for classification power quality disturbances [91].

NN was also combined with fuzzy logic [92] or Teager energy operator [93] to detect and classify power quality disturbances.

In this chapter, the detection and classification of disturbances using mathematical morphology and neural networks will be introduced. The Half Multi-resolution Morphology Gradient (HMMG) is used to detect the disturbances and as input to the Probabilistic Neural Network for classifying 9 types of disturbances. PNN is an improvement of Back Propagation Network (BPN) which is the most used in neural network paradigm. The same results in classification accuracy are determined both using PNN or BPN but PNN trains quickly compare to BPN [94]. Unlike Fourier transform and wavelet transform that analyse in frequency domain, in this proposed method the analysis was done in time domain.

7.2 Probabilistic Neural Network

Classification

The Probabilistic Neural Network model is also known as a feed forward neural network. This method is based on Bayesian classification and classical estimators for probability density functions [95]. The parent Probability Density Function (PDF) of each class in the PNN algorithm is estimated as an approximation of a Parzen window and a non - parametric function. These estimated densities are then used in a Bayes decision rule to

perform the classification. By knowing the PDF of of each of the population, then an unknown x belongs to class i if:

$$f_i(x) > f_j(x), \text{for all } j \neq i \tag{7.2.1}$$

where f_k is the pdf for class k.

The PNN was introduced by D.F. Specht in 1966 [95] that was derived from the Bayesian Network and a statistical algorithm called Kernel Fisher discriminant analysis that has the capability to minimize the probability of mis-classification (c). Bayes optimal decision rule is denoted as follows:

$$h_i c_i f_i > h_j c_j f_j, \text{for all } j \neq i \tag{7.2.2}$$

where h is prior probability which represents the probability of an unknown sample being drawn from a particular population and c is a misclassification cost which expresses the cost of incorrectly classifying an unknown.

PDF Estimation

Samples of the populations (the training set) are needed to estimate the PDF. For a single population, the PDF is calculated using Parzen's pdf estimator and can be written as follows:

$$1/n\sigma \sum_{k=1}^{n} W(x - x_k/\sigma) \tag{7.2.3}$$

where:

- x: unknown (input)
- x_k: k^{th} sample
- W: weighting function
- σ : smoothing parameter.

This formula exactly expresses the average of the pdf's for the n samples in the population when σ is a smoothing parameter.

The Gaussian function is commonly used as the weighting function since it behaves well and easily computed and also it isn't related to any assumption about a normal distribution. The estimated pdf that uses the Gaussian function can be denoted as follows:

$$g(x) = 1/n\sigma \sum_{k=1}^{n} \exp(-(x - x_k)^2/\sigma^2) \tag{7.2.4}$$

For the n_i samples in the i^{th} population, the classification criteria can be expressed as follows:

$$g_i(x) = \frac{1}{n_i} \sum_{k=1}^{n} \exp(-\frac{||x - x_k||^2}{2\sigma^2}) \tag{7.2.5}$$

where $||x - x_k||$ is the Euclidean distance between the vectors X and X_k.

Equation 7.2.5 is modified and then applied to the output of vector H of the hidden layer in PNN, and it can be denoted as follows:

$$H_h(x) = \exp\frac{||x - x_k||^2}{2\sigma^2} \tag{7.2.6}$$

where:

$$net_j = \frac{1}{N_j} \sum_h W_{hj}^{hy} H_h \text{ and } N_j = \sum_h W_{hj}^{hy};$$
$$net_j = \max_k(net_k) \text{ then } y_j = 1, \text{else } y_j = 0$$

The architecture of a PNN can be seen in Figure 7.1. In this figure, W_{ih}^{xh} is the connection weight between the input layer X and the hidden layer H and W_{hy}^{hj} is the connection weight between the hidden layer H and the output layer Y.

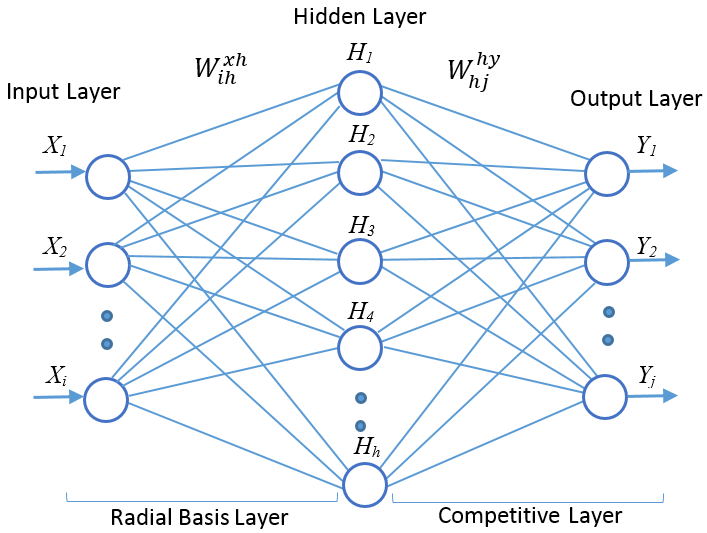

Figure 7.1: Architecture of a PNN

The PNN has 3 layers of nodes, the input layer, the hidden layer and the output layer. The input layer (on the left) contains i nodes: one for each of the i input features of a feature vector. In the middle is the hidden layer where each feature input node is connected to all nodes in the hidden layer. It means that each hidden node receives the complete input feature vector X. Each hidden node corresponds to a Gaussian function centered on its associated feature vector. All of the Gaussians feed their functional values to the output layer node Y_j.

7.2.1 Training

For effective classification, a representative of the actual population as the training set of PNN must be used. The sparse set should be sufficient and the range of error of the samples is tolerable. Adding and removing training samples simply involves adding or removing ”neurons” in the pattern layer. When the training set increases in size, the PNN asymptotically converges to the Bayes optimal classifier.

It is essential to determine the value of the smoothing parameter (σ) in the training process. The principle advantages of PNN process is much faster than backpropagation [94]. The relationship between σ and its corresponding correct classification can be seen in Figure

7.2 [96]. This figure is a graphical result of the experiment in diagnostic accuracy as a function of the smoothing parameter.

Nearest neighbour decision rule has implemented for the initial of the testing. Peak diagnostic accuracy (optimum value) can be obtained with any σ between some value of the smoothing parameter. It is not at all difficult to find a good value of σ experimentally because this peak of the curve is also sufficiently broad. In addition, any σ in the range before and after the optimum values give only slightly poorer compare to the best value. For the all values of the σ from 0 to $\inf$ matched filter, the significantly better results can be achieved compare to those to be expected from classification by chance.

In order to determine σ, an educated guess based on knowledge of the data is used, and estimating its value using a heuristic technique like Jackknifing [97].

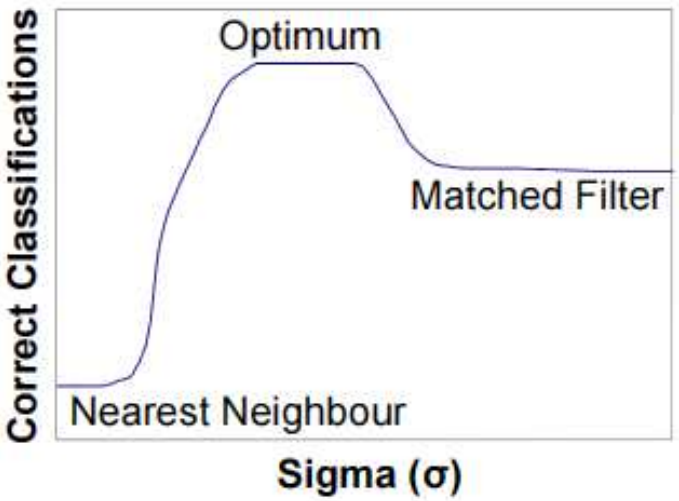

Figure 7.2: Relationship between sigma and correct classification

Jackknifing is used to grade the performance of each tested sigma (σ). Systematic testing of the values for sigma can be done by bonding the optimal value to some interval and shrinking the interval.

The Scaled Conjugate Gradient

For the training stage in this simulation using Matlab, a network training function ($trainscg$) updates weight and bias values according to the scaled conjugate gradient method. This method is based on conjugate directions, but this algorithm does not perform a line search at each iteration [98].

The algorithms for the training stage in Matlab can be described that the training stops when any of these conditions occurs:

- The maximum number of epochs (repetitions) is reached.
- The maximum amount of time is exceeded.
- Performance is minimized to the goal.
- The performance gradient falls below minimum gradient.
- Validation performance has increased more than maximum fail times since the last time it decreased (when using validation).

Cross Entropy Error Function

The cross entropy error function is used to resolve the problem during the learning process using the mean square error (MSE) [99]. An extremely slow reduction error happens when using the MSE. The cross entropy error function improves the network performance shorter stagnation period, and can be denoted as follows:

$$E_m = \frac{1}{m}\sum_{k=1}^{m}[t_k \ln y_k + (1 - t_k) \ln(1 - y_k)] \tag{7.2.7}$$

where t_k is the target value and y_k is the actual network value and m is the number of samples.

The error E_m is minimized by updating each weight proportional to the partial derivative of E_m with respect to the weight W_{jk}, so E_m becomes:

$$\frac{\partial E_m}{\partial W_{jk} m} = \sigma(y_k - t_k).z_j \tag{7.2.8}$$

where z_j is hidden layer.

In Matlab, most neural networks training computation by a CPU is compiled using the MEX (Matlab Executable) algorithm while for large networks the calculations might occur with a MATLAB calculation mode.

7.2.2 Application Areas of PNN

There are many applications of the PNN in solving some problems in signal processing. These applications include two categories such as classification and diagnostic, and also pattern recognition.

Classification and diagnostics:

- Classification of brain tissues in multiple sclerosis
- Classification of image textures
- Classification of soil textures
- Classification of liver tumors
- Power disturbance recognition and classification
- Cloud classification:

Pattern recognition:

- Application in pattern recognition problems
- Independent text recognition
- Speech recognition like speaker identification systems
- Application in human face recognition
- Application in speaker verification
- Applications in solving signal processing problems
- EEG pattern classification

7.3 Proposed Method

There are two stages in this proposed method, disturbances detection stage and disturbances classification stage. In detecting the disturbances, a HMMG method has been undertaken by extracting the sudden changing in the signal as a starting and ending point of the disturbances. Standard deviation, mean, maximum, minimum value and energy of the signal after HMMG are used as inputs of the classification of disturbances stage using Neural Network.

In this research, the block diagram of the PNN simulation can be seen in Figure 7.3.

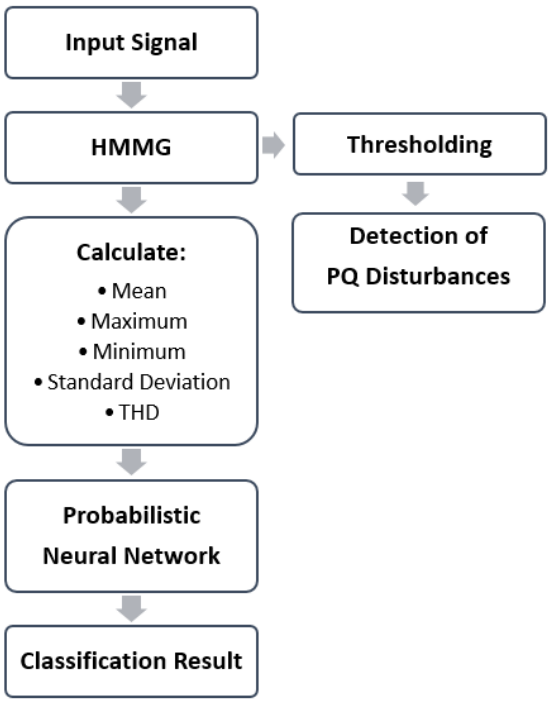

Figure 7.3: Block diagram of PQ classification using HMMG and PNN

.

7.3.1 Generation of PQ Disturbances

A database of PQ disturbances is needed both in single and multiple condition for identification and classification. These synthetic data can be generated using numerical models

and their parameters for duration and magnitude of the disturbances based on IEEE Standard 1159 - 2009 [61].

1. Pure Sine
   (a) $V(t) = A\, sin(\omega t)$
   (b) $A = 1\,(pu),\ \omega = 2\pi 50$ rad/sec
2. Sag
   (a) $V(t) = (1 - \alpha(u(t - t_1) - u(t - t_2)))\, sin(\omega t)$
   (b) $0.1 \leq \alpha \leq 0.9,\ T \leq t_2 - t_1 \leq 9T$
3. Swell
   (a) $V(t) = (1 + \alpha(u(t - t_1) - u(t - t_2)))\, sin(\omega t)$
   (b) $0.1 \leq \alpha \leq 0.8,\ T \leq t_2 - t_1 \leq 9T$
4. Interruption
   (a) $V(t) = (1 - \alpha(u(t - t_1) - u(t - t_2)))\, sin(\omega t)$
   (b) $0.9 \leq \alpha \leq 1.0,\ T \leq t_2 - t_1 \leq 9T$
5. Flicker
   (a) $V(t) = (1 + \alpha_f\ sin(\beta\omega t))\, sin(\omega t)$
   (b) $0.1 \leq \alpha_f \leq 0.2,\ 5 \leq \beta \leq 20Hz$
6. Low Frequency Oscillatory Transient
   (a) $0.1 \leq \alpha \leq 0.8,\ 0.5T \leq t_2 - t_1 \leq 3T$
   (b) $8ms \leq \tau \leq 40ms, 300 \leq f_n \leq 900Hz$
7. High Frequency Oscillatory Transient
   (a) $0.1 \leq \alpha \leq 0.8,\ 0.5T \leq t_2 - t_1 \leq 3T$

(b) $5\mu s, 0.5 \leq f_n \leq 5MHz$

8. Harmonics

   (a) $V(t) = \alpha_1\, sin(\omega t) + \alpha_3\, sin(\omega t) + \alpha_5\, sin(\omega t) + \alpha_7\, sin(\omega t)$

   (b) $0.05 \leq \alpha_3, \alpha_5, \alpha_7 \leq 0.15, \sum \alpha_i^2 = 1$

9. Sag with Harmonics

   (a) $V(t) = (1-\alpha(u(t-t_1)-u(t-t_2)))\, \alpha_1\, sin(\omega t) + \alpha_3\, sin(\omega t) + \alpha_5\, sin(\omega t) + \alpha_7\, sin(\omega t)$

   (b) $0.1 \leq \alpha \leq 0.9,\ T \leq t_2 - t_1 \leq 9T$

   (c) $0.05 \leq \alpha_3, \alpha_5, \alpha_7 \leq 0.15, \sum \alpha_i^2 = 1$

10. Swell with Harmonics

    (a) $V(t) = (1+\alpha(u(t-t_1)-u(t-t_2)))\, \alpha_1\, sin(\omega t) + \alpha_3\, sin(\omega t) + \alpha_5\, sin(\omega t) + \alpha_7\, sin(\omega t)$

    (b) $0.1 \leq \alpha \leq 0.8,\ T \leq t_2 - t_1 \leq 9T$

    (c) $0.05 \leq \alpha_3, \alpha_5, \alpha_7 \leq 0.15, \sum \alpha_i^2 = 1$

Type of disturbances for using in this strategy can be seen in Figures 7.4 to 7.6.

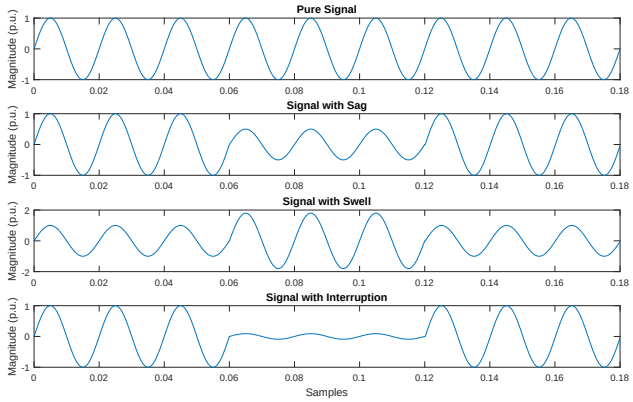

Figure 7.4: Input signal with sag, swell and interruption

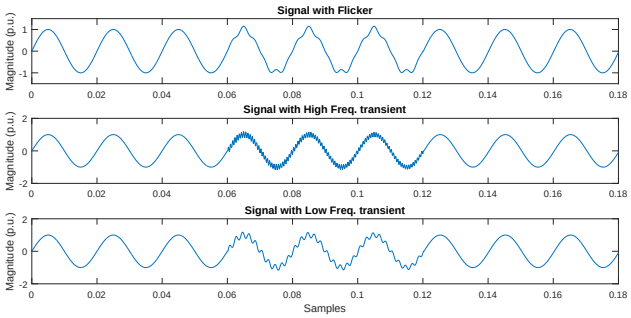

Figure 7.5: Input signal with flicker, low and high frequency transient

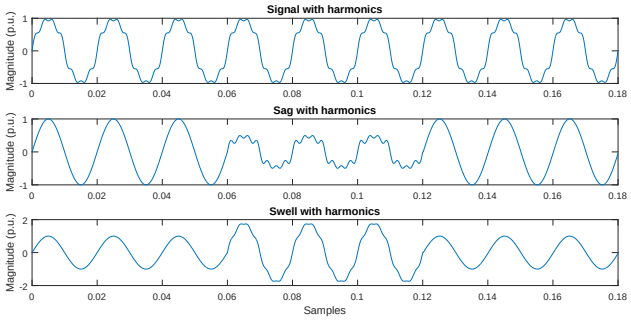

Figure 7.6: Input signal with harmonics, sag with harmonics, and swell with harmonics

For simulation using PNN, the following parameters were used:

- The pure signal has a frequency of 50Hz and magnitude in 1 per unit (p.u.).
- Duration of the signal is 3 cycles for each type of disturbances with 3 different magnitudes or parameters of the disturbances.
- 9 type of disturbances plus a pure signal were used for the simulation.
- The sampling frequency is 6.4kHz or 128 samples per cycle.
- 5 inputs are used
- 20 hidden layers are used on this PNN. The simulations have been done using 10 hidden layers, but the results were not satisfied, so the number of hidden layers were increased gradually, and a better result were obtain at 20 hidden layers.

- 10 outputs as a classification of disturbances are used in this PNN

As previously mentioned the duration of the signal is 3 cycles for each type of disturbances with 3 different magnitudes or parameters of the disturbances (Figure 7.7. So the total duration of every type of disturbance is 9 cycles. By using 128 samples per cycle, the total samples for one disturbance is 1152. The HMMG used 32 data for every iteration, making the total number of input of PNN for each type of disturbances 36 samples.

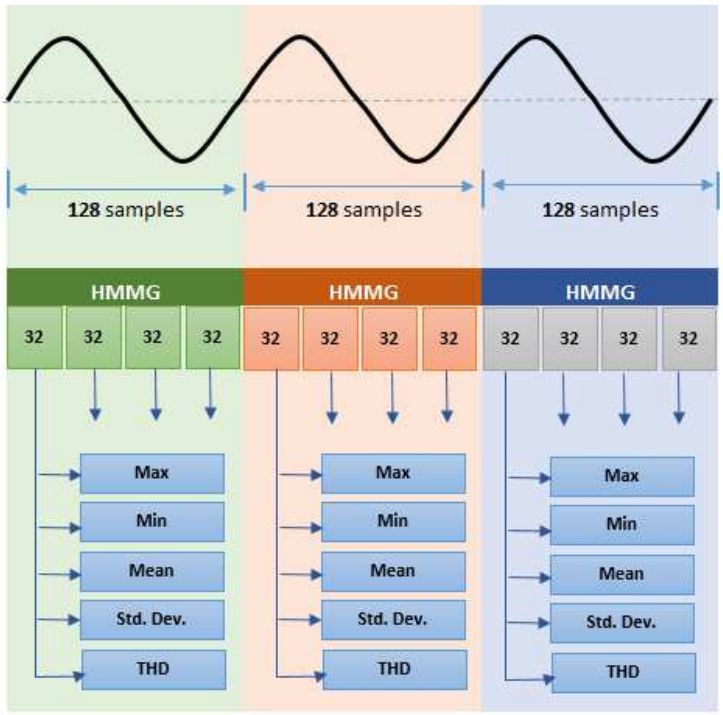

Figure 7.7: Input for PNN

In this simulation, the total number of samples are 11520 where each disturbance has 9 cycles duration. The signal with disturbances firstly was processed using HMMG for PQ disturbances detection. The effect of HMMG on this signals can be seen in Figure 7.8.

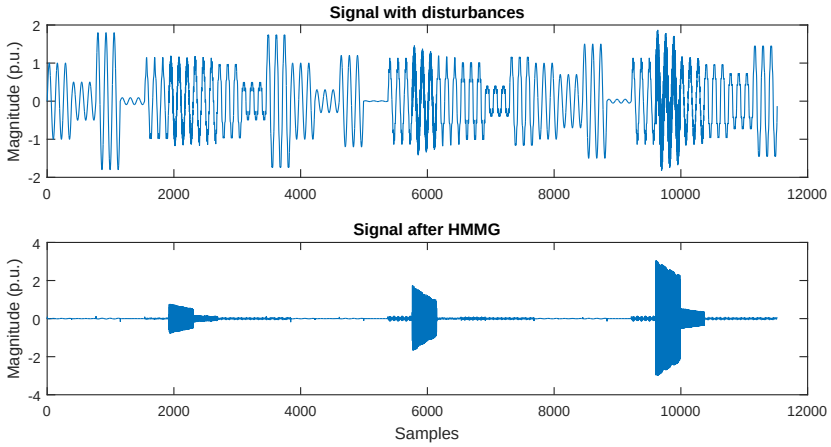

Figure 7.8: Signal with disturbances and the HMMG results

.

A number of samples that to be processed in each iteration is 32 or one quarter cycle. The resulting signal is then calculated to determine maximum, minimum, mean, standard deviation and Total Harmonics Distortion (THD) of the signal samples. All of these values become inputs of PNN.

The simulation for this strategy has been undertaken using a Pattern Recognition Neural Network of Matlab that can be seen in Figure 7.9. The number of the input of the PNN is 5, and 20 hidden layers were chosen to generate 10 output layers. This output as the classification of the power quality disturbances.

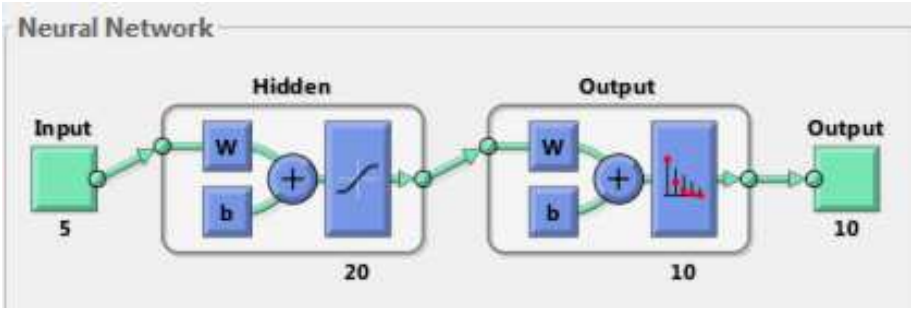

Figure 7.9: Pattern recognition neural network

7.4 Results

The classification of disturbances can be seen in the Table 7.1.

Table 7.1: Classification of disturbances

Class	Type of Disturbances	Duration	Range
C1	Pure Sine		1 p.u.
C2	Sag	0.5 - 20 cycles	0.1 - 0.9 p.u.
C3	Swell	0.5 - 20 cycles	1.1 - 1.8 p.u.
C4	Interruption	0.5 - 30 cycles	0- 0.1 p.u.
C5	Flicker		0- 0.1 p.u.
C6	Low Freq. Transient		0- 0.1 p.u.
C7	High Freq. Transient		0 - 0.1 p.u.
C8	Harmonics		0 - 0.2 p.u.
C9	Sag with Harmonics	0.5 - 20 cycles	0.1 - 0.9 p.u.
C10	Swell with Harmonics	0.5 - 20 cycles	1.1 - 1.8 p.u.

The training results of this method can be seen in Figures 7.10 to 7.14.

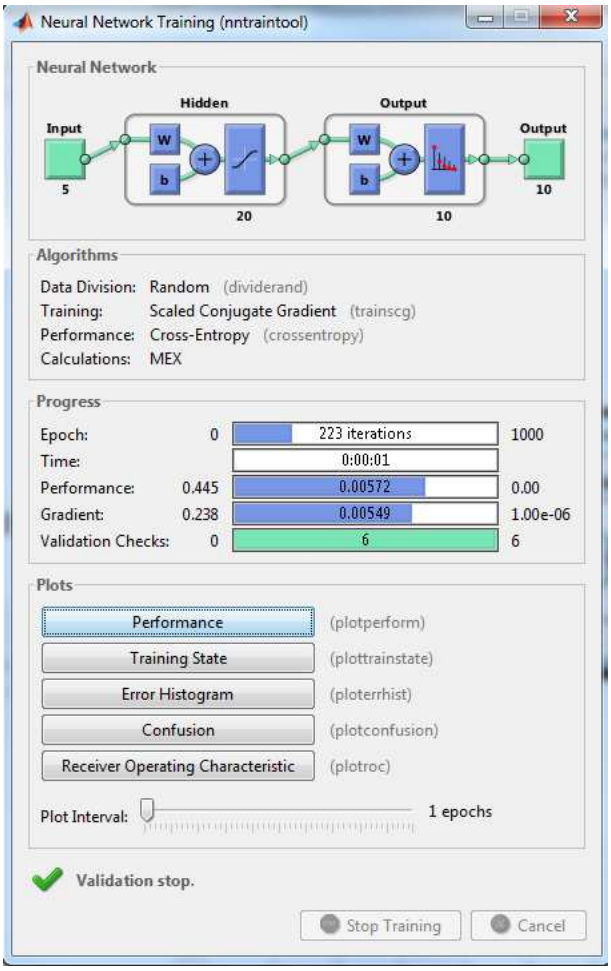

Figure 7.10: Neural network training tool

The best validation performance plot can be seen in Figure 7.11. In this plot, Cross-Entropy values are shown for all datasets in logarithmic scale. This training Cross-Entropy is decreasing. The best validation performance will be reached when the minimum value of MSE is reached. The training then continued for six more iterations before the training stopped. In this case, the best validation performance is 0.0069707 after 217 iterations (epochs), and the training stopped at 223 epochs.

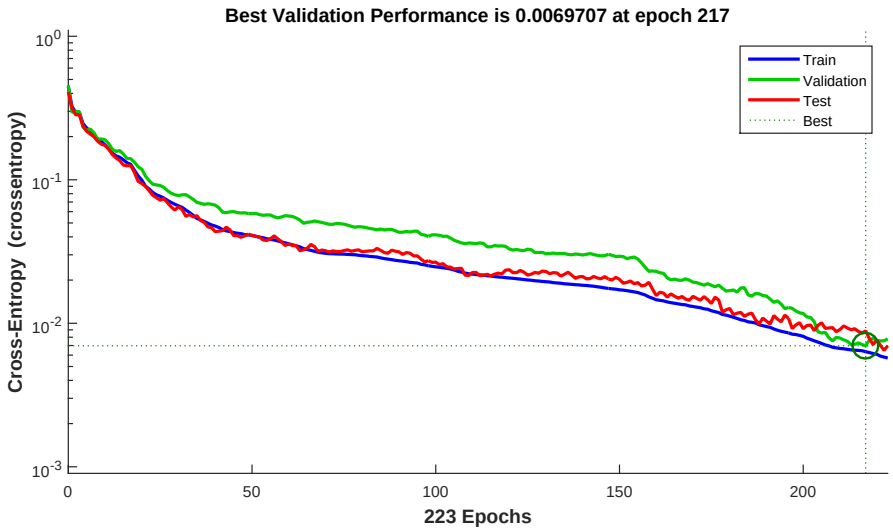

Figure 7.11: Best validation performances

The result for the confusion matrix can be seen in Figure 7.12. In the Training Confusion matrix, one target from class 6 was incorrectly assigned to class 7. On the other hand, one target from class 7 was incorrectly assigned to class 6. These incorrect results happened between the low frequency transient (class 6) and the high frequency transient (class 7). The percentage of the training confusion matrix is 99.2%.

The Validation Confusion matrix generated an incorrect assignment when one target of class 7 became the class of 3, making the percentage of validation was 98.1%. For the Test Confusion, all targets or 100% were correctly assigned to the output class. So overall, 99.2% of the samples were successfully classified as the correct output classes as shown in the all Confusion matrix.

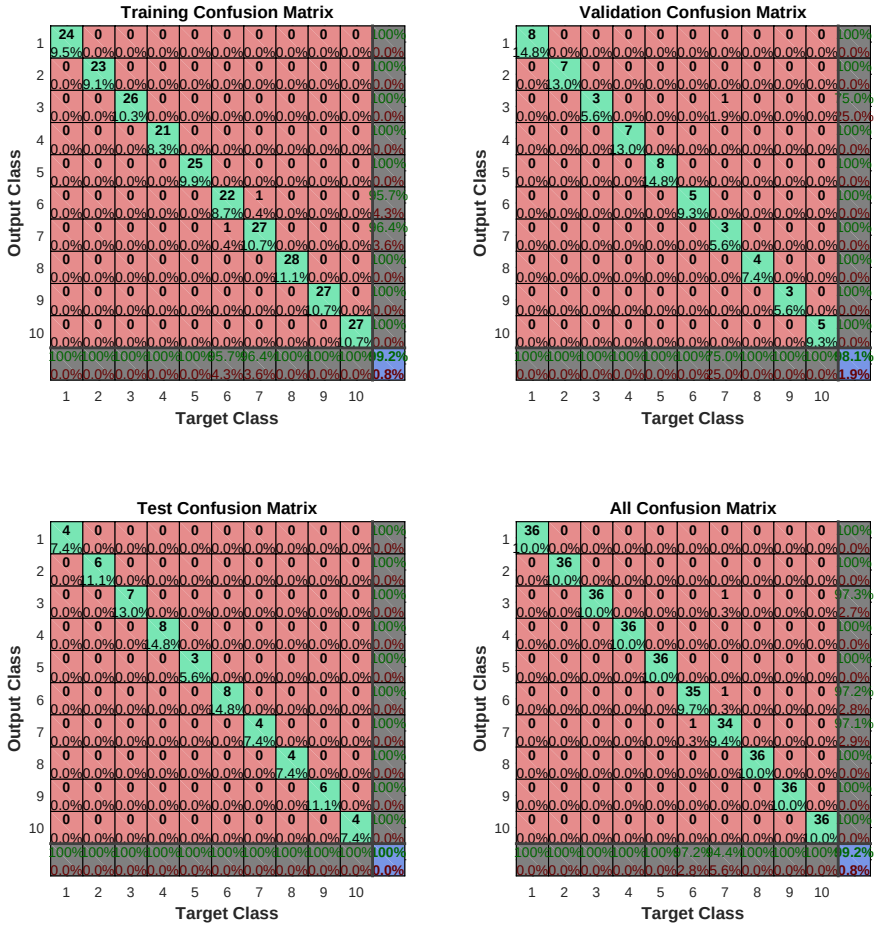

Figure 7.12: Confusion matrix

The training state, as shows in Figure 7.13, gives some other training statistics. A gradient value at 0.0054913 showed the value of backpropagation gradient on each iteration in logarithmic scale. This means that the training has reached the bottom of the local minimum of the goal function. Six validation checks have been done at epoch 223.

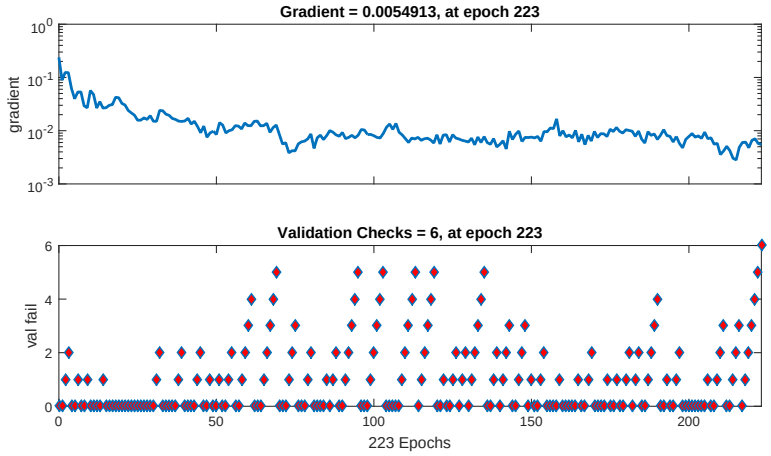

Figure 7.13: Training state

The training process result for Receiver Operating Characteristic can be seen in Figure 7.14.

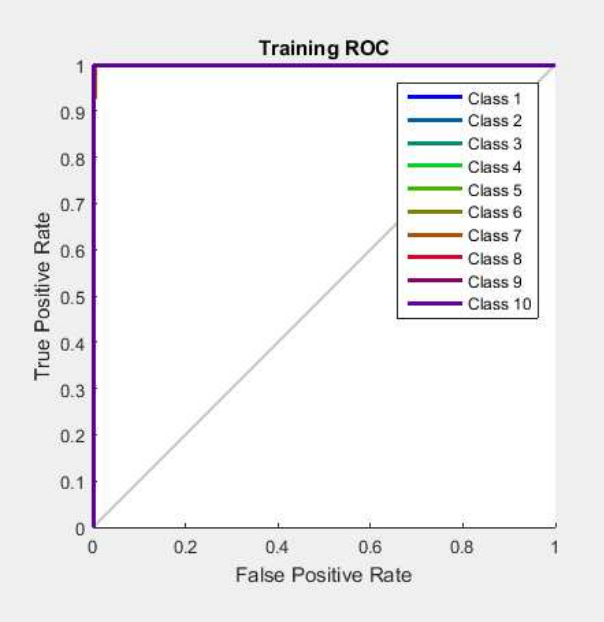

Figure 7.14: Receiver operating characteristic

The receiver operating characteristic is a metric used to check the quality of classifiers. So, from Figure 7.14 the quality of classifiers is 100%. This can be seen in that figure where

the training value for all class were gone to the true positive rate. This is because the more result tend to the true positive rate the better operating characteristic of the receiver.

The error of the training process as an histogram can be seen in Figure 7.15. It shows that a very small of error value was produced in this process. Most of errors for training, validation and test were about -0.03019 for the default 20 bins.

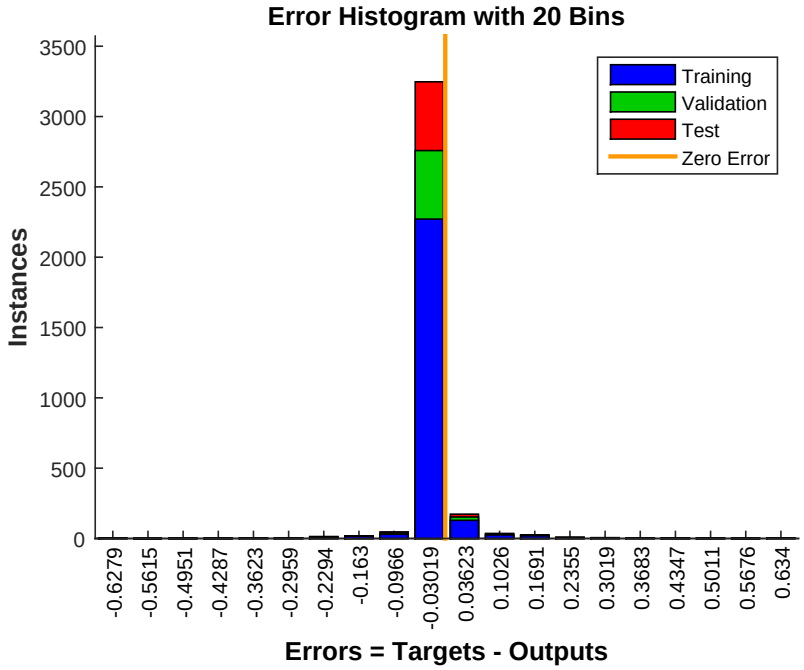

Figure 7.15: Error histogram

The simulation results for 36 samples for each type of disturbances can be seen in the Table 7.2. From this table, it is clearly seen that the proposed method can classify all type of disturbances with most of them at 100%. Only transient disturbances for both low frequency and high frequency have small error in the classification process when one sample of the low frequency has been detected as high frequency and one high frequency has been detected as low frequency.

Table 7.2: Simulation results of classification of PQ disturbances

Class	Description	C1	C2	C3	C4	C5	C6	C7	C8	C9	C10	CA
C1	Pure Sine	36	0	0	0	0	0	0	0	0	0	100%
C2	Sag	0	36	0	0	0	0	0	0	0	0	100%
C3	Swell	0	0	36	0	0	0	0	0	0	0	100%
C4	Interruption	0	0	0	36	0	0	0	0	0	0	100%
C5	Flicker	0	0	0	0	36	0	0	0	0	0	100%
C6	Low Freq. Transient	0	0	0	0	0	35	1	0	0	0	97.22%
C7	High Freq. Transient	0	0	1	0	0	1	34	0	0	0	94.44%
C8	Harmonics	0	0	0	0	0	0	0	36	0	0	100%
C9	Sag with Harmonics	0	0	0	0	0	0	0	0	36	0	100%
C10	Swell with Harmonics	0	0	0	0	0	0	0	0	0	36	100%
Percentage Correct of classification: 99.167%												
Percentage Incorrect Classification: 0.833%												

The simulation has also been done for signal with SNR at 30dB. The error histogram and confusion matrix results can be seen in Figures 7.16 and 7.17 respectively.

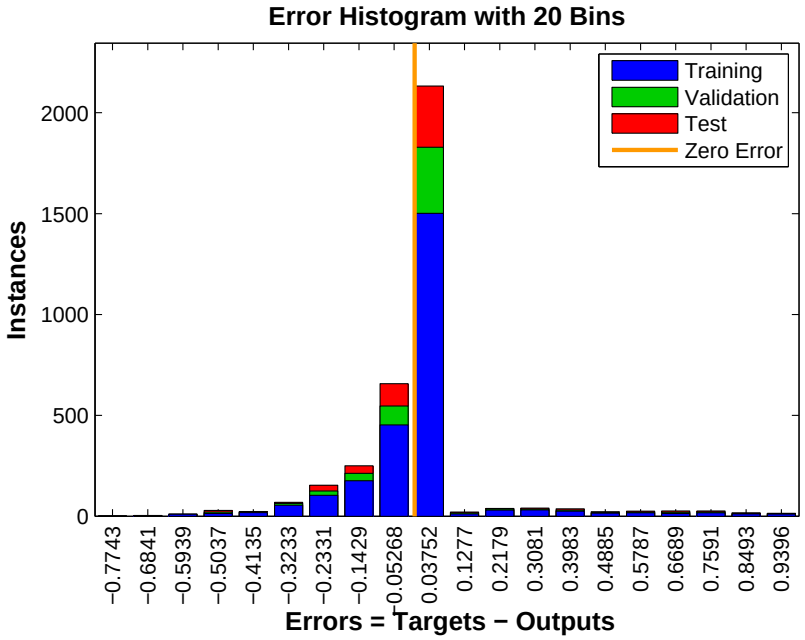

Figure 7.16: Receiver operating characteristic

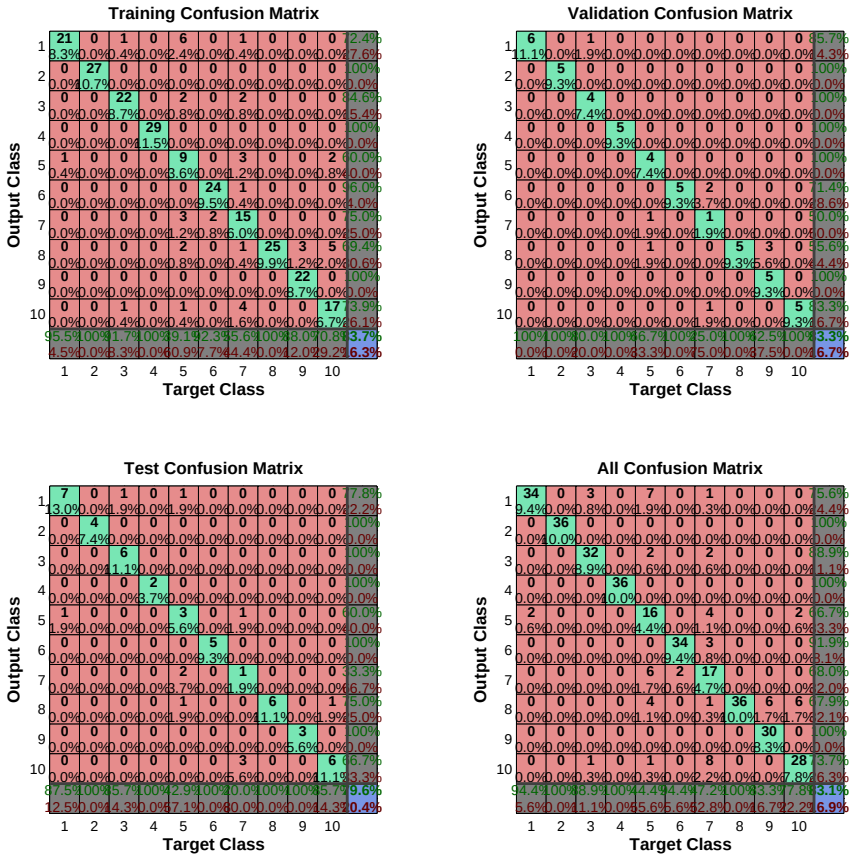

Figure 7.17: Receiver operating characteristic

From Figure 7.17, the percentage correct of classification were 79.63% for the test confusion matrix and 83.1% for all of the confusion matrix. This matrix can be shown in Table 7.3. The results show that the noise in the signal reduced the percentage correct of classification significantly. In this case, the correct classification for the 36 samples of the signal was dropped to 83.1%.

Table 7.3: Simulation results of classification of PQ disturbances for Signal with SNR=30dB

Class	Description	C1	C2	C3	C4	C5	C6	C7	C8	C9	C10	CA
C1	Pure Sine	34	0	0	0	2	0	0	0	0	0	94.4%
C2	Sag	0	36	0	0	0	0	0	0	0	0	100%
C3	Swell	3	0	32	0	0	0	02	0	0	1	88.9%
C4	Interruption	0	0	0	36	0	0	0	0	0	0	100%
C5	Flicker	7	0	2	0	16	0	6	4	0	1	44.4%
C6	Low Freq. Transient	0	0	0	0	0	34	2	0	0	0	94.4%
C7	High Freq. Transient	1	0	2	0	4	3	17	1	0	8	47.2%
C8	Harmonics	0	0	0	0	0	0	0	36	0	0	100%
C9	Sag with Harmonics	0	0	0	0	0	0	0	6	30	0	83.3%
C10	Swell with Harmonics	0	0	0	0	2	0	0	6	0	28	77.8%
Percentage Correct of classification: 83.1%												
Percentage Incorrect Classification: 16.9%												

Comparison results of the proposed method to other methods can be seen in Table 7.4. The proposed method has a better accuracy compare to PNN with S-Transform [89] or adaptive linear network (ADALINE) with fast forward neural networks (FFNN) [100].

Table 7.4: Accuracy of proposed method vs other methods

Methods	Accuracy
$PNN + S - Transform_{[89]}$	98.640%
$ADALINE + FFNN_{[100]}$	98.091%
$PNN + HMMG$	99.167%

7.5 Summary

This proposed strategy is based on PNN to classify PQ disturbances. HMMG is used for disturbances detection. Input of the PNN are the mean, maximum, minimum and standard deviation values of the signal at the time when disturbance occurred. Overall results of the simulation show that PNN is able to classify the disturbances with accuracy 99.167% for the signal without noise and 83.1% for signal with 30dB noise.

Chapter 8

Experimental Based on Real Dataset of Disturbances

8.1 Preparation

In this chapter, the novel methods for detection disturbances using mathematical morphology are compared using a real dataset of disturbances. The aim of this step is to check whether the methods that have been developed can handle real disturbances in systems.

In the previous chapters, all data that have been evaluated for the proposed methods were simulated data. Simulated data of some disturbances were generated using some mathematical formula based on the IEEE Standard 1195-2009. Difference from the simulated data that have been used in this research which only for single type of disturbances in condition noise-free or with contain noise, real data contain more than one type of disturbances. Unlike the simulated data that can be sampled at high sampling frequency, number of samples per cycle of the real data also depends on the data acquisition instrument that has been used for collecting these real data.

For the real dataset of different disturbances, they were collected from three sources; IEEE DataPort, and two others from trials in the laboratory.

A dataset of the actual data for sag from the IEEE Dataport [101] was used in this

research. These datasets were collected from the power network of the University of Cadiz, Spain during 2011 to 2016. These real sag events are based on the 50Hz frequency and a sampling frequency of 20kHz (400 samples per cycle) with a duration of less than 3 seconds captured the event.

There are two kinds of experiments that have been conducted in order to capture disturbances. The first one is using the LabVolt module from Festo Didactic that can be seen in Figures 8.1 to 8.3. The Faultable Transmission Line module and three phase power supply module were used to collect the dataset of sag, swell and momentary interruption. The voltage range of the tunable 3 phase power supply is 240/415V. Each type of disturbance is generated by changing the value of power supply. Data were collected using an Tektronix TBS 1052B-EDU oscilloscope. The sampling frequency was 2.5kHz and the frequency of the power signal was 50Hz.

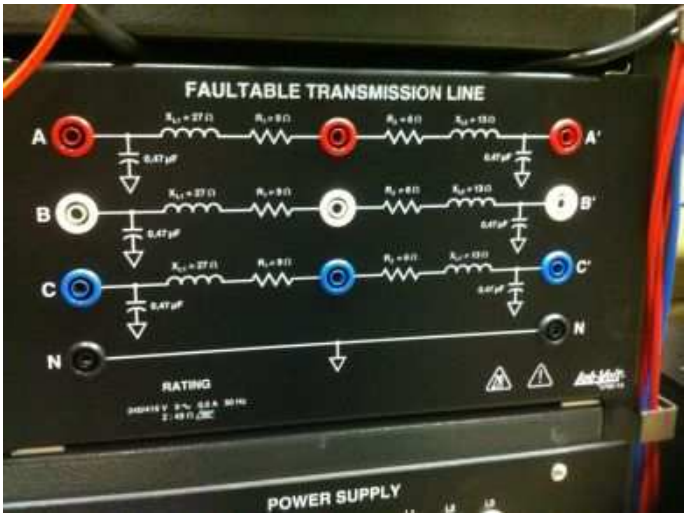

Figure 8.1: Faultable Transmission Line module

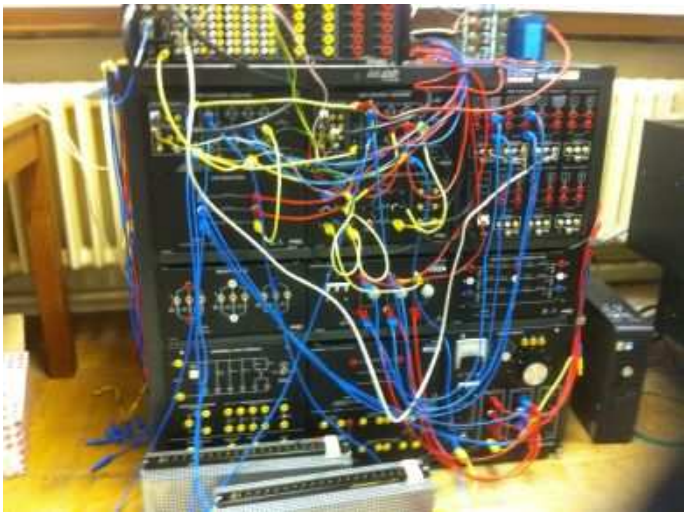

Figure 8.2: LabVolt module from Festo Didactic

Figure 8.3: 3 phase power supply

The second laboratory dataset was obtained using the system shown in Figure 8.4. This experiment used the FH2 MkIV Test Bed (Figure 8.5) with motors (three-phase ac cage rotor induction motor) and capacitors ($3 \times 20\mu$F) as loads. A data acquisition (DAQ) instrument DT300 Series from Data Translation was used to connect, via a data conditioning circuit to a personal computer with Labview software (Figure 8.6).

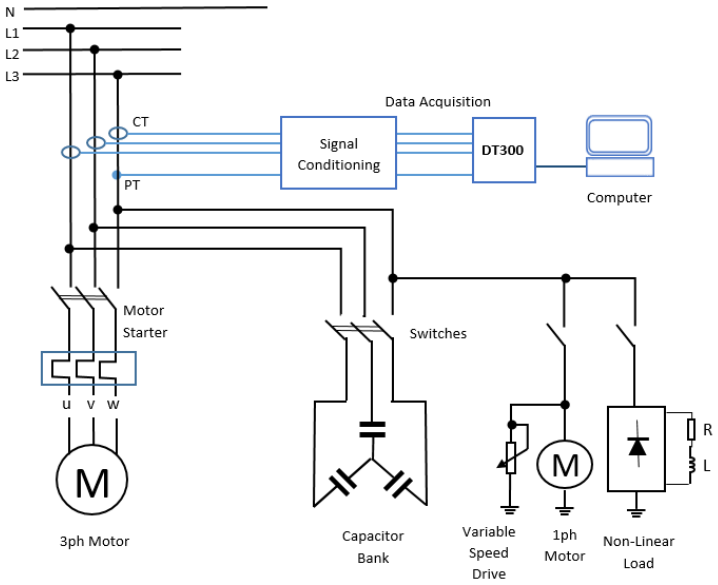

Figure 8.4: Diagram for data acquisition

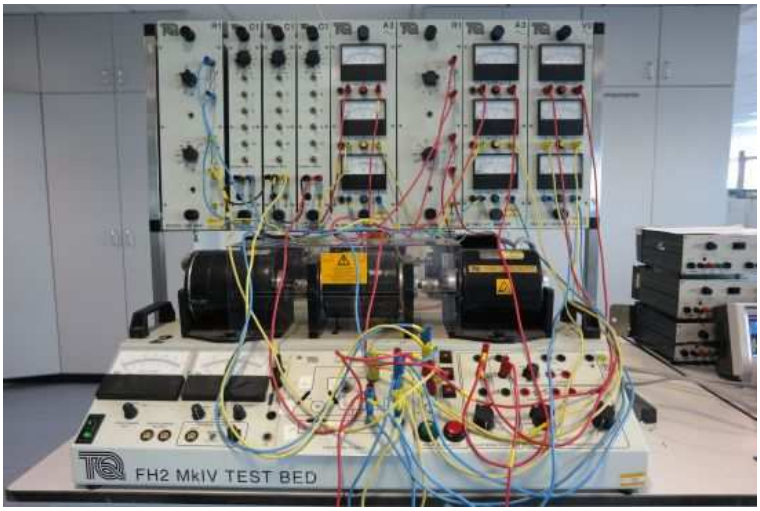

Figure 8.5: FH2 MkIV Test Bed

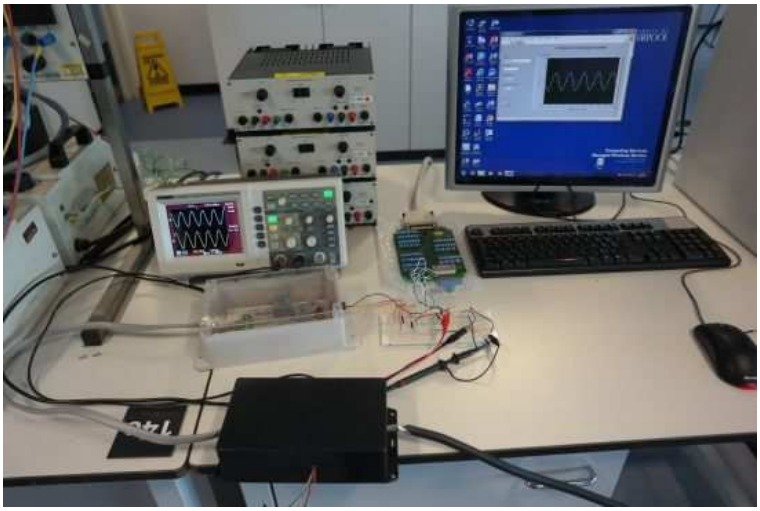

Figure 8.6: Data acquisition connection to a PC

The dataset was collected from the voltage supply in order to record voltage changes during starting and stopping a 3 phase motor and when a capacitor bank is injected into the system. The frequency signal is 50 Hz, with the value of voltages as 110/230Volt for both single phase and three phase. A sampling frequency of 25kHz was used to produce 500 data per cycle. An oscilloscope was also used for comparing the results of the data acquisition. This oscilloscope can only acquire a maximum of 2500 data points, compared to DAQ that

can be set depending on the number of data needed.

8.2 Testing Results

Using the datasets from the previous section, analysis with Matlab were conducted for the 3 novel strategies that have been presented in the previous chapters, skeletonization, conversion of the signal to image matrix in a small data window and an HMMG strategy. Three type of disturbances: voltage sag, voltage swell, and momentary interruption are used for the analysis and the number of datasets was 20 for each type of disturbance. Details of the dataset that are used on the all figures of the evaluation results can be seen in Table 8.1.

Table 8.1: Detail of dataset

Code	f_s **(kHz)**	**Length (samples)**	**Filename and Notes**
Source: IEEE Dataport **Feature: Sag** f_s**: 20kHz resample to 10kHz**			
D01	10	3500	{Realsignal Sag 80-71%_2011-11-07_12;31;26.txt}
D02	10	3500	{Real signal Sag 30-21%_2011-07-30_01;12;04.txt}
D03	20	11000	{Real signal Sag 80-71%_2012-05-09_09;34;10.txt}
D04	10	3500	{Real signal Sag 30-21%_2011-07-30_01;12;04.txt}
D05	10	3500	{Real signal Sag 60-51%_22011-10-22_08;05;25.txt}
Source: Experiment Lab 01 **Feature: Sag**			LabVolt module from Festo Didactic was used to produce some disturbances. Dataset is collected from the Faultable Transmission Line module and three phase power supply module using Oscilloscope. The disturbances were generated by changing the power supply to the system.
L01	2.5	1400	
Source: Experiment Lab 01 **Feature: Swell**			
L11	2.5	1400	
Source: Experiment Lab 01 **Feature: Interruption**			
L21	2.5	1400	
Source: Experiment Lab 02 **Feature: Transient**			Datasets were acquired from FH2 MkIV Test Bed when the motor was started and stopped. Datasets also were collected when the capacitor banks were energized to the system.
T01	25	2500	
T02	25	2500	
T03	25	2500	
T04	25	2500	

8.2.1 Skeletonization

The evaluation was conducted using 20 datasets from the Dataport and laboratory experiments with sampling frequency at 2.5kHz, 20kHz, and 10kHz. The 10kHz dataset was generated from the resampling of the 20kHz dataset. Most of the duration of the dataset is 3500 samples or based on the duration of the disturbance.

Twenty datasets of voltage sag from the IEEE Dataport [101] were simulated using the skeletonization method. In order to match with the skeletonization strategy in chapter 3, the magnitude of the data was converted from 300 volts to 10 volts. The results of simulation can be seen in Figures 8.7 to 8.9.

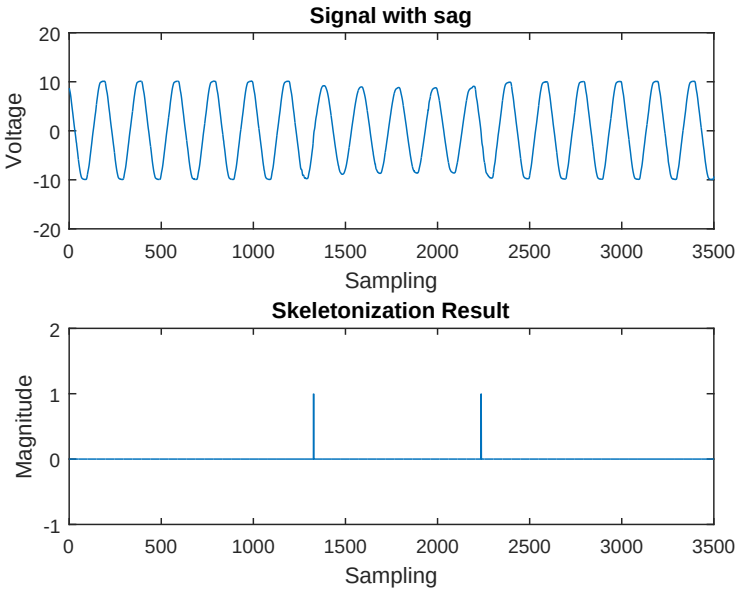

Figure 8.7: Skeletonization detection for sag at 80-71% normal using dataset D01

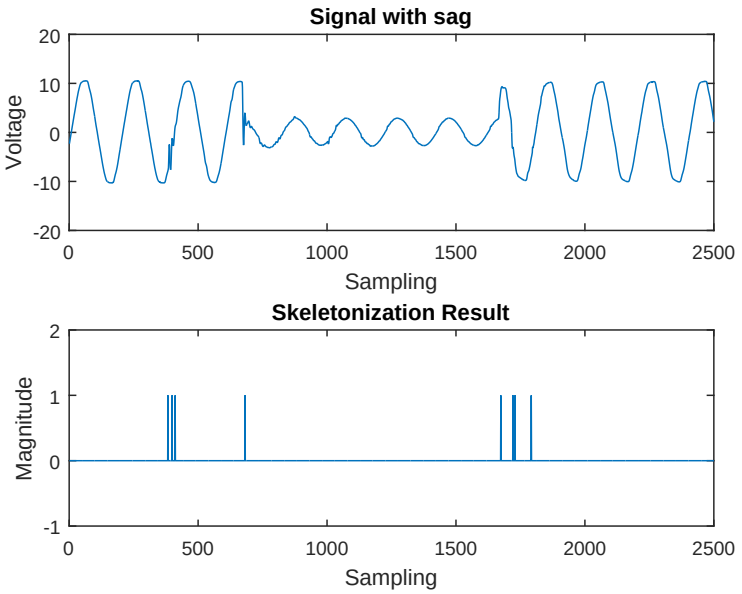

Figure 8.8: Skeletonization detection for sag at 30-21% normal using dataset D02

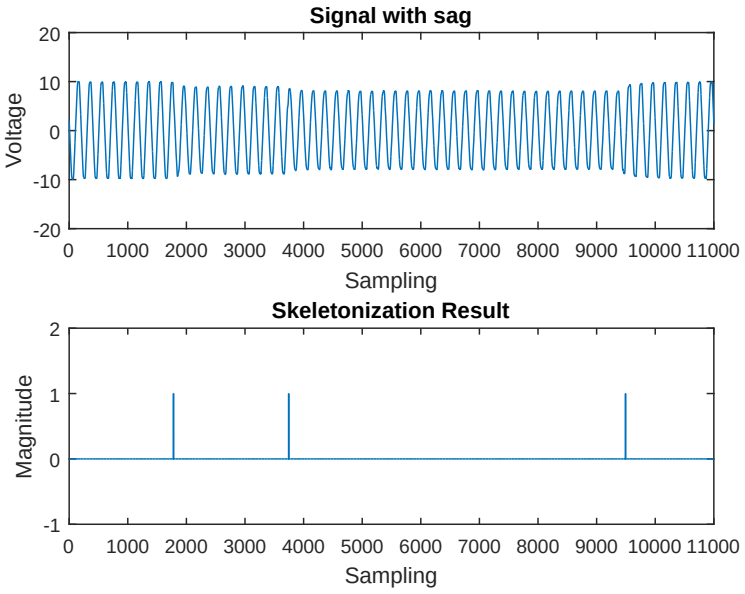

Figure 8.9: Skeletonization detection for sag at different value (80-71%) using dataset D03

In Figure 8.7 the sag with value 80% of normal voltage is successfully detected using this method as well as the sag on Figure 8.8 but with the additional result of the detection of the other disturbance. The variation of voltage sag can be seen in Figure 8.9 where the detection result shows the decrease of voltage about 10% below the normal value followed by about 20% of the normal values.

Results for swell and interruption can be seen in Figure 8.10 and 8.11.

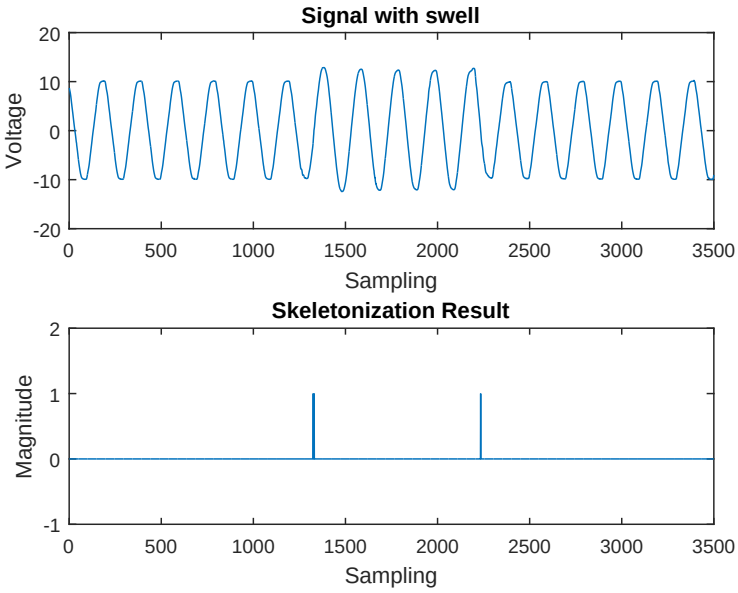

Figure 8.10: Skeletonization detection for swell at 40% above the normal value using dataset L11

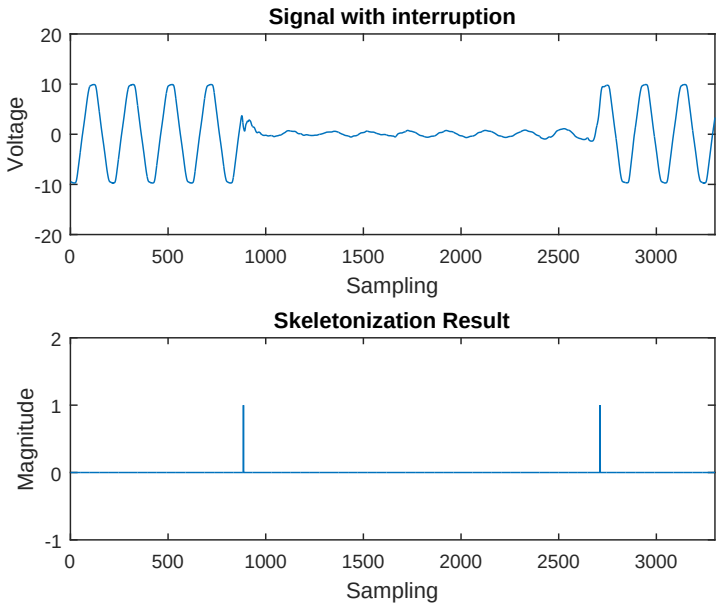

Figure 8.11: Skeletonization detection for interruption using dataset L21

8.2.2 Signal/Image Conversion

Using the same data from theprevious section, these dataset were analysed at different sampling frequency. This mean that the structuring element needs to modified to make it capable of handling the signal.

The results of the signal to image conversion (SIC) method in detection of disturbances can be seen in Figure 8.12 to 8.15 for two sags, swell and interruption respectively. In Figure 8.12 and 8.13, the results show that sag was successfully detected by the SIC method. These figures are also showing another location result of disturbances. This happens due to another disturbances or noise in the signal existing such as transient or harmonics.

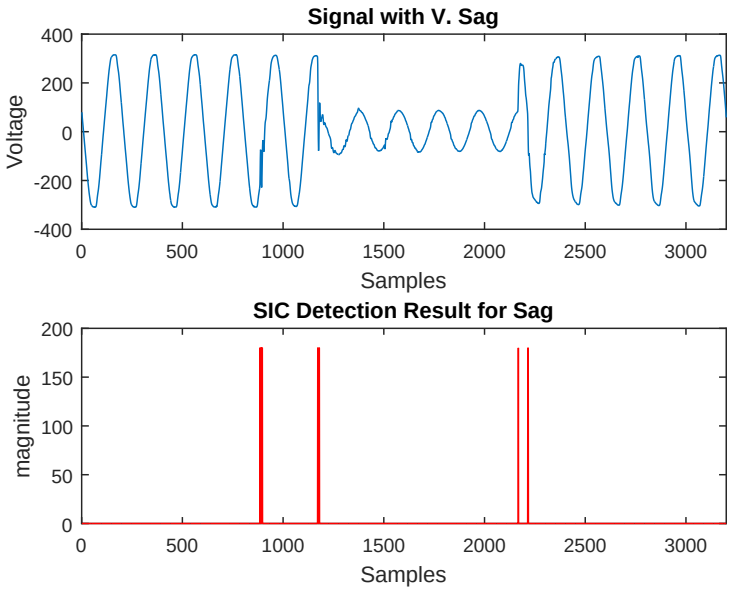

Figure 8.12: SIC detection for sag at 30-21% normal value using dataset D04

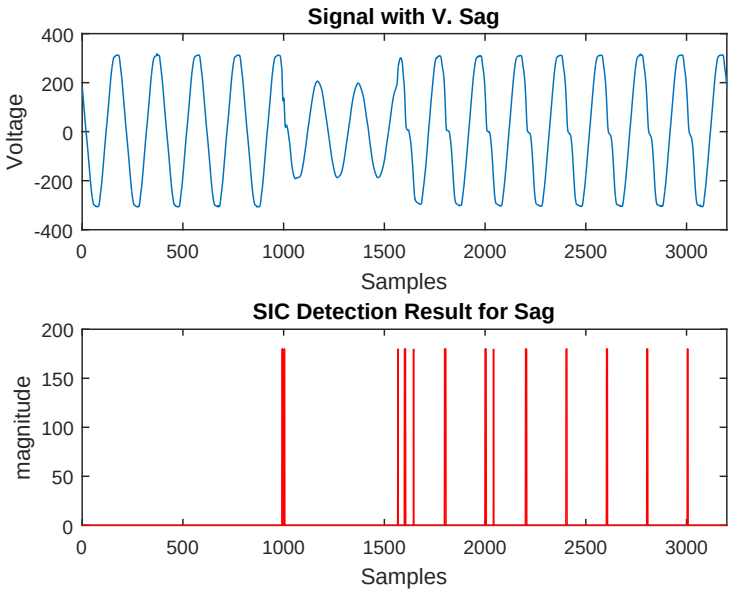

Figure 8.13: SIC detection for sag at 60-51% normal value using dataset D05

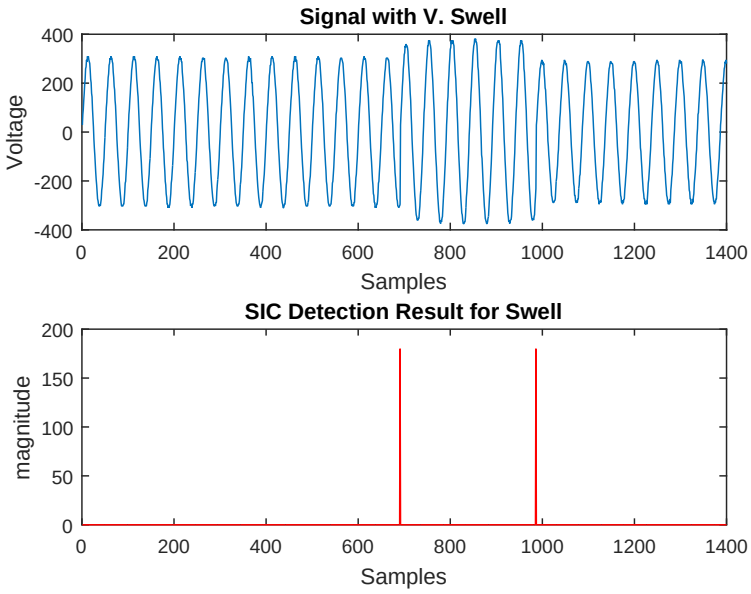

Figure 8.14: SIC detection for interruption using dataset L11

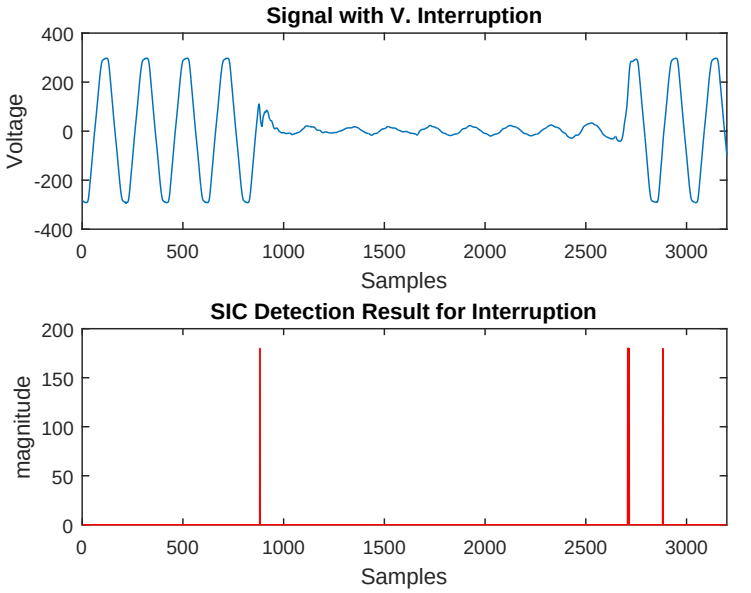

Figure 8.15: SIC detection for interruption using dataset L21

8.2.3 HMMG

Evaluation has also been undertaken using the HMMG method for sag, swell and interruption. The same signal with disturbances that have been used for the Skeletonization and the SIC methods were also used in the evaluation of this method. as The results can be seen in Figures 8.16 to 8.19 for sag, swell and interruption respectively.

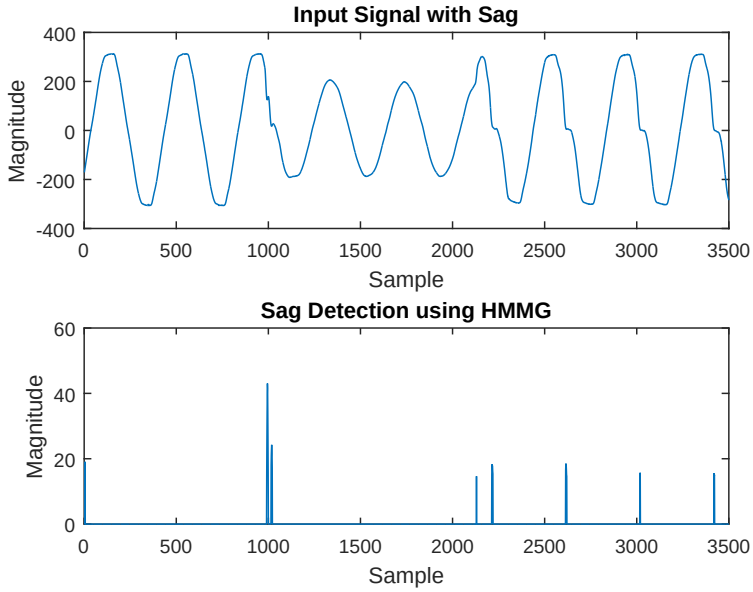

Figure 8.16: HMMG detection for sag at 60% normal value using dataset D05

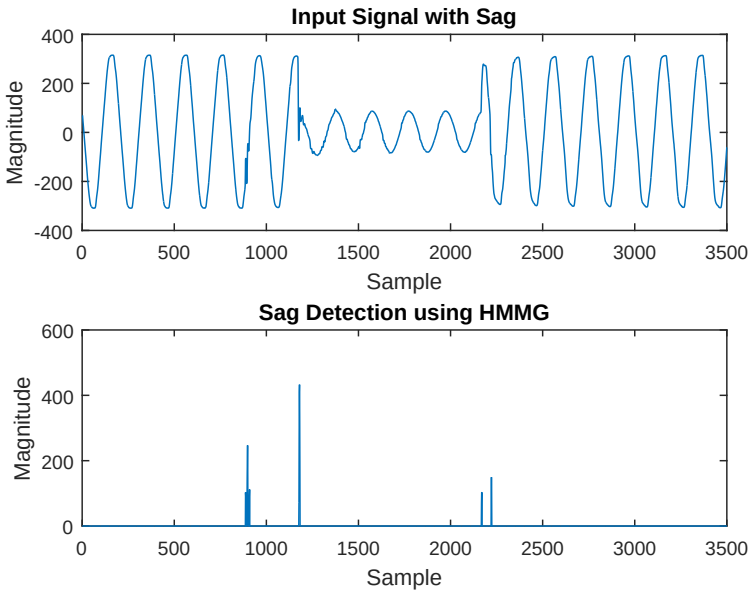

Figure 8.17: HMMG detection for sag at 30% normal value using dataset D04

Data sag for Figures 8.16 and 8.17 are from IEEE DataPort with sampling frequency at 10kHz. For this disturbance, HMMG is able to detect the time location of disturbances. Some points were also detected as different type of disturbances.

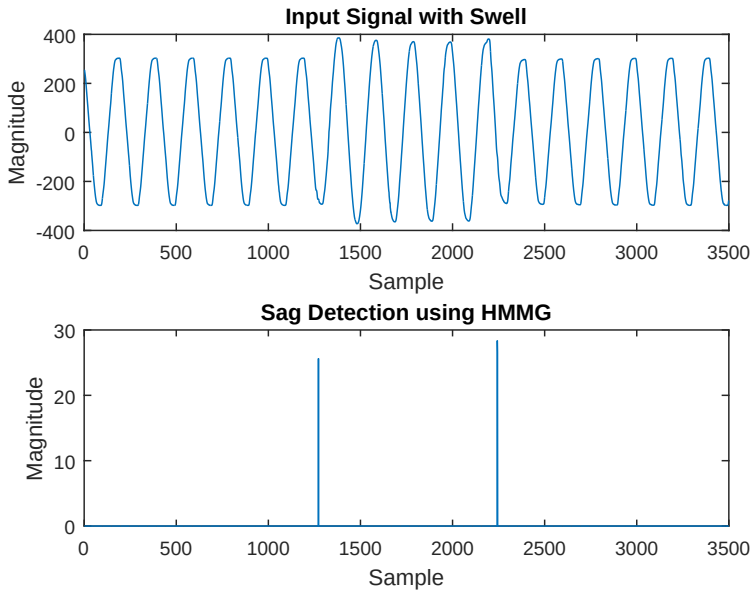

Figure 8.18: HMMG detection for swell using dataset D02

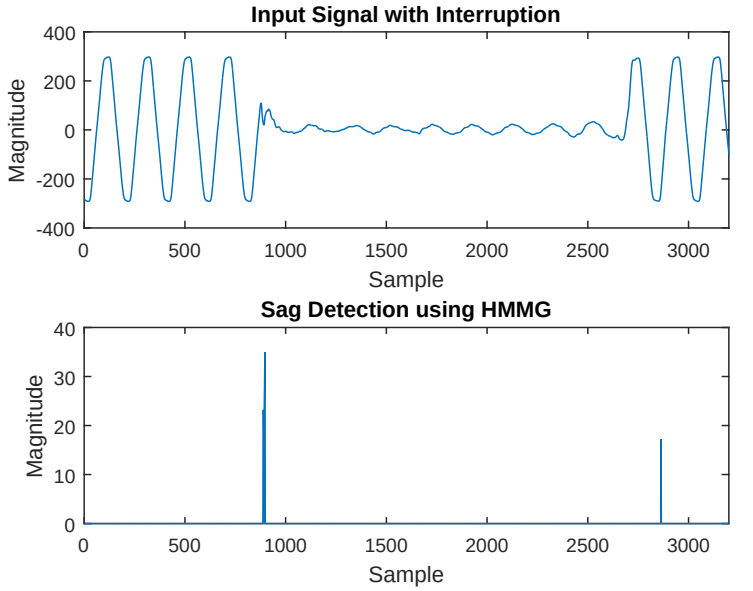

Figure 8.19: HMMG detection for interruption using dataset D04

Similar to other two methods (Skeletonization and SIC), the results of the evaluation show some points of other disturbances, especially for sag and swell detection. For inter-

ruption, there were some unsuccessful detection compared to the other strategies.

Another test has been conducted for sag, swell and interruption that were collected from the lab where the sampling frequency was 2.5kHz (Figures 8.20 - 8.22). The HMMG detection results for the sag at 76% of the normal signal can be seen in Figure 8.20.

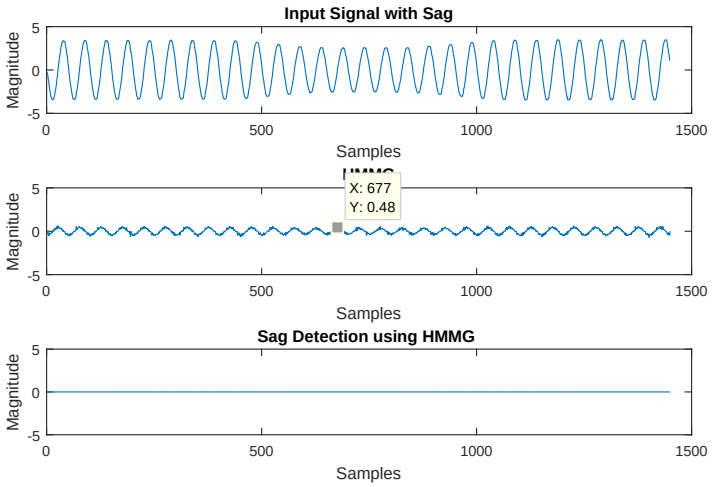

Figure 8.20: HMMG detection for sag at 76% normal value using dataset L01

Figures 8.20 shows that the HMMG was unsuccessful in detecting this sag because the variation of the signal is low. In addition, the sampling frequency was low causing the HMMG could not extract the feature of this signal correctly.

The HMMG was successful in detecting the swell in a signal as shown in Figure 8.21. However, even though the HMMG can detect the start point of interruption as shown in Figure 8.22, this method has a fault in detecting the end point of this disturbance. This is because the variation of the signal is too small and as a result, it is not enough information for HMMG to detect as a disturbance.

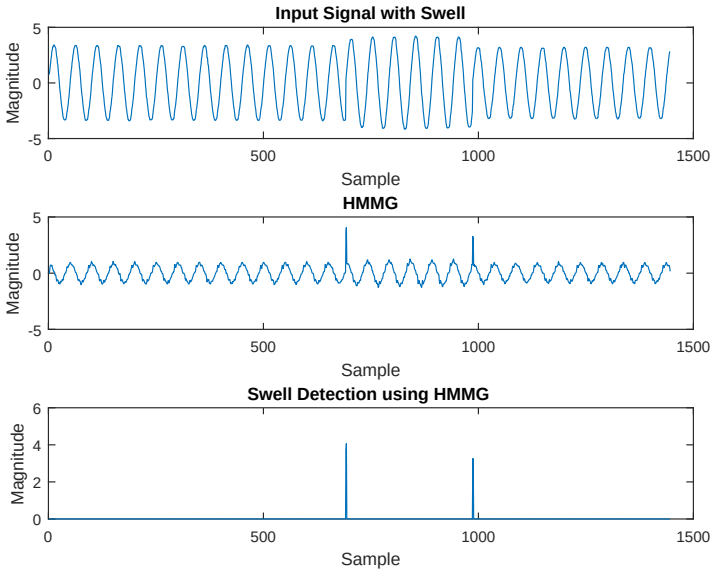

Figure 8.21: HMMG detection for swell which is the data from lab. using dataset L11

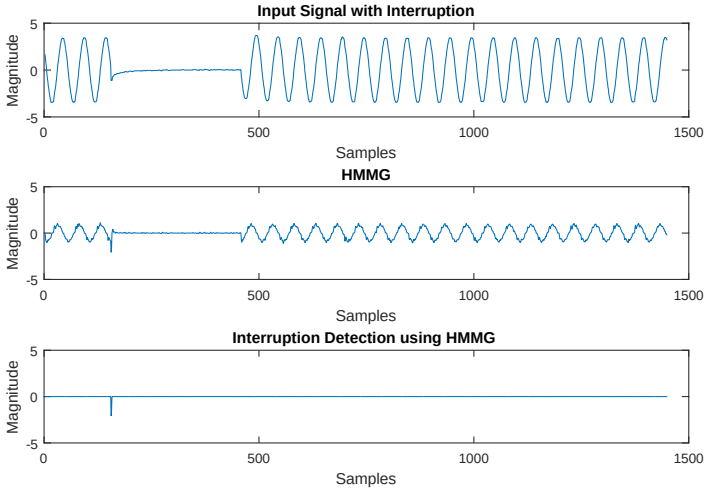

Figure 8.22: HMMG detection for interruption which is the data from lab. using dataset L21

The HMMG also has been checked for transient disturbances. A dataset of transient has

been acquired from the laboratory using the second experiment as shown in Figure 8.4. The number of datasets was 100 with 2500 samples for each data. The sampling frequency was 25kHz or 500 samples per cycle. The results of the HMMG in transient detection can be seen in Figures 8.23 to 8.26 and Table 8.2.

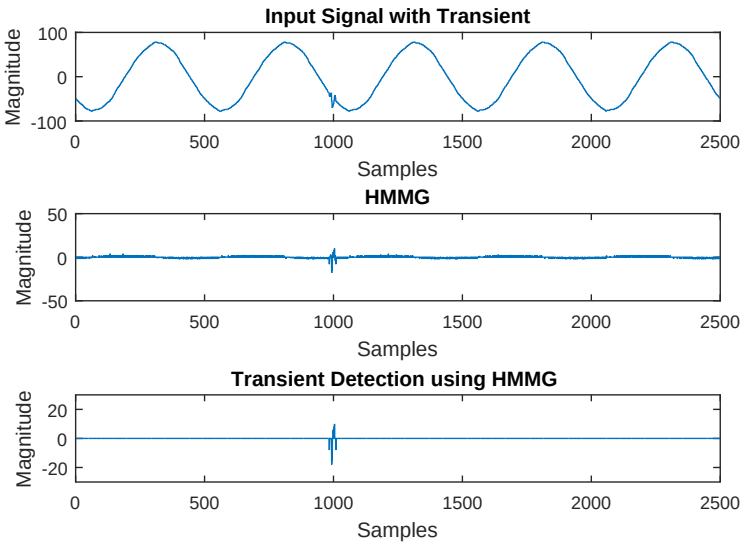

Figure 8.23: HMMG detection for transient using dataset T01

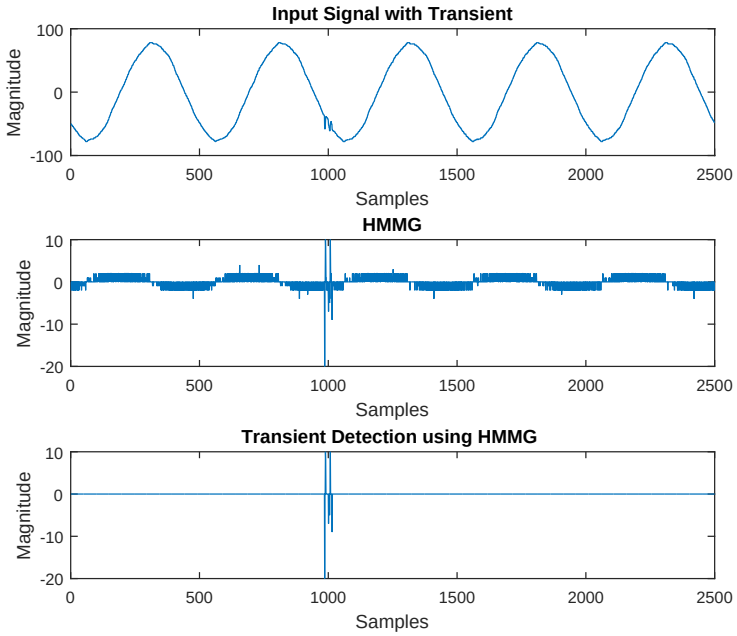

Figure 8.24: Result of HMMG detection for transient using dataset T02

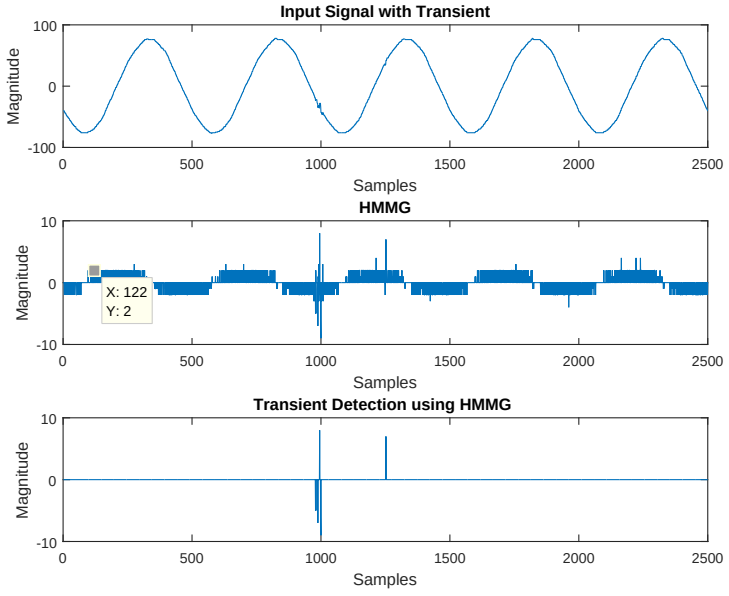

Figure 8.25: HMMG detection for transient with other noise using dataset T03

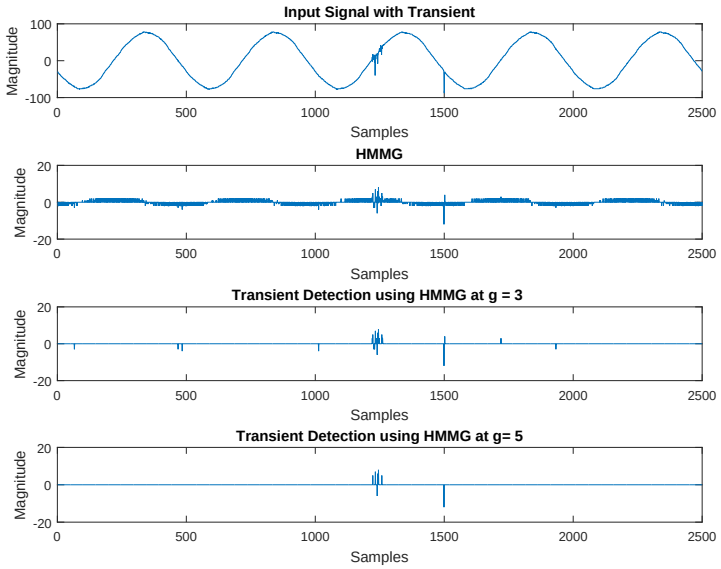

Figure 8.26: HMMG detection for transient and notching using dataset T04

In Figure 8.26, HMMG can detect not only the transient but also the notching that exists in the signal. The detection used 2 different values of structuring element g at 3 and 5. For the g= 3, using Equation (5.1.13) the thresholding value became 2.0207 resulting in some detection of the noise in the signal. In this case, the transient and notching can be detected correctly. Changing g to 5 and making the thresholding value became 4.0414 makes the results of the detection more clear, but some feature were eliminated like the crest in the notching and the trough in the transient.

Figure 8.27 shows the detection results of notching using g = 3 and 5. In this case, a better result was reached when g was 5 while a lot of noise in the signal was detected by the HMMG when g was 3. So, it is crucial to choose the value of the structuring element correctly to get the optimum result based on the maximum value and sampling frequency of the signal.

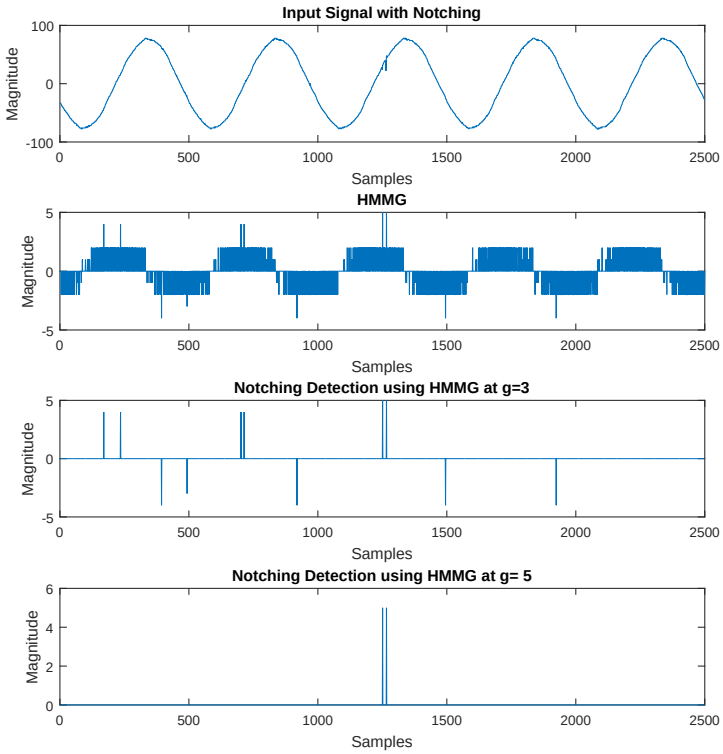

Figure 8.27: HMMG detection for notching with different value of g

Table 8.2: HMMG detection result using data transient from lab.

Type of Disturbance	Number of samples	Accurate detection	Inacurate detection	Percentage of accuracy
Transient	100	98	2	98 %

The HMMG method has good results for detecting transients in the signal with accuracy at 98%. This means that 98 out of 100 data of the transients can be detected accurately using HMMG.

8.2.4 Results Comparison

The comparison results of the simulation between the three method is presented in Table 8.3.

Table 8.3: Percentage of successful detection for the three different methods

No	Type of Disturbances	Skeletonization	SIC	HMMG
1	Sag	80%	80%	70%
2	Swell	90%	90%	90%
3	Interruption	75%	70%	60%

Note: **SIC** = Signal to Image Conversion

Table 8.3 shows that sag, swell and interruption can be detected using skeletonization, SIC, and HMMG. For sag detection, HMMG scored slightly lower than the two other methods with only 70% success compare to 80%. These three methods have the same result with 90% success in detecting the swell. Skeletonization has better results for detecting the interruption in the signal when compared with the other two methods. It is clearly seen that all three methods need some improvement in detecting voltage interruption especially to detect the end point of the disturbance.

Processing time tests have also been undertaken for the proposed methods. The duration of the sample for the test was 1280 samples and also every quarter cycle for HMMG. A morphological filter was used for all methods as a filter in this test. The results can be seen in Table 8.4.

Table 8.4: Processing time of different methods

Methods	Filtering Time	Processing Time	Total Time
Skeletonization	4.6 ms	5.10 ms	9.7 ms
Morph. Edge Detection	4.6 ms	2.90 ms	7.5 ms
SIC	4.6 ms	4.50 ms	9.10 ms
SIC - 1/32 cycle	0.32 ms	0.14 ms	0.46 ms
MMG	4.6 ms	31.83 ms	36.46 ms
HMMG	4.6 ms	10.03 ms	14.63 ms
HMMG - quarter cycle	0.92 ms	0.25 ms	1.17 ms

The test results in Table 8.4 show that skeletonization needs 2.20ms to process the signal after morphology edge detection. SIC has a good response for processing the signal every $\frac{1}{32}$ cycle with 0.46ms while it needs 9.10ms for completing all of the 1280 samples. HMMG is faster than MMG for full processing 128 samples while it only needs 1.17ms for processing every 100 samples or $\frac{1}{4}$ cycle of the input signal.

8.3 Summary

Three novel strategies have been developed to detect power quality disturbance in the power system. These strategies were applied in simulation using real dataset and a laboratory generated dataset. The results show that all of these methods successful detect the disturbances. On average, the skeletonization method can detect 78.3% of disturbances while the HMMG method only detected 76.67%. On the other hand, The signal/image conversion with a small data window found 70% of disturbances on average.

Processing time tests show that SIC is the fastest result in processing the input signal (0.14ms). HMMG also has good results for disturbances detection (1.17 ms). One of the

advantage of HMMG is the the input signal will be processed directly by the HMMG after filtering process. Different from the HMMG, the SIC converts the input signal to image matrix and makes a rounding process. This process may remove some essential features of the signal.

Chapter 9

Conclusion and Recommendations for Future Work

9.1 Conclusion

The thesis has described some methods that have been developed for detecting power quality disturbances detection in the power system based on mathematical morphology. Mathematical morphology was used for all of the methods because it requires only simple calculation and thus has a fast response. As a result, it will reduce the complexity of the calculation process and there is no need for dedicated hardware. Methods for power quality detection have been developed using: 1) Morphology gradient and then the result plotting to 3D, 2) combination of edge detection and skeletonization, 3) signal to image matrix conversion and control chart detection, 4) short data windows, 5) Half Multi resolution Morphology Gradient.

Morphology Gradient was used for an initial detection of the disturbances, then the top-hat transform was applied to detect the time location of power quality disturbances especially for voltage swell, sag, and interruption. The result of the filtered signal was then plotted to 3D. By using this method, the location of the disturbances was able to be identified with the different colors and different shapes as pattern recognition.

Skeletonization has the capability to detect the noise in the system. The noise location in the system was identified as a black color on 3D plotting. The higher the noise, the more lines will be produced by the skeletoization process, resulting in the high density of the black color. Skeletonization identified the noise when the signal to noise ratio (SNR) of the evaluated signal was less than 50dB. This can also be identified as pattern recognition by plotting the results in 3D. Skeletonization can also be combined with morphology edge detection to detect the accurate time location of disturbances in the system for both noise-free signal and signals with noise. Using this proposed method, voltage swell and sag can be detected accurately without error while there was only a small error in the voltage interruption detection. With the average error for this proposed method being only 0.1667 of sampling period, the overall result has reduced the error significantly, which was by about 33% compared to the result of morphology edge detection strategy.

In the signal to image matrix method, the input signal was converted to an image matrix. As an image, methods that are used in image processing could be applied to this matrix. In this process, some steps based on mathematical morphology were developed such as, points addition, morphology boundary, deleting axis points, and adding lost points. This method successfully detected the time location of the disturbances as violation points in the control chart. This method was then applied to short data samples of the signal (4 samples) to makes the size of the window becomes small (1/32 cycle). Simulation results for this strategy show that starting point and ending point of disturbances can be detected accurately for both sag and swell, but there was one sampling period error for detecting the end point of the interruption. This strategy has a better result compared to the Wavelet or Morphology edge detection strategy. In order to get the best results, it is essential to choose the parameter value and type of structuring element accurately based on the type of disturbance.

Half Multi-resolution Morphology Gradient (HMMG) based on MMG is presented in this thesis for detecting the power quality disturbances. This method uses only half the processes of MMG, and the level of a is set at 1, so the number of calculation was reduced, as a result the processing time of the strategy was reduced. As with the MMG method, the HMMG approach has the capability to detect the polarity of the disturbances. So, detection

using this strategy generates better results. The classification strategy for all disturbances was undertaken calculating the RMS value of the signal during the disturbances especially for sag, swell and momentary interruption. Transients, notching, and flicker can be classified by using an FFT to find the number of crests and troughs, and also their frequency. An appropriate filter was needed for real data simulations, where some noise exists in the signal.

A new strategy in estimating a single frequency of the signal in the time domain was also presented in this thesis. Using top-hat and bottom-hat transforms, this proposed method shows a good estimation for noise-free signal and also the signal with maximum SNR value at 30dB. Although the accuracy of this method decreased when analysing signals with a SNR less than 30dB, it is still good as an alternative method for frequency estimation. By using MM in its process, the complexity of calculation can be reduced.

An identification and classification of disturbances in power systems using probabilistic neural networks was also presented. This strategy used HMMG for disturbance detection as the input for the PNN. The results show a good classification for 9 type of disturbances and 1 normal signal.

Three novel strategies for the detection of PQ disturbances have been developed and were evaluated by using the real data of three type of disturbances. These disturbances were acquired from laboratory and also from IEEE Dataport. The results show all methods have good results but some errors found in the detection of disturbances due to the dataset contain more than one type of disturbances. It is also because the signal has a very low variation at the low sampling frequency, making it unsuccessful in the process of extracting the feature of the disturbance.

The advantages and drawbacks of all three novel strategies in this research can be seen in Table 9.1.

Table 9.1: Advantages and drawbacks between the three novel methods

No	Methods	Advantages	Drawbacks
1	**Skeletonization** - In 3D - Combination with Morphology Edge Detection	For pattern recognition in detection the disturbances and noise It has good results in disturbances detection,so it will be suitable for monitoring of assessment of PQ disturbances	It has a high processing time, so it is not suitable for real time application of PQ disturbances detection
2	**SIC** - with Control Chart - Small data window	For monitoring PQ disturbances with faster detection compared to Skeletonization Only needs a short sample data, so it has a fast processing time, so it is good for real time detection	Rounding process in signal to image matrix conversion may delete some essential features of the signal
3	**HMMG**	This method can be used for monitoring PQ disturbances and also by combined with PNN for detection and classification the disturbances. Due to this method has a high speed in processing the signal, it can be used for real time application.	It has a problem in detecting end point of voltage interruption especially when the first point after interruption has a small different compared to the end point of the disturbance.

9.2 Recommendations for Future Work

There are still some options for future improvement for the strategies based on Mathematical Morphology that have been presented in this thesis.

The first task would be a real time application of detection of power quality disturbances using short data windows. This should be based on the hardware system that would be used. The number of sample in real time processing should be matched as a real-time system so there would be no delay time in the processing of this strategy. The higher speed of the processor of the hardware will guarantee the processing time of this method in handling a short sample of the signal. On the other hand, if the hardware had not enough speed to

process a short sample, the number of the sample could be increased such as from 4 to 8, 16 or higher. Choosing an appropriate structuring element for both its type and its size would be an important step in this future work.

Another future area of research is to develop a new structuring element or a new strategy as an adaptive structuring element. This would be a great challenge since this topic still is an open area of research.

Finally, the frequency estimation strategy would be a good research area for finding an alternative method of calculating the frequency of the signal. It includes an improvement in estimating the frequencies of the signal with SNR lower than 30dB and lowering the errors for the higher frequency.

References

[1] M. F. McGranaghan, D. R. Mueller, and M. J. Samotyj, "Voltage sags in industrial systems," *IEEE Transactions on Industry Applications*, vol. 29, no. 2, pp. 397–403, Mar 1993.

[2] W. A. Elmore, *Protective Relaying Theory and Applications*. New York: ABB Power T & D Company Inc., 2003.

[3] J. Perez, "A guide to digital fault recording event analysis," in *2010 63rd Annual Conference for Protective Relay Engineers*, March 2010, pp. 1–17.

[4] *SIMEAS R Digital Fault Recorder with Power Quality (PQ) or Phasor Measurement Unit (PMU), Power Distribution Division Siemens, 2008*.

[5] *SIMEAS Q80 Power Quality Recorder, Power Distribution Division Siemens, 2009*.

[6] R. Bernardes and F. Ayello, "Pqms - power quality monitoring system: Improve power systems through ieds," in *CIRED 2009 - 20th International Conference and Exhibition on Electricity Distribution - Part 1*, June 2009, pp. 1–4.

[7] A. Shirkovets, A. Telegin, V. Senchenko, and V. Kirichenko, "High-frequency recording system for transient processes in 6-110 kv electrical networks," in *2014 Electric Power Quality and Supply Reliability Conference (PQ)*, June 2014, pp. 69–73.

[8] L. Liu and Z. Zeng, "The detection and location of power quality disturbances based on orthogonal wavelet packet transform," in *Electric Utility Deregulation and Re-*

structuring and Power Technologies, 2008. DRPT 2008. Third International Conference on, 2008, pp. 1831–1835.

[9] T. Y. Ji, Q. H. Wu, L. Jiang, and W. H. Tang, "Disturbance detection, location and classification in phase space," *Generation, Transmission Distribution, IET*, vol. 5, no. 2, pp. 257–265, 2011.

[10] Q. Yinglin and T. Lijun, "Pattern recognition and time location of power quality disturbances using tt-transform," in *Intelligent System Design and Engineering Application (ISDEA), 2010 International Conference on*, vol. 2, 2010, pp. 53–56.

[11] L. Gengyin, Z. Ming, and Z. Zhiyuan, "Research on power quality disturbance automatic recognition and location," in *IEEE Power Engineering Society General Meeting, 2003*, vol. 2, 2003, pp. –691 Vol. 2.

[12] M. H. Sedaaghi, "Morphological filtering in signal/image processing," Ph.D. dissertation, Liverpool University, 1998.

[13] H. Runhong, O. Sen, and S. Yili, "A precise location method of power quality disturbances based on morphological edge detection," in *2012 Asia-Pacific Power and Energy Engineering Conference (APPEEC)*, 2012, pp. 1–5.

[14] S. Gautam and S. Brahma, "Detection of high impedance fault in power distribution systems using mathematical morphology," *IEEE Transactions on Power Systems*, vol. 28, no. 2, pp. 1226–1234, May 2013.

[15] T. Ji, "Advanced mathematical morphology and its applications to signal processing," Ph.D. dissertation, Liverpool University, 2009.

[16] T. Y. Ji, Z. Lu, W. H. Tang, and Q. Wu, "Disturbance detection in the phase space through gk clustering," in *DRPT 2008. Third International Conference on Electric Utility Deregulation and Restructuring and Power Technologies, 2008*, April 2008, pp. 2328–2332.

[17] C. Xue, L. Hui-jin, Z. Quan-ming, Y. Li-ming, and L. Qing-fen, "Power quality disturbances detection and location using mathematical morphology and complex wavelet transformation," in *Industrial Electronics and Applications, 2008. ICIEA 2008. 3rd IEEE Conference on*, 2008, pp. 2263–2268.

[18] P. Wang and S. Liu, "Application of mathematical morphological operator in power fault signal detection," in *2011 International Conference on Electrical and Control Engineering (ICECE)*, 2011, pp. 1000–1003.

[19] L. L. Zhang, T. Y. Ji, M. S. Li, Q. H. Wu, L. Jiang, and J. P. Zhan, "Disturbance identification based on mathematical morphology and radial coordinate visualization," in *2013 4th IEEE/PES Innovative Smart Grid Technologies Europe (ISGT EUROPE)*, Oct 2013, pp. 1–5.

[20] Z. Ji, Q. Zeng, J. Liao, and Q. H. Wu, "A novel mathematical morphology filter for the accurate fault location in power transmission lines," in *TENCON 2009 - 2009 IEEE Region 10 Conference*, 2009, pp. 1–6.

[21] D. Zhang, "Transient protective relaying based on wavelet analysis and mathematical morphology," Ph.D. dissertation, Liverpool University, 2002.

[22] J. Zhu, T. Y. Ji, M. S. Li, Q. H. Wu, and J. S. Smith, "Detection and classification of power disturbances using mathematical morphology with trapezoid structuring elements and signal envelopes," in *IEEE PES Innovative Smart Grid Technologies, Europe*, Oct 2014, pp. 1–6.

[23] J. Serra and P.Soille, *Mathematical Morphology and Its Applications to Image Processing*. Kluwer Academic Publishers, 1998.

[24] L. V. J.Goutsias and D. S. Bloomberg, Eds., *Mathematical Morphology and Its Applications to Image and Signal Processing*. Kluwer Academic Publishers: Marcel Dekker,INC, 2000.

[25] T. Ji, "Advanced mathematical morphology and its applications to signal processing," Ph.D. dissertation, The University of Liverpool, Department of Electrical Engineering and Electronics, 2009.

[26] A. McAndrew, *Introduction to Digital Image Processing with MATLAB*. Course Technology Publishers, 2004.

[27] I. Peters, R. A., "A new algorithm for image noise reduction using mathematical morphology," *Image Processing, IEEE Transactions on*, vol. 4, no. 5, pp. 554–568, 1995.

[28] T. Veerakumar, S. Esakkirajan, and I. Vennila, "An efficient approach to remove random valued impulse noise in images," in *Recent Trends In Information Technology (ICRTIT), 2012 International Conference on*, 2012, pp. 49–53.

[29] D. Ze-Feng, Y. Zhou-ping, and X. You-lun, "High probability impulse noise-removing algorithm based on mathematical morphology," *Signal Processing Letters, IEEE*, vol. 14, no. 1, pp. 31–34, 2007.

[30] I. S. Yassine, S. Belfkih, S. Najah, and H. Zenkouar, "A new method for texture image segmentation," in *I/V Communications and Mobile Network (ISVC), 2010 5th International Symposium on*, 2010, pp. 1–4.

[31] C. Jia-xin and L. Sen, "A medical image segmentation method based on watershed transform," in *Computer and Information Technology, 2005. CIT 2005. The Fifth International Conference on*, 2005, pp. 634–638.

[32] G. K. Matsopoulos and S. Marshall, "Medical applications of mathematical morphology," in *Morphological and Nonlinear Image Processing Techniques, IEE Colloquium on*, 1993, pp. 8/1–8/4.

[33] R. Garnavi, A. Baraani-Dastjerdi, H. A. Moghaddam, M. Giti, and A. A. Rad, "A new segmentation method for lung hrct images," in *Digital Image Computing: Techniques and Applications, 2005. DICTA'05. Proceedings 2005*, 2005, pp. 52–52.

[34] W. Minjin, "Fuzzy morphology and image analysis," in *Pattern Recognition, 1988., 9th International Conference on*, 1988, pp. 453–455 vol.1.

[35] M. C. Maccarone, M. Tripiciano, and V. Di Gesu, "Fuzzy mathematical morphology to analyse astronomical images," in *Pattern Recognition, 1992. Vol.III. Conference C: Image, Speech and Signal Analysis, Proceedings., 11th IAPR International Conference on*, 1992, pp. 248–251.

[36] J. Oh and L. F. Chaparro, "Adaptive fuzzy morphological filtering of images," in *Acoustics, Speech and Signal Processing, 1998. Proceedings of the 1998 IEEE International Conference on*, vol. 5, 1998, pp. 2901–2904 vol.5.

[37] T. Kikuchi, "Characteristic extraction from an ambiguous image using fuzzy mathematical morphology with adaptive structuring elements," in *Fuzzy Systems, 2001. The 10th IEEE International Conference on*, vol. 1, 2001, pp. 228–231.

[38] L. Chunzhi and C. Jiajun, "Mathematical morphological filter and its application in removing noises in vibration signal," in *Electronic Measurement and Instruments, 2007. ICEMI '07. 8th International Conference on*, 2007, pp. 4–101–4–104.

[39] Z. Ji, Q. Zeng, J. Liao, and Q. H. Wu, "A novel mathematical morphology filter for the accurate fault location in power transmission lines," in *TENCON 2009 - 2009 IEEE Region 10 Conference*, 2009, pp. 1–6.

[40] P. Wang and S. Liu, "Application of mathematical morphological operator in power fault signal detection," in *Electrical and Control Engineering (ICECE), 2011 International Conference on*, 2011, pp. 1000–1003.

[41] E. C. Pedrino, J. H. Saito, and V. O. Roda, "Architecture for binary mathematical morphology reconfigurable by genetic programming," in *2010 VI Southern Programmable Logic Conference (SPL)*, March 2010, pp. 93–98.

[42] S. R. S. R. M. Haralick and X. Zhuang, "Image analysis using mathematical mor-

phology," *IEEE Trans. Pattern Anal. Machine Intell. PAMI-9*, no. 4, pp. 532–550, 1987.

[43] R. M. Haralick and L. G. Shapiro, *Computer and Robot Vision*. Addison-Wesley, 1993.

[44] Q. H. Wu, Z. Lu, and T. Y. Ji, *Protective Relaying of Power Systems Using Mathematical Morphology*, 1st ed. Springer Publishing Company, Incorporated, 2009.

[45] L. Zhang, J. Xu, J. Yang, D. Yang, and D. Wang, "Multiscale morphology analysis and its application to fault diagnosis," *Mechanical Systems and Signal Processing*, vol. 22, no. 3, pp. 597 – 610, 2008. [Online]. Available: http://www.sciencedirect.com/science/article/pii/S0888327007001926

[46] Y. Zhang, T. Y. Ji, M. S. Li, and Q. H. Wu, "Identification of power disturbances using generalized morphological open-closing and close-opening undecimated wavelet," *IEEE Transactions on Industrial Electronics*, vol. 63, no. 4, pp. 2330–2339, April 2016.

[47] Y. Zhang, T. Ji, M. Li, and Q. Wu, "Detection and classification of low-frequency power disturbances using a morphological max-lifting scheme," in *Power and Energy Engineering Conference (APPEEC), 2013 IEEE PES Asia-Pacific*, Dec 2013, pp. 1–5.

[48] L. Zhang, M. Li, T. Ji, Q. Wu, L. Jiang, and J. Zhan, "Morphology singular entropy-based phase selector using short data window for transmission lines," *Power Delivery, IEEE Transactions on*, vol. 29, no. 5, pp. 2162–2171, Oct 2014.

[49] S. Gautam and S. Brahma, "Detection of high impedance fault in power distribution systems using mathematical morphology," *Power Systems, IEEE Transactions on*, vol. 28, no. 2, pp. 1226–1234, May 2013.

[50] Z. Ji, Q. Zeng, J. Liao, and Q. Wu, "A novel mathematical morphology filter for the

accurate fault location in power transmission lines," in *TENCON 2009 - 2009 IEEE Region 10 Conference*, Jan 2009, pp. 1–6.

[51] C. Xue, L. Hui-jin, Z. Quan-ming, Y. Li-ming, and L. Qing-fen, "Power quality disturbances detection and location using mathematical morphology and complex wavelet transformation," in *Industrial Electronics and Applications, 2008. ICIEA 2008. 3rd IEEE Conference on*, June 2008, pp. 2263–2268.

[52] R. C. G. R. E. W. S. L. Eddins, *Digital Image Processing With Matlab*. Gatesmark Publishing, 2009.

[53] S. R. Sternberg, "Grayscale morphology," *Comput. Vision Graph. Image Process.*, vol. 35, no. 3, pp. 333–355, Sep. 1986. [Online]. Available: http://dx.doi.org/10.1016/0734-189X(86)90004-6

[54] R. van den Boomgaard, "Mathematical morphology: Extensions towards computer vision." Ph.D. dissertation, The University of Amsterdam, 1992.

[55] O. Poisson, P. Rioual, and M. Meunier, "Detection and measurement of power quality disturbances using wavelet transform," *IEEE Transactions on Power Delivery*, vol. 15, no. 3, pp. 1039–1044, Jul 2000.

[56] P. K. Dash, B. K. Panigrahi, D. K. Sahoo, and G. Panda, "Power quality disturbance data compression, detection, and classification using integrated spline wavelet and s-transform," *IEEE Transactions on Power Delivery*, vol. 18, no. 2, pp. 595–600, April 2003.

[57] M. Karimi, H. Mokhtari, and M. R. Iravani, "Wavelet based on-line disturbance detection for power quality applications," *IEEE Transactions on Power Delivery*, vol. 15, no. 4, pp. 1212–1220, Oct 2000.

[58] J. Wang and C. Wang, "Detection of power quality disturbance based on binary wavelet transform," in *TENCON 2007 - 2007 IEEE Region 10 Conference*, Oct 2007, pp. 1–3.

[59] L. Liu and Z. Zeng, "The detection and location of power quality disturbances based on orthogonal wavelet packet transform," in *Electric Utility Deregulation and Restructuring and Power Technologies, 2008. DRPT 2008. Third International Conference on*, April 2008, pp. 1831–1835.

[60] "IEEE recommended practice for powering and grounding electronic equipment," *IEEE Std 1100-2005 (Revision of IEEE Std 1100-1999)*, pp. 1–703, May 2006.

[61] "IEEE recommended practice for monitoring electric power quality," *IEEE Std 1159-2009 (Revision of IEEE Std 1159-1995)*, pp. c1–81, June 2009.

[62] Z. Lu, D. R. Turner, Q. H. Wu, J. Fitch, and S. Mann, "Morphological transform for detection of power quality disturbances," in *Power System Technology, 2004. PowerCon 2004. 2004 International Conference on*, vol. 2, 2004, pp. 1644–1649 Vol.2.

[63] P. Soille, *Morphological Image Analysis: Principles and Applications*. New York: Springer-Verlag, 1999.

[64] "IEEE guide for voltage sag indices," *IEEE Std 1564-2014*, pp. 1–59, June 2014.

[65] "IEC standard for electromagnetic compatibility (emc) part 4-30: Testing and measurement techniques power quality measurement methods." *IEC 61000-4-30, 2003*, 2003.

[66] A. Baggini, *Handbook of Power Quality*. The Atrium, Southern Gate, Chichester, West Sussex PO19 8SQ, England: John Wiley & Sons Ltd, 15 April 2008.

[67] G. V. M. B. M. Barnes, *Practical Grounding, Bonding, Shielding and Surge Protection, 1st Edition*. Butterworth-Heinemann, 2004.

[68] F. Y. Shih, *Image processing and mathematical morphology fundamentals and applications*. FL, USA: CRC Press, Taylor & Francis Group, 2009.

[69] P. Swamidass, Ed., *Encyclopedia of Production and Manufacturing Management*. Kluwer Academic Publishers: Springer US, 2000.

[70] Y. Zhang, T. Y. Ji, M. S. Li, and Q. H. Wu, "Detection and classification of low-frequency power disturbances using a morphological max-lifting scheme," in *2013 IEEE PES Asia-Pacific Power and Energy Engineering Conference (APPEEC)*, Dec 2013, pp. 1–5.

[71] I. D. Saputra, J. S. Smith, and Q. H. Wu, "Combination of morphology edge detection and skeletonization in detecting time location of power disturbances," in *IEEE PES Innovative Smart Grid Technologies, Europe*, Oct 2014, pp. 1–5.

[72] Q. H. Wu, J. F. Zhang, and D. J. Zhang, "Ultra-high-speed directional protection of transmission lines using mathematical morphology," *Power Delivery, IEEE Transactions on*, vol. 18, no. 4, pp. 1127–1133, 2003.

[73] D. J. Zhang, Q. H. Wu, J. F. Zhang, and K. I. Nuttall, "Accurate fault location based on transients extraction using mathematical morphology," *Electronics Letters*, vol. 38, no. 24, pp. 1583–1585, Nov 2002.

[74] C. t. Nguyen and K. Srinivasan, "A new technique for rapid tracking of frequency deviations based on level crossings," *IEEE Transactions on Power Apparatus and Systems*, vol. PAS-103, no. 8, pp. 2230–2236, Aug 1984.

[75] M. M. Begovic, P. M. Djuric, S. Dunlap, and A. G. Phadke, "Frequency tracking in power networks in the presence of harmonics," *IEEE Transactions on Power Delivery*, vol. 8, no. 2, pp. 480–486, Apr 1993.

[76] S. Rai, D. Lalani, S. K. Nayak, T. Jacob, and P. Tripathy, "Estimation of low-frequency modes in power system using robust modified prony," *IET Generation, Transmission Distribution*, vol. 10, no. 6, pp. 1401–1409, 2016.

[77] S. R. Nam, S. H. Kang, L. M. Jing, S. H. Kang, and S. W. Min, "A novel method based on prony analysis for fundamental frequency estimation in power systems," in *IEEE 2013 Tencon - Spring*, April 2013, pp. 327–331.

[78] J. Li, S. Wang, and F. Wang, "Frequency estimation by correlation based two-dimensional prony-type method," in *International Conference on Neural Networks and Signal Processing, 2003. Proceedings of the 2003*, vol. 1, Dec 2003, pp. 681–685 Vol.1.

[79] T. Lobos and J. Rezmer, "Real-time determination of power system frequency," *IEEE Transactions on Instrumentation and Measurement*, vol. 46, no. 4, pp. 877–881, Aug 1997.

[80] M. S. Sachdev, H. C. Wood, and N. G. Johnson, "Kalman filtering applied to power system measurements for relaying," *IEEE Power Engineering Review*, vol. PER-5, no. 12, pp. 52–53, Dec 1985.

[81] A. G. Phadke, J. S. Thorp, and M. G. Adamiak, "A new measurement technique for tracking voltage phasors, local system frequency, and rate of change of frequency," *IEEE Transactions on Power Apparatus and Systems*, vol. PAS-102, no. 5, pp. 1025–1038, May 1983.

[82] J. V. Wijayakulasooriya, G. A. Putrus, and P. D. Minns, "Electric power quality disturbance classification using self-adapting artificial neural networks," *IEE Proceedings - Generation, Transmission and Distribution*, vol. 149, no. 1, pp. 98–101, Jan 2002.

[83] A. K. Ghosh and D. L. Lubkeman, "The classification of power system disturbance waveforms using a neural network approach," in *Proceedings of IEEE/PES Transmission and Distribution Conference*, Apr 1994, pp. 323–329.

[84] Z.-L. Gaing, "Wavelet-based neural network for power disturbance recognition and classification," *IEEE Transactions on Power Delivery*, vol. 19, no. 4, pp. 1560–1568, Oct 2004.

[85] J. F. Fernandes, F. B. Costa, and R. P. de Medeiros, "Power transformer disturbance classification based on the wavelet transform and artificial neural networks," in *2016*

International Joint Conference on Neural Networks (IJCNN), July 2016, pp. 640–646.

[86] S. S., K. U. Rao, and S. Jade, "Detection and classification of pq disturbances in the supply to induction motor using wavelet transform and feedforward neural network," in *2015 IEEE International Conference on Electrical, Computer and Communication Technologies (ICECCT)*, March 2015, pp. 1–5.

[87] N. R. Devi, D. V. S. S. S. Sarma, and P. V. R. Rao, "Diagnosis and classification of stator winding insulation faults on a three-phase induction motor using wavelet and mnn," *IEEE Transactions on Dielectrics and Electrical Insulation*, vol. 23, no. 5, pp. 2543–2555, October 2016.

[88] S. Khokhar, A. A. M. Zin, A. S. Mokhtar, M. A. Bhayo, and A. Naderipour, "Automatic classification of single and hybrid power quality disturbances using wavelet transform and modular probabilistic neural network," in *2015 IEEE Conference on Energy Conversion (CENCON)*, Oct 2015, pp. 457–462.

[89] S. Mishra, C. N. Bhende, and B. K. Panigrahi, "Detection and classification of power quality disturbances using s-transform and probabilistic neural network," *IEEE Transactions on Power Delivery*, vol. 23, no. 1, pp. 280–287, Jan 2008.

[90] R. Kumar, B. Singh, D. T. Shahani, A. Chandra, and K. Al-Haddad, "Recognition of power-quality disturbances using s-transform-based ann classifier and rule-based decision tree," *IEEE Transactions on Industry Applications*, vol. 51, no. 2, pp. 1249–1258, March 2015.

[91] S. Alshahrani, M. Abbod, B. Alamri, and G. Taylor, "Evaluation and classification of power quality disturbances based on discrete wavelet transform and artificial neural networks," in *2015 50th International Universities Power Engineering Conference (UPEC)*, Sept 2015, pp. 1–5.

[92] L. C. Saikia, S. M. Borah, and S. Pait, "Detection and classification of power quality disturbances using wavelet transform, fuzzy logic and neural network," in *2010 Annual IEEE India Conference (INDICON)*, Dec 2010, pp. 1–5.

[93] Z. M. Chen, M. S. Li, T. Y. Ji, and Q. H. Wu, "Detection and classification of power quality disturbances in time domain using probabilistic neural network," in *2016 International Joint Conference on Neural Networks (IJCNN)*, July 2016, pp. 1277–1282.

[94] D. F. Specht and P. D. Shapiro, "Generalization accuracy of probabilistic neural networks compared with backpropagation networks," in *IJCNN-91-Seattle International Joint Conference on Neural Networks*, vol. i, Jul 1991, pp. 887–892 vol.1.

[95] D. F. Specht, "Probabilistic neural networks for classification, mapping, or associative memory," in *IEEE 1988 International Conference on Neural Networks*, July 1988, pp. 525–532 vol.1.

[96] ——, "Vectorcardiographic diagnosis using the polynomial discriminant method of pattern recognition," *IEEE Transactions on Biomedical Engineering*, vol. BME-14, no. 2, pp. 90–95, April 1967.

[97] V. Deolalikar, "Jackknifing documents and additive smoothing for naive bayes with scarce data," in *2015 IEEE International Conference on Data Mining*, Nov 2015, pp. 91–100.

[98] M. F. Mller, "A scaled conjugate gradient algorithm for fast supervised learning," *Neural Networks*, vol. 6, no. 4, pp. 525 – 533, 1993. [Online]. Available: http://www.sciencedirect.com/science/article/pii/S0893608005800565

[99] G. E. Nasr, E. A. Badr, and C. Joun, "Cross entropy error function in neural networks: Forecasting gasoline demand," in *Proceedings of the Fifteenth International Florida Artificial Intelligence Research Society Conference*. AAAI Press, 2002, pp. 381–384. [Online]. Available: http://dl.acm.org/citation.cfm?id=646815.708603

[100] M. Valtierra-Rodriguez, R. de Jesus Romero-Troncoso, R. A. Osornio-Rios, and A. Garcia-Perez, "Detection and classification of single and combined power quality disturbances using neural networks," *IEEE Transactions on Industrial Electronics*, vol. 61, no. 5, pp. 2473–2482, May 2014.

[101] O. F.-O. M. J. E.-G. J.-J. G. de la Rosa; A. Agera-Prez; Jos Carlos Palomares-Salas; J. M. Sierra-Fernndez, "Real-life power quality sags," 2017. [Online]. Available: http://dx.doi.org/10.21227/H2K88D